Characterization of Nitrosyl, Azido, and Carbonyl Complexes in Diiron Enzymes and Their Implications for O_2 and NO Activation

Shen Lu
B.S. Peking University, 1997
M.S. Peking University, 2000

A dissertation submitted to the faculty of the
OGI School of Science & Engineering
at Oregon Health & Science University
in partial fulfillment of the
requirements for the degree
Doctor of Philosophy
in
Biochemistry and Molecular Biology

October 2005

The dissertation "Characterization of Nitrosyl, Azido, and Carbonyl Complexes in Diiron Enzymes and Their Implications for O_2 and NO Activation" by Shen Lu has been examined and approved by the following Examination Committee:

Pierre Moënne-Loccoz, Advisor
Assistant Professor

James W. Whittaker
Associate Professor

H. Peter Larsson
Associate Scientist
Neurological Sciences Institute

Colin R.Andrew
Associate Professor
Eastern Oregon University

ACKNOWLEDGMENTS

First, I wish to express my deepest thanks to my research advisor, Dr. Pierre Moënne-Loccoz, who have given to me a new understanding of what it means to be a scientist and have provided me with many learning opportunities. I would not be where I am today if it wasn't for his immense patience over all those years. I would also like to thank Dr. James Whittaker for his guidance, seminar discussions, and for taking the time to examine this dissertation. I also wish to thank Dr. Colin Andrew and Dr. Peter Larsson for the time spent carefully reviewing my dissertation. I am also grateful to our collaborators in the research groups of Profs. Martin Bollinger, Simon de Vries, Kenneth Karlin, Paul Ortiz de Montellano, and Stephen Lippard for providing me with proteins and synthesized models, and for many enlightening discussions. I would like to thank Dr. Michael Gold, who provided me an opportunity of one year of training of protein purification and techniques for enzyme kinetic studies. I would also like to thank Profs. Ninian Blackburn, Thomas Loehr, Pierre Moënne-Loccoz, Michiko Nakano, Matthew Sachs, Joann Sanders-Loehr, James Whittaker, Gebretateos Woldegiorgis, and Peter Zuber, for their tutoring in biochemistry and biology and helping me enter this field from a chemistry background. I am also grateful to the entire metalloprotein group and people in EBS department for their immense help and friendship during my PhD studies. Special appreciations give to my parents and many former teachers for providing me with love, support, and encouragement during my long period of studies. Finally, I wish to give the deep thanks to my wife for always being there in times of need and for the great love, patience, and support she has given to me.

TABLE OF CONTENTS

LIST OF TABLES

LIST OF FIGURES

ABSTRACT

Characterization of Nitrosyl, Azido, and Carbonyl Complexes in Diiron Enzymes and Their Implications for O_2 and NO Activation

Shen Lu, M.S.

Ph.D., OGI School of Science & Engineering

at Oregon Health & Science University

October, 2005

Thesis Advisor: Dr. Pierre Moënne-Loccoz

Our research goal is to understand how diiron metal clusters control the diversity of their reaction with O_2 and NO. X-ray crystal structures of protein R2 from *E. coli* ribonucleotide reductase and the hydroxylase component of methane monooxygenase (MMOH) from *Methyloccocus capsulatus* (Bath) have revealed very similar non-heme diiron carboxylated bridged cluster. Yet, these two enzymes react very differently with O_2. In single turnover reaction, a diiron(III) peroxo intermediate is spectroscopically observable in MMOH but not in wt-R2, suggesting that the divergence between the O_2-reaction of MMOH and R2 might occur at the onset of the reaction. To investigate the possible involvement of a peroxo intermediate species in the O_2 activation of wt-R2, and determine the geometry of O_2- binding in R2 and MMOH, we have characterized O_2-analogs in these proteins using UV-vis absorption, EPR, RR, and FTIR spectroscopies.

Our investigation of the reaction of NO with the diiron sites in wt-R2 and the variant proteins D84E-R2, and W48F/D84E-R2 shows that in these three proteins the diiron sites accommodate two NO molecules to form a spin coupled $\{FeNO\}^7$ dimer.

Both Fe-N-O units share a common vibrational signature indicative of a fully symmetric $[\{FeNO\}^7]_2$ cluster. These structural motifs are consistent with the symmetric bridging peroxo intermediates characterized in the variant proteins, and they suggest that while such a symmetric peroxo intermediate is not detectable in wt-R2, the binding of O_2 and its initial reductive activation is the same in all three proteins.

The binding of azide to oxidized MMOH was also investigated with RR and FTIR techniques. The FTIR spectra define the azido complex as terminally bound to only one iron (III) at the diiron center. H/D exchange experiments detect the presence of a hydrogen bond interaction at the coordinating (N1) azide nitrogen atom. The hydrogen bond partner is proposed to be an aqua ligand one the second Fe. The photodissociation of the azido group from the metal cluster is associated with a proton uptake to from hydrazoic acid. The proton donor to the azido group is likely to be the same group involved in the hydrogen bond interaction. Our experimental data provide structural details that can be compared to theoretical prediction of the O_2 reaction in MMOH. The structure of the azide complex suggest that the peroxo complex might adopt an asymmetric structure, and that as predicted by the theoretical analysis, the presence of hydrogen bond between the peroxo group and an aqua ligand might favor the decay of H_{peroxo} and the formation of higher valent intermediate as the O-O bond is cleaved.

The reaction of NO with the diiron cluster of two NO reductases, cNOR from *Paracoccus denitrificans* and qCu_ANOR from *Bacillus azotoformans*, were also studied. Here again, the 2-electron reduction of two NO molecules to from N_2O is poorly understood. To determine how NO initially binds at the active site, we studied the binding of CO as an analog to NO-binding. These experiments reveal that two CO molecules could bind concomitantly at the diiron (II) sites, to form a heme-CO complex and a non-heme Fe_BCO complex. Our FTIR experiments strongly supported a mechanistic model where two NO molecules form a $[\{FeNO\}^7]_2$ unit that promote N-N bond formation.

CHAPTER 1

O_2 AND NO ACTIVATION IN DIIRON PROTEINS

1.1 Metals in Biology

Metals are receiving ever-increasing recognition for their roles in biological processes. The occurrence of metallobiomolecules in biological systems is becoming more important to the medical, pharmaceutical, agricultural, biotechnological, and environmental industries [Holm and Solomon, 1996; Lippard et al., 1994]. A large number of enzymes and proteins contain metal ions at their active sites. These metalloenzymes are involved in important biocatalytic processes such as fixation of nitrogen, methane biogenesis and oxidation, and oxidative or reductive degradation of metabolites. A detailed understanding of the structure and function of those enzymes can allow us to redesign these proteins to perform industrially relevant catalysis. Understanding the structural and functional significance of these metal sites requires specialized instrumentation and spectroscopic techniques.

Bioinorganic chemistry is an interdisciplinary field that connects inorganic chemistry with biology. It encompasses studies of metal ion uptake, their complexation with proteins, studies of the biological function they carry, and the storage and homeostasis of these metals in biological systems [Broderick and Coucouvanis, 2003]. This kind of research focuses on important cofactors that contain metal ions such as heme and non-heme iron clusters, and on the functional significance of certain groups of enzymes. It has been estimated that over 50% of all proteins are metalloproteins. Metalloenzymes such as superoxide dismutase and ribonucleotide reductase have been studied for decades with the goal of elucidating the details of their catalytic mechanisms. The discovery and characterization of

evolutionarily unrelated enzymes that utilize different metal clusters to promote comparable reaction provide powerful insights into catalytic mechanisms. The development of synthetic models for metalloenzymes remains a productive method for metalloenzyme studies. The mimic of the structures and properties of natural metal sites promotes our understanding of reaction mechanisms catalyzed by metalloenzymes [Holm and Solomon, 2004].

1.2 Non-heme Diiron Enzymes

O_2 activation by iron-containing proteins includes hemoproteins, and mono- and dinuclear non-heme proteins. Within the non-heme proteins, carboxylate-bridged diiron enzymes perform a variety of biological functions, including O_2 transport and storage, reduction of ribonucleotides in DNA synthesis, methane hydroxylation in carbon fixation, dehydrogenation of fatty acids in the regulation of membrane fluidity, and ferroxidase reactions in metal storage. The functional diversity of these enzymes can be rationalized by contrasting the structural features of their diiron clusters. For example, the diiron center in the O_2-transport enzyme deoxyhemerythrin is rich in nitrogen ligands, with 5 coordinated histidines, and it contains a single, open coordination site where O_2 binds to form a stable hydroperoxo diiron(III) complex [Stenkamp et al., 1985; Kurtz, 1999]. Dinuclear non-heme iron active sites are found in a wide range of metalloenzymes where they are often involved in reactions with dioxygen. The understanding of the chemical properties of non-heme iron oxygenases has increased dramatically in recent years. Spectroscopic and crystallographic studies have been used to provide critical insights into catalysis [Ryle and Hausinger, 2002; Stenmark et al., 2001].

In their three-dimensional structures, the family of diiron carboxylate enzymes shares a common structural motif: four-helix bundle. Not surprisingly, some appear to also share reaction intermediates in the course of their O_2-activation. For example, a peroxodiferric intermediate has been characterized in the ferroxidase reaction of

ferritin [Moënne-Loccoz et al., 1999], stearoyl-acyl carrier protein Δ^9 desaturase (Δ^9D) [Broadwater et al., 1999], mutant proteins of the R2 component of ribonucleotide reductase (RNR) [Moënne-Loccoz et al., 1998a], and methane monooxygenase hydroxylase (MMOH) [Liu et al., 1994; Liu et al., 1995a]. Subtle changes in the protein structure appear to tune the metallocenter properties and reactivity. As a vivid illustration of this control, mutations have been designed into R2 to change this enzyme into a self-hydroxylating monooxygenase reminiscent of MMOH activity [Baldwin et al., 2000; Baldwin et al., 2001; Krebs et al., 2000].

Ribonucleotide Reductase

RNR is responsible for the reduction of the four standard ribonucleotides to deoxyribonucleotides and thereby provides the precursors for synthesis of DNA. Three main classes of RNR enzymes have been discovered based on their different metal cofactors [Reichard, 1993]. Class I enzymes contain a diiron-carboxylate bridged cluster [Andersson and Graslund, 1995], class II contains cobalamin cofactor (vitamin B_{12}), and class III enzymes utilize a 4Fe-4S iron sulfur cluster [Stubbe and van der Donk, 1998b]. Despite these drastic variations, functional and structural similarities suggest that all these three RNRs evolved from a common ancestral reductase [Stubbe et al., 2001].

Class I RNRs are tetrameric enzymes ($\alpha_2\beta_2$), with the substrate binding active site located in the large α_2-homodimer called R1. The small β_2-homodimer contains a diiron active site in each polypeptide chain and is called R2 [Stubbe and Riggs-Gelasco, 1998a]. The R2 component is responsible for the generation and maintenance of a catalytically essential tyrosyl radical (Y122) that initiates ribonucleotide reduction on the R1 component via long-range electron transfer [Wallar and Lipscomb, 1996]. The first crystal structure of an R2 protein from *E. coli* was published in 1990 [Nordlund et al., 1990] with some refinements in 1993 [Nordlund and Eklund, 1993a]. The tyrosine residue 122 is less than 5 Å away from the diiron center and is deeply buried away from solvent inside the R2 subunit. Each of the diiron centers is

coordinated by one aspartate (D84), one histidine (H118 and H241), and three glutamate residues (E115, E204, and E238) brought together at the core of a four-α-helix bundle (Fig. 1.1 & 1.2A). The incorporation of iron into the R2 subunit, the oxygen activation of the diiron center in vivo, and the electron transfer between the R2 and R1 subunits are still matters of debate [Siegbahn, 1998; Andersson et al., 1999; Lovell et al., 2002; Himo and Siegbahn, 2003; Chang et al., 2004].

Methane Monooxygenase

Methane monooxygenase (MMO) uses O_2 to convert methane into methanol as the first step of carbon metabolism in methanotrophs [Feig and Lippard, 1994]. This reaction is achieved by reductive activation of dioxygen, as illustrated in Equation 1.1:

$$CH_4 + O_2 + NADH + H^+ \rightarrow CH_3OH + H_2O + NAD^+ \quad \text{(Eq. 1.1)}$$

Two varieties of MMO have been discovered in methanotrophic bacteria. The first is a copper-containing, membrane-bound enzyme known as particulate MMO (pMMO) [Murrell et al., 2000]. The recent crystal structure of pMMO revealed one mononuclear copper center, one dinuclear center, and one zinc center [Lieberman and Rosenzweig, 2005]. Yet, the nature of the metal cluster carrying the monooxygenase reaction and the active form of the enzyme remain to be defined. A soluble, iron-containing MMO (sMMO) has been characterized more thoroughly and is the focus of our research. The sMMO enzyme system consists of three components: a hydroxylase (MMOH), a coupling protein (MMOB) and a reductase (MMOR) [Fox et al., 1989]. X-ray crystal structures of MMOH have revealed a relatively flexible non-heme diiron center coordinated by two histidines and four glutamates [Rosenzweig et al., 1993]. The reduced diiron(II) MMOH, which binds and activates dioxygen, has a relatively short Fe–Fe distance of 3.3 Å due to the presence of a monodentate and a bidentate carboxylate bridge (Fig. 1.2B) [Deeth and Dalton, 1998; Kopp and Lippard, 2002].

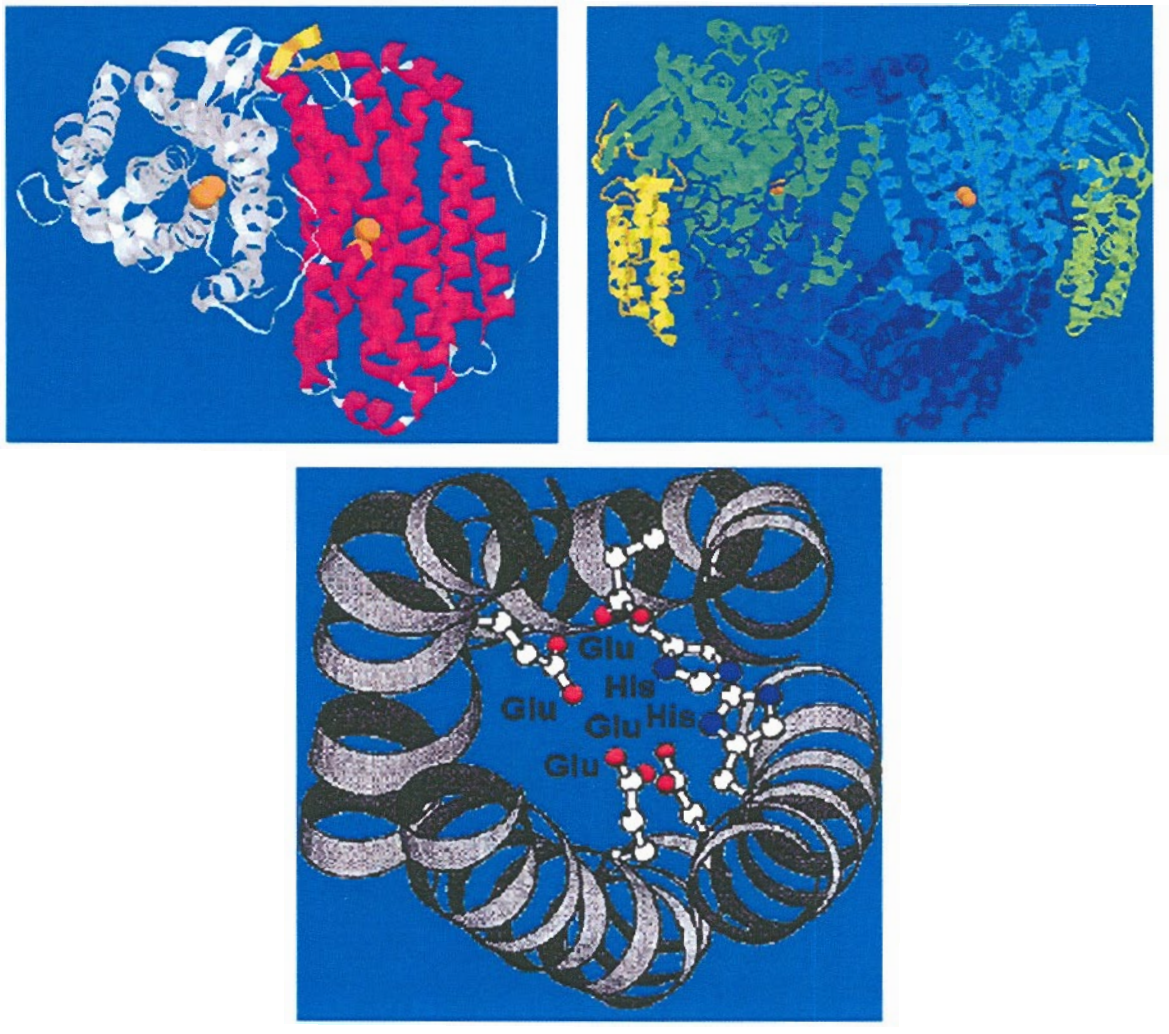

Fig. 1.1 X-ray crystal structures of diiron proteins.
- Top, left: Ribonucleotide reductase R2. The dimer subunits are colored white and red, and the iron atoms are shown as orange spheres (PDB accession code 1XIK).
- Top, right: Methane monooxygenase hydroxylase. The α subunits are colored light blue and green, the β subunits dark blue, and the γ subunits yellow and light green. The iron atoms in the α subunits are shown as orange spheres (PDB accession code 1FYZ).
- Bottom: The four α-helical bundle common to these two diiron proteins is shown with the coordinating side chains.

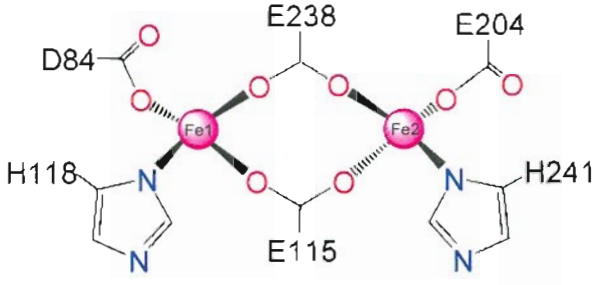

(A) reduced wt-R2

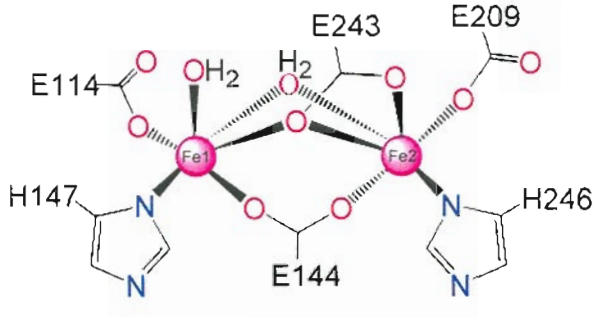

(B) reduced MMOH

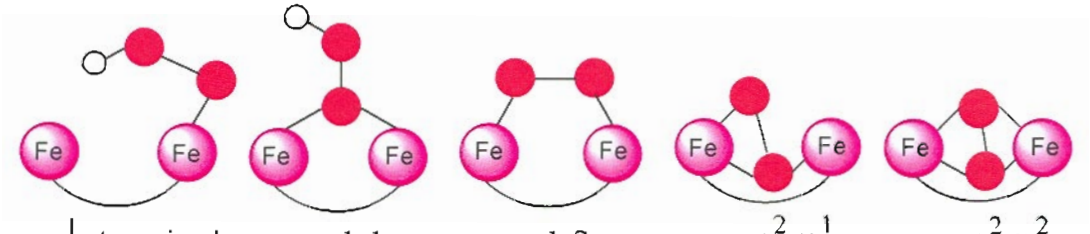

(C) putative peroxo diiron(III)

Fig. 1.2 Diiron centers in photoreduced wt-R2* (PDB accession code 1XIK) (A), and in dithionite-reduced MMOH (PDB accession code 1FYZ) (B). Also shown are possible peroxo diiron(III) geometries (C).

* In the dithionite reduced crystals, D84 chelates Fe1 in a bidentate coordination.

1.3 O_2 Activation in Non-Heme Diiron Proteins

Dioxygen plays a key role in many important biological processes, as in the mitochondrial respiration where the heme-copper containing enzyme cytochrome *c* oxidase couples O_2 reduction to H_2O with proton pumping across the inner microchondria membrane [Ferguson-Miller and Babcock, 1996]. The diiron centers of RNR-R2, MMOH and Δ^9D can also activate O_2 for catalysis [Wallar and Lipscomb, 1996; Solomon et al., 2000]. Reductive activation of O_2 commonly occurs in diiron clusters abundant in oxygen ligands and containing multiple open or solvent-occupied coordination sites. Despite the similarities in diiron centers, these evolutionarily related O_2 activating enzymes display a remarkable diversity in the reactions they catalyze. One hypothesis is that the fate of O_2 chemistry begins at the peroxo diiron(III) intermediate level where structural flexibility afforded by the iron carboxylate ligands produce different peroxide geometries which results in catalytic diversity.

We targeted two diiron-carboxylate proteins (R2 and MMOH) as the main focus of our research. Both of these proteins have been characterized by X-ray crystallography in various oxidation states [Nordlund et al., 1990; Rosenzweig et al., 1993; Lindqvist et al, 1996; Logan et al., 1996; Voegtli et al., 2000; Voegtli et al., 2003]. The proteins share a common structural scaffold comprised of a four-α-helix bundle where two helices each contribute either an aspartate or a glutamate residue, and the other two helices contain an E-X-X-H motif. These conserved amino acid side chains point toward the core of the helix bundle where they ligate the two iron atoms (Fig. 1.1); the remaining metal coordination spheres are occupied by solvent-derived oxo-, hydroxo-, or aqua ligands. One notable feature from many crystal structures of these proteins is the variability in carboxylate coordination that accompanies changes in the state of diiron cluster oxidation. For example, while the overall protein crystal structures of MMOH are nearly super imposable, the structure of chemically reduced MMOH exhibits an E243 residue in a μ-η^1:η^2 bridging coordination (Fig. 1.2B), which differs from its terminal coordination to Fe2 in the oxidized structure [Rosenzweig et al., 1995; Whittington et al., 2001; Hanson and Hanson, 1996]. In the

crystal structure of reduced wt-R2, E238 adopts a μ-1,3 bridging geometry between the two 4-coordinate Fe(II) ions. In the air-oxidized wt-R2 crystal structure, this same residue binds terminally to the 6-coordinate Fe2 [Logan et al., 1996].

These observations led to the concept of carboxylate shifts controlling the number of open coordination sites and the range of Fe–Fe distances during catalytic turnover. However, it is important to emphasize that while the crystal structures distinctly reveal a flexibility of carboxylate coordination with changes in oxidation state, the O_2 mechanisms of these proteins and the diversity of their catalytic products cannot be extrapolated solely on the basis of their reduced and oxidized diiron structures. For example, in the case of reduced wt-R2, the crystal structure displays two four-coordinate iron(II) atoms, whereas circular dichroism (CD) and magnetic circular dichroism (MCD) measurements predict an asymmetric diiron(II) cluster with one five-coordinate and one four-coordinate iron center [Pulver et al., 1995; Wei et al., 2004]. The success in understanding these mechanisms will thus depend on our being able to correlate reactivity, catalysis, and geometric information through a variety of kinetic and spectroscopic techniques. Resonance Raman (RR) and Fourier transform infrared (FTIR) spectroscopies can complement information from X-ray crystallography by defining the geometry of binding of substrate analogs and reaction intermediates in metalloproteins.

1.4 O_2 Activation and Reaction Intermediates

Kinetic and spectroscopic studies have identified several intermediates involved in O_2 activation by carboxylate diiron enzymes, and we expect that additional transient species will be uncovered as more is learned about these systems. Structural information about these intermediates has been obtained from stopped-flow and rapid freeze quench (RFQ) experiments in conjunction with optical absorption, electron-nuclear double resonance (ENDOR), electron paramagnetic resonance (EPR), Mössbauer, X-ray absorption (XAS), and RR spectroscopies [Moënne-Loccoz et al.,

1998a; Moënne-Loccoz et al., 1999; Bollinger et al., 1998], and also from synthesized model studies [Lee et al., 2002].

The first glimpse of a reactive intermediate in a non-heme diiron protein by RR studies was provided on the double variant protein W48F/D84E-R2 from *E. coli* [Moënne-Loccoz et al., 1998a]. The D84E mutation replacing an iron ligand in wt-R2 was designed to mimic the metal site in MMOH, while the W48F replacement blocked electron transfer from the indole ring to the diiron cluster. These mutations result in the accumulation of a peroxo intermediate with characteristic UV-vis and Mössbauer signatures [Bollinger et al., 1998]. The RR study unambiguously identified this species as a μ-1,2 peroxo-diiron(III) intermediate [Moënne-Loccoz et al., 1998a].

The peroxo intermediate of MMOH (H_{peroxo}) that results from the initial reaction of O_2 with its diferrous cluster is also of great interest in understanding O_2 activation. Density function theory (DFT) calculations using as initial coordinates the reduced cluster of MMOH and kinetic data from single turnover experiments predict that H_{peroxo} might correspond to a symmetric nonplanar μ-η^2:η^2 peroxo diiron(III) geometry (butterfly side-on bridging) or an asymmetric μ-η^2:η^1 geometry (Fig. 1.2C), as both structures appear to present comparable free energy [Gherman et al., 2004]. The prediction of energetically equivalent and structurally distinct peroxo-diiron(III) clusters supports the hypothesis that carboxylate shifts and alternative hydrogen bond partners favor interconversion between peroxide structures.

Another avenue of studies involves synthetic models that mimic the dioxygen reactivity of diiron proteins. So far only a few diiron(III) peroxo complexes have been successfully prepared and characterized [Tshuva and Lippard, 2004]. Exposing the dinucleating ligand N,N,N',N- tetrakis(2-benzylimidazolyl-methyl)-2-hydroxo-1,3-diaminopropane (HPTB) to O_2 at -80 °C results in the formation of a diiron(III) μ-1,2 peroxo complex [Que and Dong, 1996]. The two iron(III) atoms bridged by the peroxo group and a μ-alkoxo group are 3.46 Å apart. distance and symmetric complex presents two diiron(III) was crystalographically characterized with a iron-iron distance. Unfortunately in this symmetric peroxo complex, both irons are coordinated

to 2 nitrogen ligands which does not exactly reproduce the ligand sets observed in the active sites of MMOH or the R2 protein, and variations in the steric bulk of the ligand set and its electron donating ability are known to strongly influence the formation and stability of the peroxo species. In particular, weaker electron donors and sterically bulkier ligands that form a hydrophobic pocket at the O_2 binding site are known to stabilize peroxo complexes [Tshuva and Lippard, 2004]. Recent successes with the characterization of higher valent complexes in non-heme iron models are also providing clues about the structural parameters important to the O_2 activation process [Que, 2004]. Yet, the striking similarities of the diiron site structures in R2 and MMOH and their divergence in O_2 activation will remain a major paradox to synthetic chemist for years to come.

1.5 Substrate Analogs as Reporters of Intermediate Structures

Besides their reaction with O_2, diiron enzymes also participate in denitrifying and detoxifying NO reductase reactions, where two NO molecules are reduced by 2 electrons to N_2O. In these reactions the binding of one NO per iron may lead to the formation of a $[FeNO]_2$ intermediate that promotes N-N bond formation, but supporting evidence for such a complex are lacking. Our research aims to elucidate the structure of the peroxo intermediates in R2 and MMOH, and the iron-nitrosyl intermediates in diiron containing NO reductases. The hypothesis we explore is that the fate of O_2 chemistry begins at the peroxo intermediate level where structural flexibility afforded by the iron carboxylate ligands allows interconversion between peroxide geometries, result in a catalytic diversity. In the NO reductase reaction, we intend to determine whether both irons can bind NO to form an iron-nitrosyl dimer as proposed in earlier models [Moënne-Loccoz et al., 1998b; Moënne-Loccoz et al., 2000].

We use O_2 and NO analogs to mimic these reaction intermediates. Specifically, azido, nitrosyl, and carbonyl complexes are used to validate crystal structures, to probe

chemical reactivities, to investigate O_2 and NO binding in protein pockets, and to compare and contrast diiron clusters from different enzymes. In the event that intermediates cannot be trapped, surrogates become critical to the characterization of active site clusters.

RR spectroscopy has the unique capability to identify peroxo intermediates and their analogs to define their binding geometry with regard to the two metal ions [Moënne-Loccoz et al., 1998a]. Another technique that we have found particularly valuable in characterizing these complexes is FTIR spectroscopy coupling to low-temperature photolysis of the exogenous molecule. This technique, which we applied to nitrosyl adducts in R2 proteins, carbonyl complexes in NOR, and azido complexes in MMOH, can provide structural information and determine hydrogen bond interactions at the active sites. Since the formation and decay of peroxo intermediates depends on these interactions and the proton transfers they may promote, this approach has great potential for elucidating structural details important to the mechanisms of O_2 and NO reaction in diiron proteins.

CHAPTER 2
VIBRATIONAL TECHNIQUES AND CASE STUDIES

2.1 Instrumentation and Methods

Anaerobic Sample Preparation

Samples were made anaerobic by degassing and exchanging with argon on a Schlenk line. Protein solutions were purged by exposure to a continuous water vapor saturated argon flow for at least 30 min. Upon completion, the solutions were maintained under a slight positive pressure with the aid of the Schlenk line. Anaerobic protein solutions were then ready for reduction, mixture with reactive solution such as azide solution, or injection of reactive gases such as CO and NO. To avoid contamination by O_2, all such handling was performed inside an anaerobic glove box.

UV-vis Spectroscopy

Electronic absorption spectra of the samples used for RR and FTIR spectroscopies were obtained on a Cary 50 Varian spectrophotometer with 1-nm wavelength resolution and scanning rate of 1200 nm/min. Samples were monitored before and after RR and FTIR experiments.

RR Spectroscopy

Typical sample volumes for RR experiments are 20 μl when using a 1-mm inner diameter capillary, and 200 μl when using a 4-mm inner diameter NMR tube. To maximize the quality of the RR data, the enzyme concentrations ranged from 50 to 250 μM for heme proteins, and between 0.5 and 3 mM for non-heme iron proteins. RR

spectra were obtained on a McPherson 2061/207 spectrograph (0.67 m with variable gratings) equipped with a Princeton Instrument liquid N_2-cooled (LN-1100PB) CCD detector. Kaiser Optical supernotch filters were used to attenuate the Rayleigh scattering. Excitation sources consisted of an Innova 302 krypton laser (413 nm), a Liconix 4240NB He/Cd laser (442 nm), and a Coherent Innova 90 argon ion laser (458 nm) (Coherent, Santa Clara, CA). Frequencies were calibrated relative to indene and CCl_4 standards and are accurate to ± 1 cm^{-1}. CCl_4 was also used to check the polarization conditions. Spectra were recorded in a 90° scattering geometry on samples at room temperature. RR spectra from frozen samples thermostated to 90 K with a liquid nitrogen cold finger were obtained with a 180° back-scattering geometry. The laser power was usually kept below 10 mW on sample to minimize laser decomposition and to prevent undesirable photochemical side reactions. In some experiments with photolabile ligands, the laser power was reduced as low as 0.05 mW using neutral density filters.

FTIR Spectroscopy

For most FTIR experiments and whenever possible, the enzyme concentration was raised to the millimolar range and the optical pathlength was limited to 15 μm, as these conditions minimize the background signal from H_2O (Fig. 2.1, left). Moreover, as microbubble formation is difficult to control, they produce interference ripples with a frequency equal to 1/2d where d is the pathlength. These ripples origin from the interferences of light reflected from the front and back windows of the FTIR cell. A 15-μm pathlength produces broad ripples of 333 cm^{-1} easily differentiated from vibrational features (Fig. 2.1, right). An 11-μL droplet of sample was deposited on a 20 x 2 mm CaF_2 window in an anaerobic glove box (Coy laboratory products, Inc. and Vacuum Atmospheres, Inc.). A second CaF_2 window was dropped on the sample to form an optical cell with a pathlength controlled by a 15-μm Teflon spacer. Once the IR cell was securely mounted, the formation of the NO, CO or N_3^- adducts could be

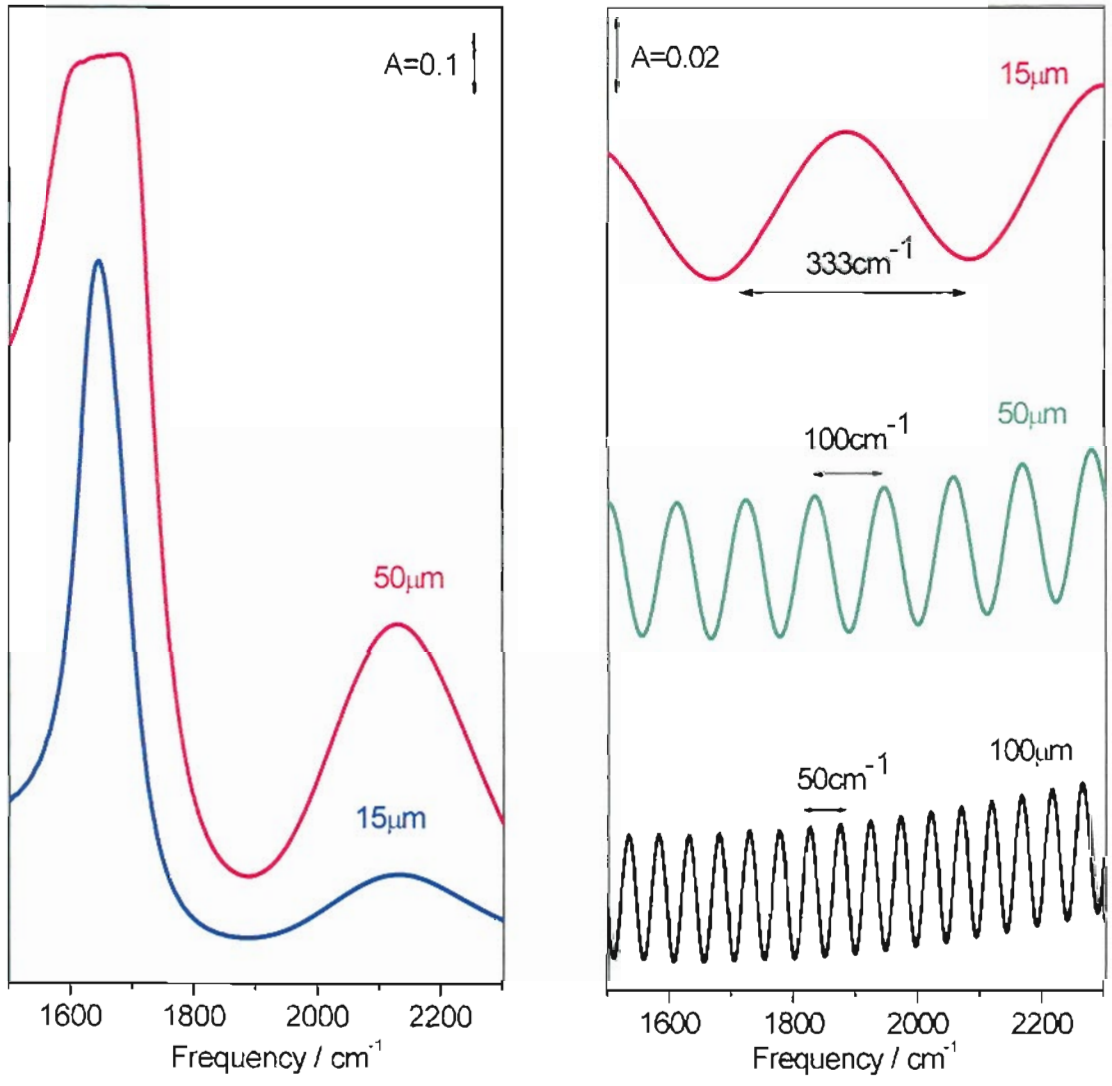

Fig. 2.1 Room temperature FTIR spectra of H_2O and air bubbles.
- Left panel: FTIR spectra of H_2O with a 15-μm spacer and a 50-μm spacer.
- Right panel: Ripples from air bubbles with different Teflon spacer. The interference frequencies are 333 cm^{-1} with a 15-μm spacer, 100 cm^{-1} with a 50-μm spacer, and 50 cm^{-1} with a 100-μm spacer, respectively.

confirmed by obtaining the UV-vis spectrum directly on FTIR samples by using a Cary 50 spectrophotometer.

FTIR spectra were obtained on a Perkin-Elmer system 2000 equipped with a liquid-N_2 cooled MCT detector. The instrument was constantly purged with dried compressed air to limit interference from water vapor. Sets of 1000-scan accumulations were acquired at a 4-cm^{-1} resolution and ratioed against a background spectrum of the empty sample chamber obtained before loading the sample. The cell was connected to a thermostatic water bath to control the temperature at 20℃. For cryogenic temperature experiments, the same IR cell was attached to a closed-cycle helium compressor system (Displex, Advanced Research Systems, Inc.). To photodissociate the metal bound CO, NO, or N_3^- adducts, continuous illumination of the samples was performed with a 50 W tungsten lamp after filtering out heat and NIR emission.

2.2 Case study I: Nitrosyl Complex of Heme Oxygenase-1*

NO functions as a signaling molecule in a diversity of physiological responses [Murad, 1999; Zakhary et al., 1997]. Many of these responses result from the interaction of NO with a heme group anchored to the receptor protein [Rotenberg and Maines, 1990]. NO, unlike O_2, can bind to the iron atom of hemoproteins in both the ferric and ferrous states, and the binding affinity is generally much higher for the ferrous state. For example, at pH 7.4 and 25℃, the K_d values for the binding of NO to ferrous deoxymyoglobin and ferric metmyoglobin (met-Mb) are 7×10^{-6} and 905 μM, respectively, a difference of roughly 10^8 [Wang et al., 2003]. The binding of NO to the ferric heme oxygenase-1 (HO-1) complex with $K_d = 1.4$ μM approaches the tightest

---

* Material in this chapter has been published in this or similar form in *J. Biol. Chem.* and is used here with permission of the American Society for Biochemistry and Molecular Biology.

Wang, J., Lu, S., Moënne-Loccoz, P., and Ortiz de Montellano, P. R. (2003) Interaction of nitric oxide with human heme oxygenase-1. *J. Biol. Chem.* **278,** 2341-2347.

binding so far observed for any ferric hemoprotein. Detailed analysis shows that this high affinity, when compared with the ~500-fold lower affinity for met-Mb, is due to a 50 times faster k_{on} and a 10 times slower k_{off} for NO, but the structural basis for these differences is unclear.

Indirect evidence exists for the inhibition of HO-1 in tissue homogenates by endogenously formed NO, but focused studies of the inhibition of HO-1 by NO have not been carried out. NO has been shown by RR and EPR to bind to the ferrous-heme iron of HO-1 to form an iron-nitrosyl complex, but the binding of NO to HO-1 in its ferric state has not been examined. The ferric-nitrosyl complex is denoted as a $\{FeNO\}^6$ species in the generalized formulation of Enemark and Feltham, which counts metal *d*-electrons plus the lone π^* electron from the NO to describe metal nitrosyl species [Enemark and Feltham, 1974; Wescott and Enemark, 1999]. Similarly, ferrous-nitrosyl are described as $\{FeNO\}^7$ species. Our RR studies of the reaction of NO with ferric HO-1 reveals the formation of a 6-coordinate low-spin heme nitrosyl complex. The ν(N-O), detected by FTIR, is only 4 cm^{-1} lower than that of the corresponding met-Mb-nitrosyl complex, but the large bandwidth of the ν(N-O) mode in HO-1 suggests a greater degree of ligand conformational freedom. The structural information is discussed in the context of the difference in binding affinity for NO in HO-1 and Mb.

2.2.1 Materials and Methods

The UV-vis spectra of the HO-1 proteins were recorded on a Cary 50 spectrophotometer with standard parameters. The enzyme concentration for RR experiments was ~125 μM in 0.1 M potassium phosphate buffer at pH 7.4. ^{14}NO and ^{15}NO gas purchased from Aldrich was bubbled through a 0.1 M KOH solution to remove higher nitrogen oxides. Formation of the NO adduct was achieved by addition of an NO-saturated buffer solution to an argon-purged HO-1 solution in the Raman capillary cell to reach a final concentration of ~2 mM NO. Before freezing the samples, the completion of the reaction was confirmed by UV-vis spectroscopy in the same

Raman capillary cell. Once the RR experiments were completed, the sample was thawed to obtain its UV-vis spectrum and confirm the stability of the complex during the laser illumination at 90 K. RR spectra were obtained on a custom McPherson 2061/207 spectrograph equipped with a Princeton Instruments liquid N_2-cooled CCD detector. Spectra were collected on frozen samples kept at ~90 K with N_2 cold finger in a backscattering geometry with 413-nm laser excitation.

For FTIR experiments, the enzyme concentration was increased to ~1 mM by filtration using a Microcon 10 ultrafiltration device (Amicon). The concentrated HO-1 solution was made anaerobic in a vial before exchanging the headspace with pure NO gas to reach a final concentration of ~2 mM NO in solution. The protein sample was then injected into an IR cell consisting of CaF_2 windows separated by a 50-μm Teflon spacer. The formation of the NO adduct was confirmed by UV-vis spectroscopy in the IR cell before and after FTIR experiments. FTIR spectra were obtained at room temperature and 15 K on a PerkinElmer Life Sciences system 2000 equipped with a liquid N_2-cooled MCT detector. Sets of 20 min accumulations were acquired at a 2-cm^{-1} resolution on the samples and the identical cell filled with buffer was used for background subtraction.

2.2.2 Spectroscopic Results

The NO complex of ferric HO-1 prepared for RR experiments was very photolabile and could not be characterized at room temperature, but at 90 K the geminate rebinding of NO was favored and allowed the detection of the nitrosyl complex at moderate laser power. The spectrum of ferric HO-1 reveals a 6-coordinate high-spin/low-spin (HS/LS) equilibrium with ν_3, ν_2, and ν_{10} modes at 1482/1508, 1566/1585, and 1608/1640 cm^{-1}, respectively. After exposure to NO, the porphyrin skeletal modes are observed at higher frequencies with ν_4, ν_3, ν_2, and ν_{10} at 1378, 1511, 1588, and 1645 cm^{-1}, respectively (Fig. 2.2). These frequencies identify the NO adduct as a 6-coordinate low-spin complex. A minor 6-coordinate high-spin population

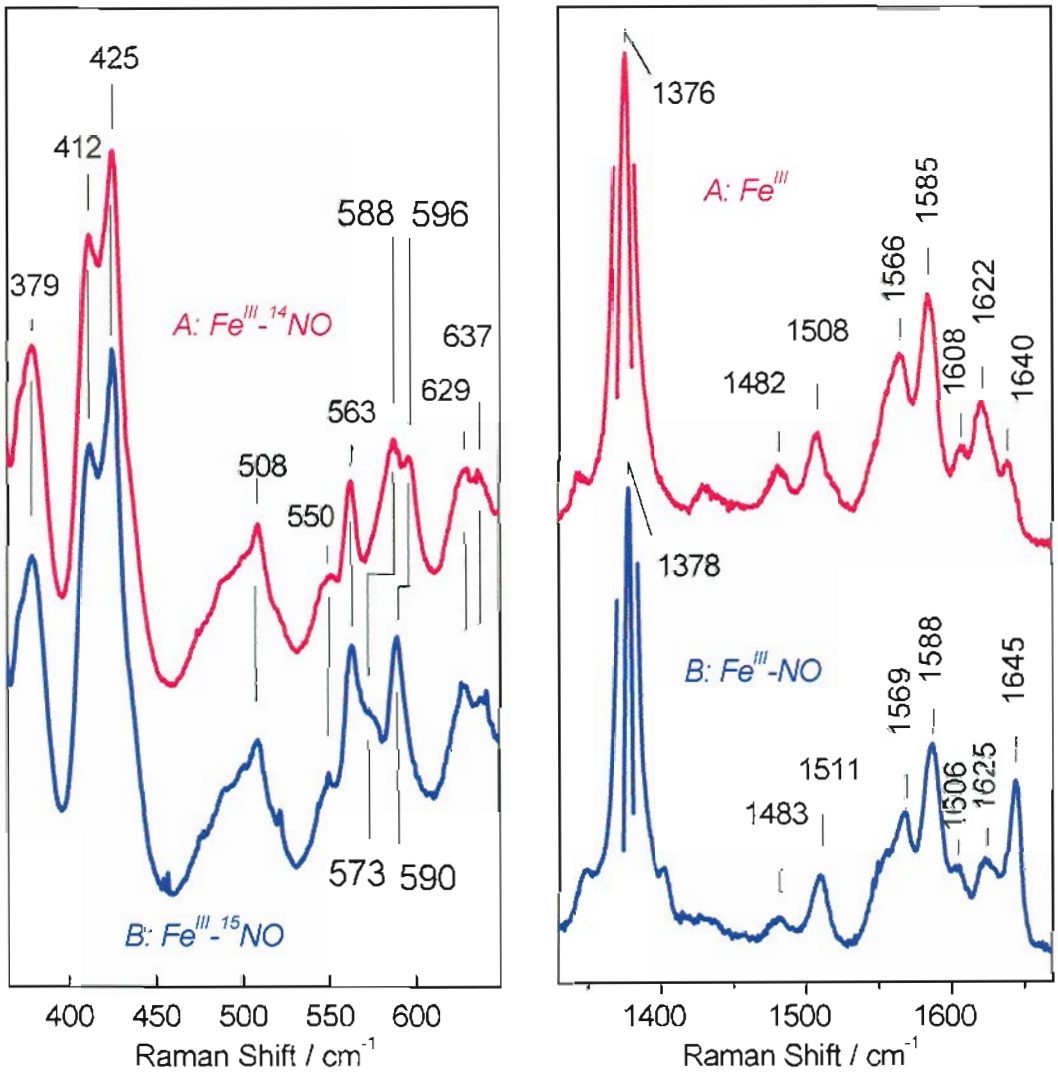

Fig. 2.2 RR spectra of the ferric HO-1 nitrosyl complexes obtained at 90 K using a 413-nm excitation.
- Left panel: low-frequency spectra of the $\{FeNO\}^6$ formed with ^{14}NO (A) and ^{15}NO (B).
- Right panel: high-frequency spectra of the ferric (A) and $\{FeNO\}^6$ complex (B).

Reproduced with permission:

Wang, J., Lu, S., Moënne-Loccoz, P., and Ortiz de Montellano, P. R. (2003) Interaction of nitric oxide with human heme oxygenase-1. *J. Biol. Chem.* **278,** 2341-2347.

revealed by a ν_3 component at 1483 cm^{-1} is assigned to some photolyzed species. In the low-frequency region of the RR spectra, the identification of the Fe-N-O vibrational modes was facilitated by the use of isotopic labeling and the close similarity of these frequencies with those observed in other hemoproteins (Fig. 2.2). In the met-Mb ferric-nitrosyl complex, the ν(Fe-NO) (Δ^{15}N) and δ(Fe-N-O) (Δ^{15}N) are observed at 595 (-6) and 573 (-11) cm^{-1}, respectively. In the ferric nitrosyl complex of HO-1, two bands at 596 and 588 cm^{-1} that shift to 590 and 573 cm^{-1} with ^{15}NO are assigned to the ν(Fe-NO) and the δ(Fe-N-O), respectively.

In heme ferric-nitrosyl complexes, the ν(N-O) is not resonance enhanced with Soret excitation, but it can be observed in FTIR spectrum. This vibration is detected at 1918 cm^{-1} in the $\{FeNO\}^6$ complex of HO-1, only 4 cm^{-1} lower than that in met-Mb (Fig. 2.3). Such ν(N-O) frequencies are characteristic of linear six-coordinated $\{FeNO\}^6$ complexes. It is much more difficult to produce good FTIR blanks with frozen samples at cryogenic temperatures rather than samples in the liquid state. Despite these experimental problems, difference spectra against blanks are of sufficient quality to confirm that the species observed at 20 °C also form at 15 K. Difference spectra of much higher quality can be obtained by taking advantage of the photolabile character of metal-bound exogenous ligand. Light induced FTIR difference spectra of NO-treated ferric Mb and HO-1 display a single ν(N-O) that corresponds with 6 cm^{-1} and 11 cm^{-1} up-shift to those observed at room temperature, respectively (Fig. 2.3). A significant difference between these two signals resides in the ~20 cm^{-1} half-width of this stretching mode in HO-1 compared with the 9 cm^{-1} half-width observed in met-Mb. In met-Mb the configuration of the nitrosyl group is clearly defined by the presence of the imidazole ring from the distal histidine, but the absence of distal polar side chains above the heme iron of HO-1 and a greater solvent accessibility may permit greater fluctuation of the NO ligand, resulting in substantial inhomogeneous broadening of the ν(N-O). When temperature was cooled down to 15 K, an unusual large upshift of 11 cm^{-1} was observed in nitrosyl HO-1 complex. Meanwhile, an asymmetric ν(N-O) band at low temperature suggests more than one

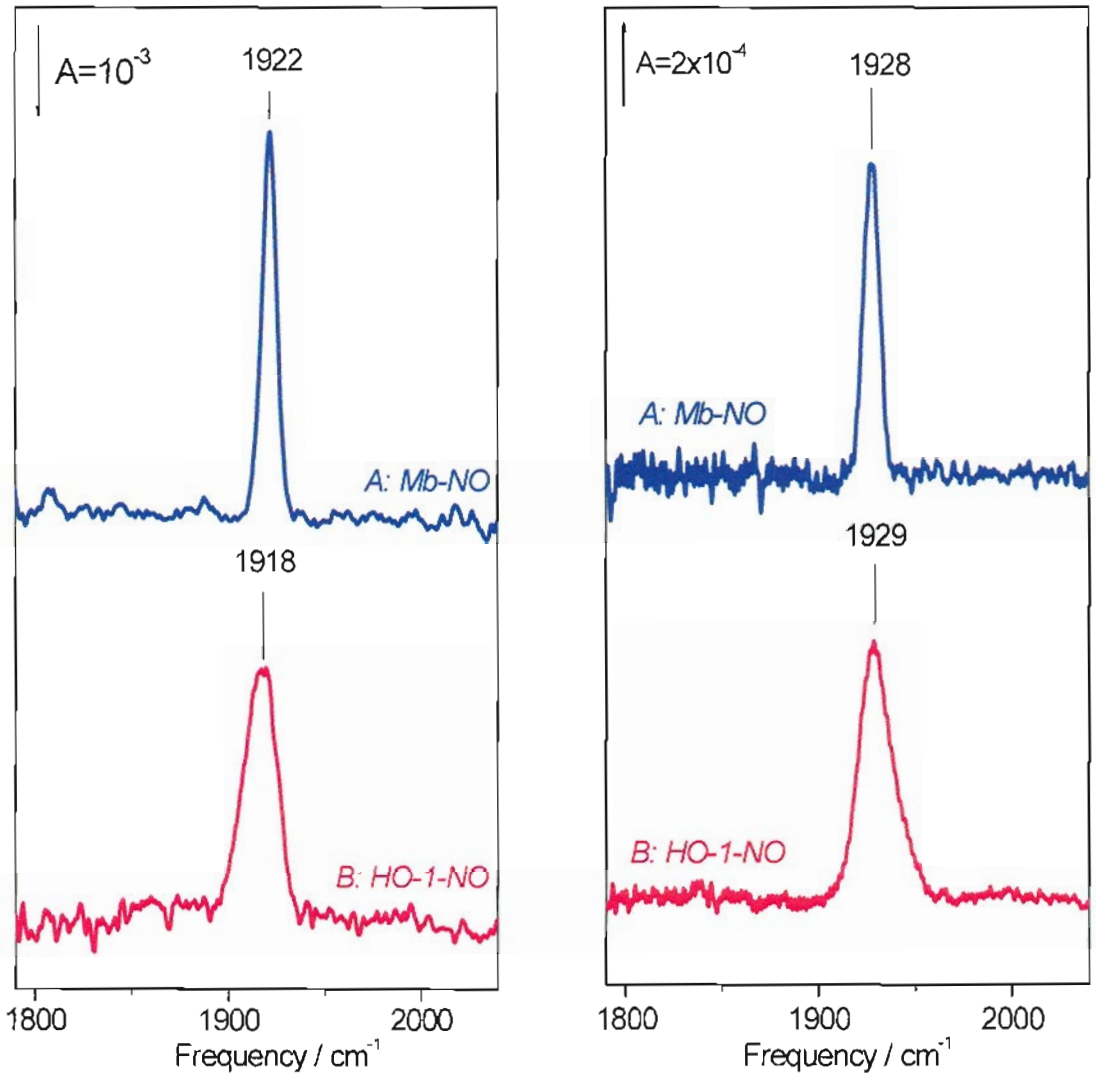

Fig. 2.3 FTIR spectra of the ferric nitrosyl complex in met-Mb (A) and HO-1 (B).
- Left panel: room temperature data.
- Right panel: Light induced difference spectra obtained at 15 K.

Reproduced with permission:

Wang, J., Lu, S., Moënne-Loccoz, P., and Ortiz de Montellano, P. R. (2003) Interaction of nitric oxide with human heme oxygenase-1. *J. Biol. Chem.* **278,** 2341-2347.

binding geometries present for nitrosyl HO-1 complex. Thus, the origin of the large upshift of ν(N-O) frequency with decreasing temperature may relate to changes in equilibrium distributions between several iron-nitrosyl configurations.

2.2.3 Discussion

The overall vibrational characterization of the $\{FeNO\}^6$ complex in HO-1 and Mb demonstrates that these complexes share the same bonding geometry and strength. RR studies show that the $\{FeNO\}^6$ complex in HO-1 is a 6-coordinate low-spin species, as in the met-Mb complex. Furthermore, FTIR shows that the ν(N-O) band of the $\{FeNO\}^6$ complex in HO-1 is at 1918 cm^{-1}, only 4 cm^{-1} lower than for the met-Mb complex. This suggests that coordination of the NO to the heme iron is similar in both hemoproteins, although the larger bandwidth in the HO-1 complex suggests that a greater mobility of the nitrosyl group in HO-1. Furthermore, in both met-Mb and ferric HO-1, the iron in the absence of NO is coordinated to a water molecule. In view of the similarities in coordination properties, the differences in the K_d for binding of NO to ferric HO-1 and met-Mb must stem from other differences in the active sites of the two proteins. The ~50-fold increase in k_{on} rate for NO in HO-1 compared with met-Mb may reflect a higher steric hindrance in the distal pocket of met-Mb. In both these ferric proteins the sixth iron coordination site is occupied by a water molecule that must be displaced for NO to bind, but displacement of the water molecule in HO-1 may require relatively little protein side chain rearrangement relative to those occurring in met-Mb.

The unusually low K_d value for the binding of NO to ferric HO-1 suggests that the catalytic turnover of the enzyme should be inhibited by NO. Furthermore, as the catalytic cycle of HO-1 traverses the ferrous state, NO could bind not only to the ferric but also to the ferrous protein, again inhibiting the enzyme. While the K_d value for the binding of NO to the ferrous protein can be expected to be even lower than that of the ferric enzyme, the K_d value for NO-binding to the ferric enzyme is already low enough that significant inhibition of the protein could occur at physiological or pathological NO concentrations, which range from 50 nM to 5 μM.

2.3 Case Study II: O_2 Activation in Heme-Copper Models of Terminal Oxidases*

Terminal oxidases mediate the four-electron four-proton reduction of O_2 to water, using low potential electron-donors and coupling this exergonic reaction to pump protons across membranes to drive ATP synthesis. Protein X-ray structures reveal that O_2 binding and reduction occurs at a binuclear active site consisting of a high-spin heme group (with proximal histidine), with a tris-histidine ligated copper ion (Cu_B) situated on the distal side (Fig. 2.4, top) [Gennis, 1998; Proshlyakov et al., 2000; MacMillan et al., 1999]. Several heme-copper synthetic models have been reported to react with O_2 to give μ-peroxo Fe^{III}-(O_2^{2-})-Cu^{II} species. Most of these studies have used tris[2-pyridylmethyl]amine (TMPA) as a 4N-chelating ligand to Cu (Fig. 2.4, bottom) [Ghiladi et al., 2001]. However, extensive studies of copper dioxygen chemistry have shown that changes in ligand structure or identity can dramatically alter O_2 chemistry of Cu [Karlin et al., 1997]. Specifically, tetradentate TMPA induces formation of an end-on ligated (Cu^{II}-O-O-Cu^{II}) peroxo-dicopper(II) structure upon O_2 reaction with $[Cu^{I}(TMPA)-(MeCN)]^{+}$, whereas tridentate ligands of $[Cu^{I}(L^{Me_2N})]^{+}$ generate side-on μ-η^2:η^2-peroxo-dicopper(II) species [Que and Tolman, 2002; Liang et al., 2002; Zhang et al., 2003].

---

* Material in this chapter has been published in this or similar form in *Proc. Natl. Acad. Sci. U. S. A.*, and *J. Am. Chem. Soc.* , and is used here with permission of the National Academy of Sciences of the United States of America, and the American Chemical Society.

Kim, E., Helton, M. E., Wasser, I. M., Karlin, K. D., Lu, S., Huang, H., Moënne-Loccoz, P., Incarvito, C. D., Rheingold, A. L., Honecker, M., Kaderli, S., and Zuberbuhler, A. D. (2003) Superoxo, μ-peroxo, and μ-oxo complexes from heme/O_2 and heme-Cu/O_2 reactivity: copper ligand influences in cytochrome c oxidase models. *Proc. Natl. Acad. Sci. U. S. A.* **100**, 3623-3628.

Kim, E., Shearer, J., Lu, S., Moënne-Loccoz, P., Helton, M. E., Kaderli, S., Zuberbuhler, A. D., and Karlin, K. D. (2004) Heme/Cu/O_2 reactivity: change in Fe^{III}-(O_2^{2-})-Cu^{II} unit peroxo binding geometry effected by tridentate copper chelation. *J. Am. Chem. Soc.* **126,** 12716-12717.

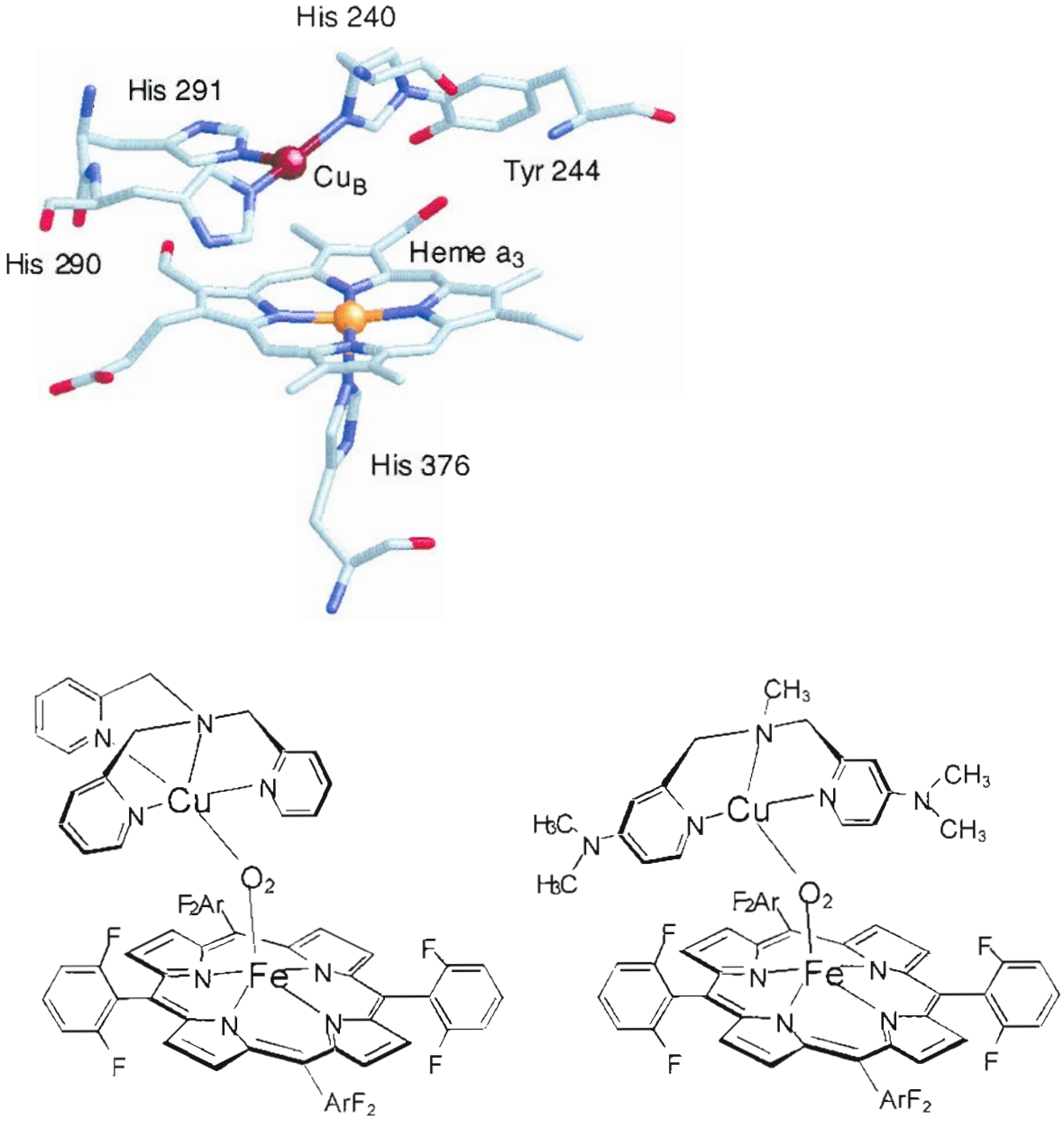

Fig. 2.4 Structure of the fully reduced active site of bovine cytochrome *c* oxidase (top), and synthetic models: (F_8TPP)Fe/Cu(TMPA) (bottom, left), and (F_8TPP)Fe/Cu(L^{Me_2N}) (bottom, right).

Reproduced with permission:

Kim, E., Helton, M. E., Wasser, I. M., Karlin, K. D., Lu, S., Huang, H., Moënne-Loccoz, P., Incarvito, C. D., Rheingold, A. L., Honecker, M., Kaderli, S., and Zuberbuhler, A. D. (2003) Superoxo, μ-peroxo, and μ-oxo complexes from heme/O_2 and heme-Cu/O_2 reactivity: copper ligand influences in cytochrome c oxidase models. *Proc. Natl. Acad. Sci. U. S. A.* **100**, 3623-3628.

2.3.1 Materials and Methods

RR spectra were obtained on frozen samples kept at ~90 K with a liquid nitrogen coldfinger. A 413-nm Kr^+ laser (Innova 302, Coherent Inc.) was used for excitation in conjunction with a Kaiser Optical supernotch filter to attenuate Rayleigh scattering. A 442-nm excitation from a He-Cd laser (Liconix 4240NB) was also used to characterize the dinuclear μ-oxo product. The backscattered light was analyzed with a McPherson 2061/207 spectrograph (0.67 m with variable gratings) equipped with a Princeton instrument liquid-N_2-cooled (LN-1100PB) CCD detector. Frequencies were calibrated relative to aspirin, indene and CCl_4 standards and are accurate to ±1 cm^{-1}. The laser power was kept below 10 mW and the samples were spun within the coldfinger holder to prevent adverse effects from the laser illumination. After completion of these experiments, the headspaces of each samples were analyzed using a 90° scattering geometry at room temperature to determine *in situ* the isotope constitution of the oxygen gas.

2.3.2 Results and Discussion

The reduced compound, the peroxo intermediate, and the oxo product can be easily differentiated by their high frequency RR spectra (Fig.2.5). Porphyrin skeletal modes of the peroxo species in the high-frequency region of the RR spectra are consistent with a five-coordinate high-spin ferric heme species as previously observed in $[(F_8)Fe^{III}\text{-}(O_2^{2-})\text{-}Cu^{II}(TMPA)]^+$ [Ghiladi et al., 2001]. X-ray crystal structures of the products indicate that the Fe-O-Cu unit is significantly bent in complex formed with the tridentate Cu complex compared to tetradentate systems. The Fe-O-Cu oxo product can be formed when O_2-exposed reduced samples are warmed up to room temperature. Soret excitation of $[(F_8)Fe^{III}\text{-}(O^{2-})\text{-}Cu^{II}(L^{Me_2N})]^+$ at 413 nm results in RR spectra dominated by strong porphyrin skeletal modes and weak iron-ligand vibrations (Fig. 2.6). Comparison of low-temperature RR spectra of oxo product generated in CH_2Cl_2/6% EtCN with $^{16}O_2$ or $^{18}O_2$ reveals two isotopic shifts. The 792 cm^{-1} (-40 cm^{-1}) vibration is assigned to a ν_{as}(M-O-M).

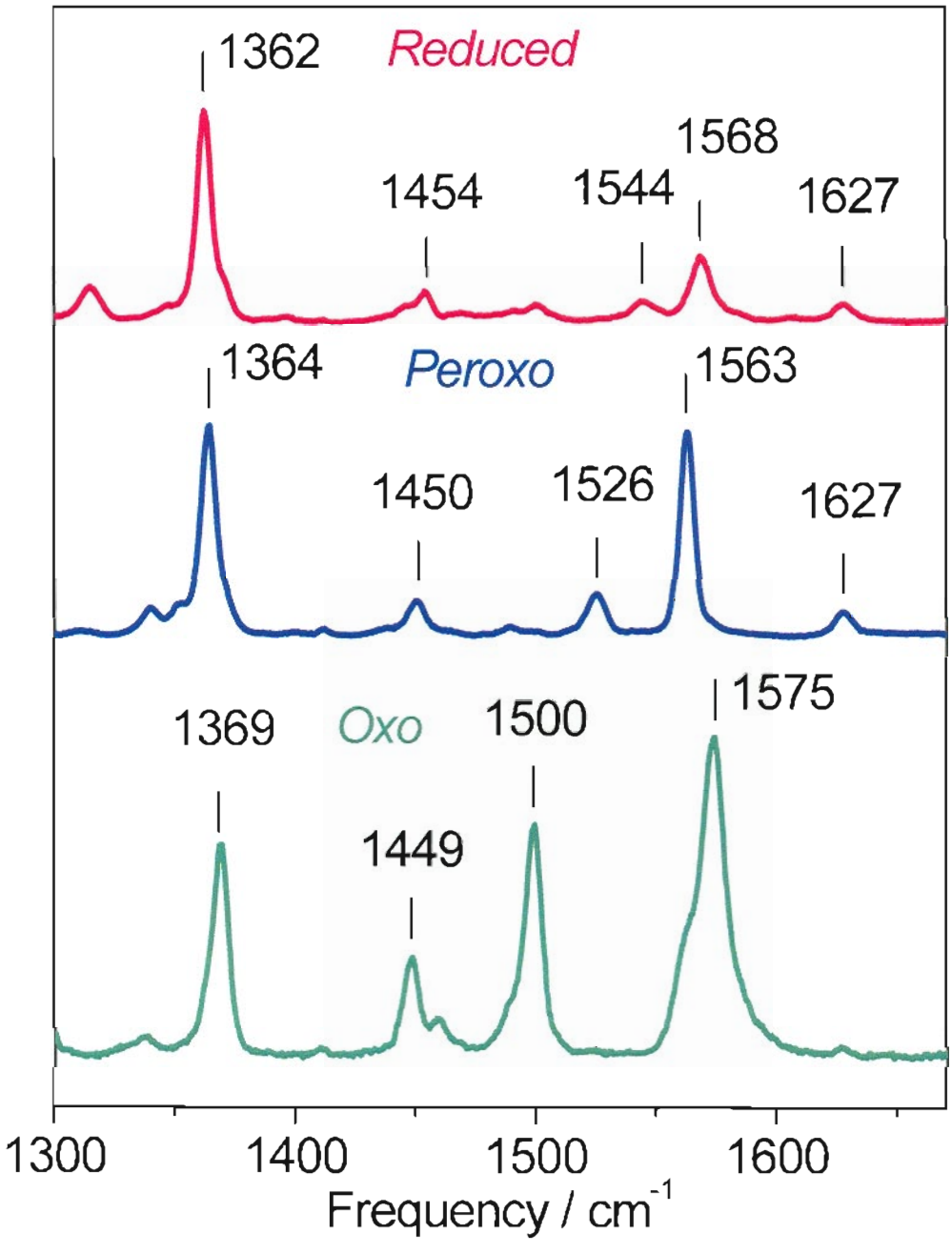

Fig. 2.5 High-frequency RR spectra of $(F_8)Fe/Cu(L^{Me_2N})$ model obtained with 413-nm excitation at 90 K (solvent: CH_2Cl_2 with 6% EtCN).
- Top (red): 1:1 mixtures of $(F_8)Fe^{II}$ and $[(L^{Me_2N})Cu^{I}]^{+}$
- Middle (blue): μ-peroxo complex $[(F_8)Fe^{III}\text{-}(O_2^{2-})\text{-}Cu^{II}(L^{Me_2N})]^{+}$
- Bottom (green): μ-oxo complex $[(F_8)Fe^{III}\text{-}(O)\text{-}Cu^{II}(L^{Me_2N})]^{+}$

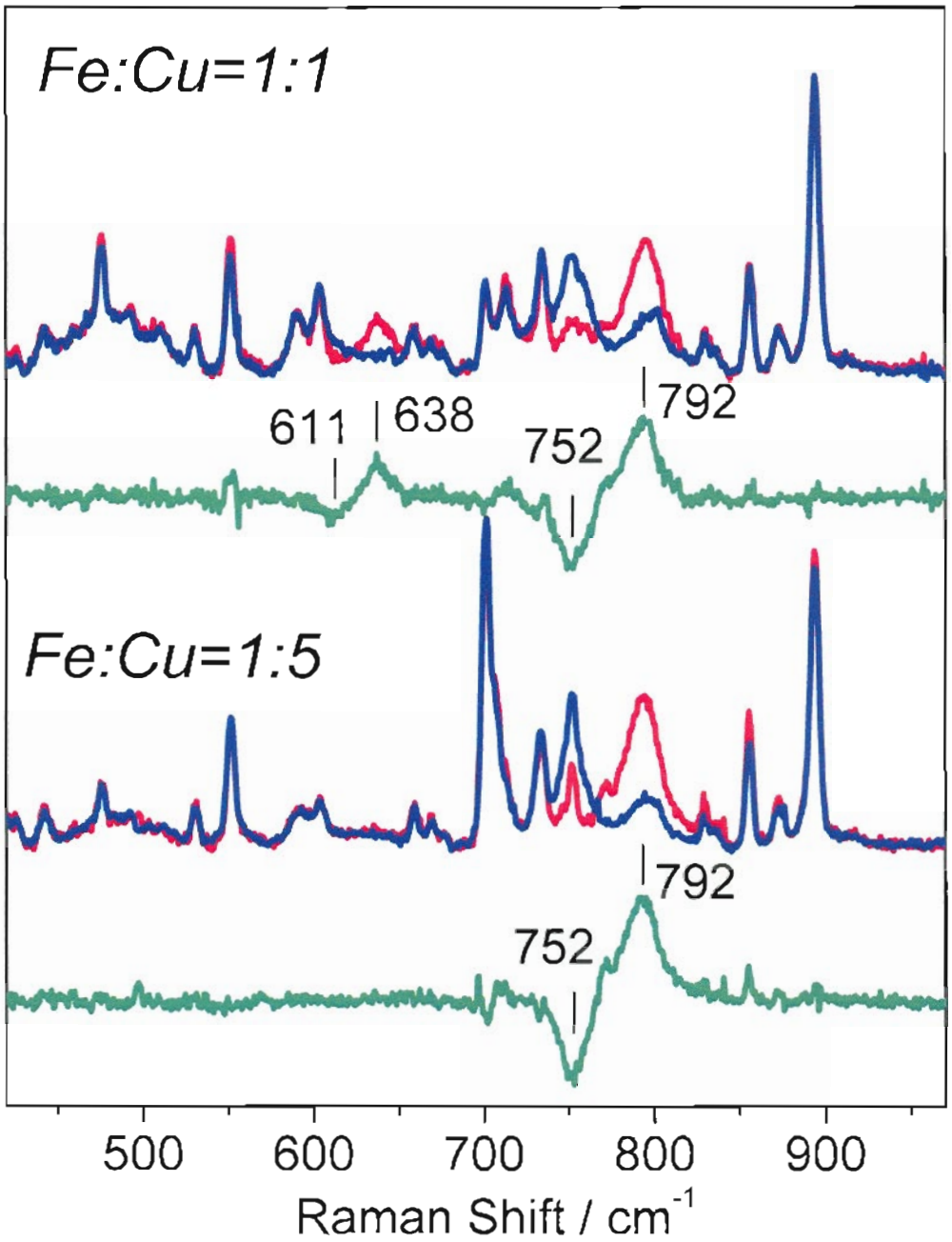

Fig. 2.6 Low-frequency RR spectra of the μ-oxo product and hydroxy product of the O_2 reaction of $(F_8)Fe^{II}$ and $[(L^{Me_2N})Cu^{I}]^+$ obtained with 413-nm excitation at 90 K (solvent: CH_2Cl_2 with 6% EtCN).
- Top traces correspond to a 1:1 mixture of $(F_8)Fe^{II}$ and $[(L^{Me_2N})Cu^{I}]^+$
- Bottom traces correspond to a 1:5 mixture of $(F_8)Fe^{II}$ and $[(L^{Me_2N})Cu^{I}]^+$
- $^{16}O_2$ (red), $^{18}O_2$ (blue), and $^{16}O_2$-$^{18}O_2$ (green).

When Fe and Cu compounds are mixed 1:1, another oxygen isotope sensitive band also shows up at 638 cm^{-1} (-27 cm^{-1}). This band was assigned as a $\nu(Fe^{III}\text{-}OH)$ mode based on its frequency and isotope sensitivity (Fig. 2.6, top trace). The ferric-hydroxyl complex most likely originates from the hydrolysis of some μ-oxo bridge clusters by trace water in EtCN. The Fe(III)-O-Cu(II) μ-oxo species becomes the only ferric product when the amount of Cu loaded is 5 times that of Fe (Fig. 2.6, bottom trace). While non-heme oxo-bridged diiron complexes with equivalent ligand sets show strong ν_s(M-O-M), this mode is not observed in asymmetric structures such as the heme/non-heme dinuclear complexes and it is the asymmetric (Fe-O-Cu) stretch that is resonance enhanced. The observed stretching frequencies, isotope shifts, and Fe-O-Cu angles are in agreement with calculation of secular equations for oxo-metal bridged.

Comparison of low-temperature RR spectra of peroxo species generated in CH_2Cl_2/6% EtCN with $^{16}O_2$ or $^{18}O_2$ reveals two isotopic shifts of ≥ -40 cm^{-1} that identify two bands at 767 and 752 cm^{-1} as putative ν(O-O) peroxo stretching vibrations (Fig. 2.7, left). The latter assignment was confirmed by complementary experiments with scrambled isotope gas mixtures composed of 25% $^{16}O_2$, 50% $^{16}O^{18}O$, and 25% $^{18}O_2$. The expected intermediate frequency of $\nu_{as}(^{16}O\text{-}^{18}O)$ is between $\nu_{as}(^{16}O\text{-}^{16}O)$ and $\nu_{as}(^{18}O\text{-}^{18}O)$ with isotope shifts of about -20 cm^{-1} compared to pure $^{16}O_2$ gas. Large porphyrin vibrations hinder direct visualization of additional bands originating from the $^{16}O\text{-}^{18}O$ peroxo species, but their presence becomes apparent in difference spectra. As expected, the relative intensity of the $\nu_{as}(^{16}O\text{-}^{16}O)$ at 767 cm^{-1} corresponds to 25% of that observed with pure $^{16}O_2$ gas. Similarly, the intensity of the 707 cm^{-1} band obtained from the scrambled gas samples represents 25% of the intensity observed with the pure $^{18}O_2$ gas. We can therefore assign these signals to peroxo ν(O-O), rather than a $\nu(Fe^{IV}\text{=}O)$ stretch or a $\nu(Fe^{III}\text{-}O\text{-}Cu^{II})$, where the dioxygen bond cleavage would have led to intensity ratios ^{16}O:^{18}O signals with 1:1 [Burstyn et al., 1988; Selke et al., 1996]. The RR results clearly establish that two very similar iron-porphyrinate peroxo species with ν(O-O) at 767 and 752 cm^{-1} are present in $[(F_8)Fe^{III}\text{-}(O_2^{2-})\text{-}Cu^{II}(L^{Mc_2N})]^+$.

In the "untethered" $[(F_8)Fe^{III}\text{-}(O_2^{2-})\text{-}Cu^{II}(TMPA)]^+$ and its analog where the TMPA moiety is covalently "tethered" to the heme, $[(^6L)Fe^{III}\text{-}(O_2^{2-})\text{-}Cu^{II}]^+$, we observed significantly different ν(O-O), with frequencies upshifted by 40 to 60 cm^{-1} [Ghiladi et al., 1999; Ghiladi et al., 2001]. The differences in ν(O-O) observed in this series of heme-peroxo-copper complexes is likely related to changes in Fe-O-O angles and possibly a transition from μ-1,2 to μ-η^2:η^2 bridging geometry [Moënne-Loccoz et al., 1999; Brunold et al., 1998]. Our studies reveal that tridentate versus tetradentate copper chelations play a key role in determining the structure and reactivity of the heme-peroxo-copper complex and suggest that the $[(F_8)Fe^{III}\text{-}(O_2^{2-})\text{-}Cu^{II}(L^{Me_2N})]^+$ is a μ-η^2:η^2 complex only stable below 100 K, whereas the $[(F_8)Fe^{III}\text{-}(O_2^{2-})\text{-}Cu^{II}(TMPA)]^+$ adopt a μ-1,2 geometry that is metastable at room temperature.

The observation of two isomers in $[(F_8)Fe^{III}\text{-}(O_2^{2-})\text{-}Cu^{II}(L^{Me_2N})]^+$ may be a result of different conformers caused by different copper ligand orientations with respect to the peroxo ligand. Assuming the copper center has a square-pyramidal geometry, as observed for five-coordinate complexes containing L^R (R = H, MeO, or Me_2N) [Obias et al., 1998], the positioning of the L^{Me_2N} ligand-copper complex in $[(F_8)Fe^{III}\text{-}(O_2^{2-})\text{-}Cu^{II}(L^{Me_2N})]^+$ can present: (*i*) one pyridyl and one alkylamino group or (*ii*) two pyridyl groups *trans* to the peroxo ligand (Fig. 2.8, top).

To confirm this assignment, we characterized the peroxo complex in a tethered $[(^2L)Fe^{II}/Cu^I]^+$ system to limit the geometry of isomers (Fig. 2.8, bottom). As expected, RR spectra of $[(^2L)Fe^{III}\text{–}(O_2^{2-})\text{–}Cu^{II}]^+$ show a single O-O stretching frequency at 747 cm^{-1} ($\Delta(^{18}O_2)$ = -40 cm^{-1}) (Fig 2.7, right). In a $^{16}O\text{-}^{18}O$ mixed isotope experiment, a single band is observed at 730 cm^{-1} between the $^{16}O\text{-}^{16}O$ and $^{18}O\text{-}^{18}O$ stretching bands. The mixed isotope result confirms the peroxo assignment by ruling out ferryl-oxo (Fe=O) and Fe-O-Cu species [Kim et al., 2003; Kim et al., 2004]. Moreover, the presence of a single peroxo geometry allows us to isolate the $\nu(^{16}O\text{-}^{18}O)$ as a single component at 730 cm^{-1}. The lack of splitting of the $\nu(^{16}O\text{-}^{18}O)$ is further confirmed by the intensity of this band which is twice that of the $\nu(^{16}O\text{-}^{16}O)$ and the $\nu(^{18}O\text{-}^{18}O)$. These observations identify the peroxo species as a fully symmetric species and

further support the μ-η^2:η^2 assignments. In conclusion, reduced Fe^{II}-Cu^{I} heme-copper complex, with tridentate Cu^{I}, reacts with dioxygen to give a μ-η^2:η^2 peroxo intermediate with ν(O-O) frequency 40 to 60 cm^{-1} lower than those of heme-peroxo-copper complexes with tetradentate Cu^{I} [Kim et al., 2004; Liu et al., 2004].

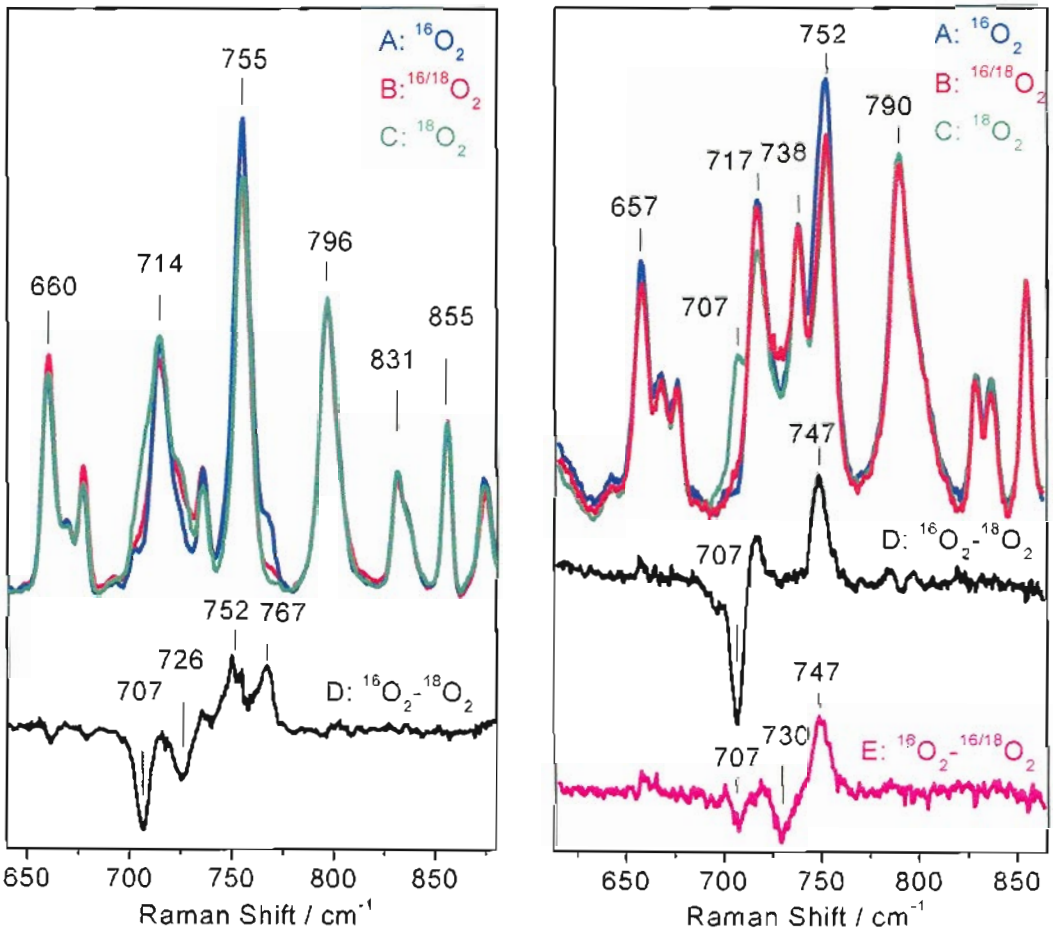

Fig. 2.7 Low-frequency RR spectra of peroxo intermediates obtained with a 413-nm excitation at 90 K (solvent: CH_2Cl_2 with 6% EtCN).
- Left panel: $[(F_8)Fe^{III}\text{-}(O_2^{2-})\text{-}Cu^{II}(L^{Me_2N})]^+$ formed by oxygenation with $^{16}O_2$ (A), a scrambled $^{16}O/^{18}O$ gas containing 25% $^{16}O_2$, 50% $^{16}O^{18}O$, and 25% $^{18}O_2$ (B), and $^{18}O_2$ (C). The difference spectrum A minus C is shown as D.
- Right panel: RR spectra of $[(^2L)Fe^{III}\text{–}(O_2^{2-})\text{–}Cu^{II}]^+$ formed by oxygenation with $^{16}O_2$ (A), a scrambled $^{16}O/^{18}O$ gas containing 25% $^{16}O_2$, 50% $^{16}O^{18}O$, and 25% $^{18}O_2$ (B), and $^{18}O_2$ (C). The difference spectrum of A minus C is shown as D and the difference spectrum of A minus B is shown as E.

Reproduced with permission:

Kim, E., Helton, M. E., Wasser, I. M., Karlin, K. D., Lu, S., Huang, H., Moënne-Loccoz, P., Incarvito, C. D., Rheingold, A. L., Honecker, M., Kaderli, S., and Zuberbuhler, A. D. (2003) Superoxo, μ-peroxo, and μ-oxo complexes from heme/O_2 and heme-Cu/O_2 reactivity: copper ligand influences in cytochrome c oxidase models. *Proc. Natl. Acad. Sci. U. S. A.* **100**, 3623-3628.

Kim, E., Shearer, J., Lu, S., Moënne-Loccoz, P., Helton, M. E., Kaderli, S., Zuberbuhler, A. D., and Karlin, K. D. (2004) Heme/Cu/O_2 reactivity: change in Fe^{III}-(O_2^{2-})-Cu^{II} unit peroxo binding geometry effected by tridentate copper chelation. *J. Am. Chem. Soc.* **126**, 12716-12717.

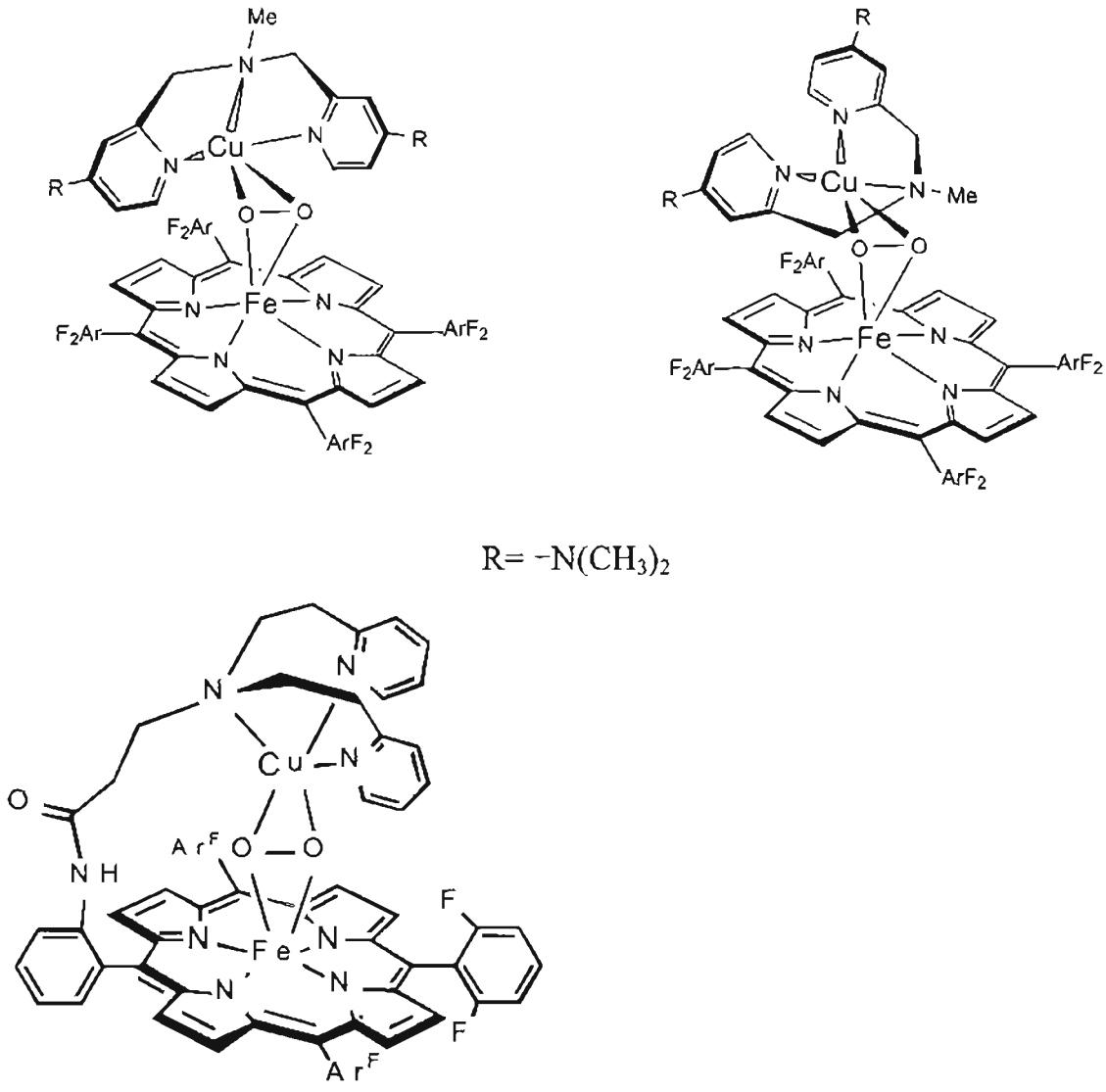

Fig. 2.8 Two side-on peroxo isomers of $[(F_8)Fe^{III}\text{-}(O_2^{2-})\text{-}Cu^{II}(L^{Me_2N})]^+$ (top), and the unique peroxo intermediate of $[(^2L)Fe^{III}\text{-}(O_2^{2-})\text{-}Cu^{II}]]^+$ (bottom).

Reproduced with permission:

Kim, E., Shearer, J., Lu, S., Moënne-Loccoz, P., Helton, M. E., Kaderli, S., Zuberbuhler, A. D., and Karlin, K. D. (2004) Heme/Cu/O_2 reactivity: change in $Fe^{III}\text{-}(O_2^{2-})\text{-}Cu^{II}$ unit peroxo binding geometry effected by tridentate copper chelation. *J. Am. Chem. Soc.* **126**, 12716-12717.

CHAPTER 3

NITROSYL COMPLEXES IN R2 PROTEINS AND THEIR IMPLICATIONS FOR O_2 ACTIVATION*

3.1 O_2 Activation in R2 Diiron Proteins

Subunit R2 of RNR belongs to a class of structurally related proteins that include MMOH and Δ^9D. These metalloenzymes can activate oxygen to carry out reactions that range from the formation of a tyrosine radical in R2, to alkane hydroxylation in MMOH, and to fatty acid desaturation in Δ^9D [Feig and Lippard, 1994; Wallar and Lipscomb, 1996; Solomon et al., 2000]. Four electrons are needed for reduction of dioxygen to water during the O_2-activation. In R2, two of these electrons are from the two iron(II) oxidation to iron(III), another one is from the oxidation of a tyrosine generating a tyrosyl radical, and the last electron comes from external reductants by the intermediate of a tryptophan, W49 [Schlichting et al., 2000; Hersleth et al., 2002].

The crystal structure of apo R2 from *E. coli*, in absence of the metal cofactors, was solved in 1993 [Aberg et al., 1993]. Most of the side chains involved in metal binding and electron transfer form a hydrogen-bonded network in the interior of the protein as no water molecules are bound in the place of the irons in the apo form. Addition of the ferrous iron to the apo protein give the reduced diferrous form of R2,

---

* Material in this chapter has been published in this or similar form in *J. Biol. Inorg. Chem.* and is used here with permission of the Springer publications.

Lu, S., Libby, E., Saleh, L., Xing, G., Bollinger, J. M. Jr., and Moënne-Loccoz, P. (2004) Characterization of NO adducts of the diiron center in protein R2 of *Escherichia coli* ribonucleotide reductase and site-directed variants; implications for the O2 activation mechanism. *J. Biol. Inorg. Chem.* **9**, 818-827.

which is stable under anaerobic conditions [Atkin et al., 1973]. The X-ray structure of the photoreduced form of R2 has been obtained with 1.7-Å resolution [Logan et al., 1996]. In 2003, Voegtli et al. published a new X-ray structure of diferrous R2-wt by using a method that involves soaking crystals of apo protein in solutions of ferrous ammonium sulfate. Crystals subjected to this treatment yielded structures with diiron centers different from those reported previously (Fig. 3.1) [Voegtli et al., 2003]. Comparison of this structure, designated ferrous soaked R2-wt, with that of reduced R2 obtained either by treatment with dithionite or by X-ray photoreduction reveals subtle differences. In both structures, E115 bridges the two Fe(II) ions in a μ-1,3 fashion and each Fe(II) ion is coordinated by the δ nitrogen of a histidine. The average Fe1–O distances for the two side chain oxygen atoms of D84 are 2.0 and 2.7 Å. The electron density is better defined for monomer A, and D84 is best described as a monodentate, terminal ligand. Residue E204 is a monodentate, terminal ligand to Fe2, although the average Fe2–O distance of 2.5 Å, is somewhat long. The corresponding average distance in the structure of the photoreduced protein is 2.3 Å. The E204 coordinated oxygen atom forms hydrogen bonds with the side chain nitrogen atoms of N87 and W111. Similar interactions are also present in the structure of the photoreduced protein, but in this case involve the uncoordinated oxygen atom of E204 [Voegtli et al., 2003].

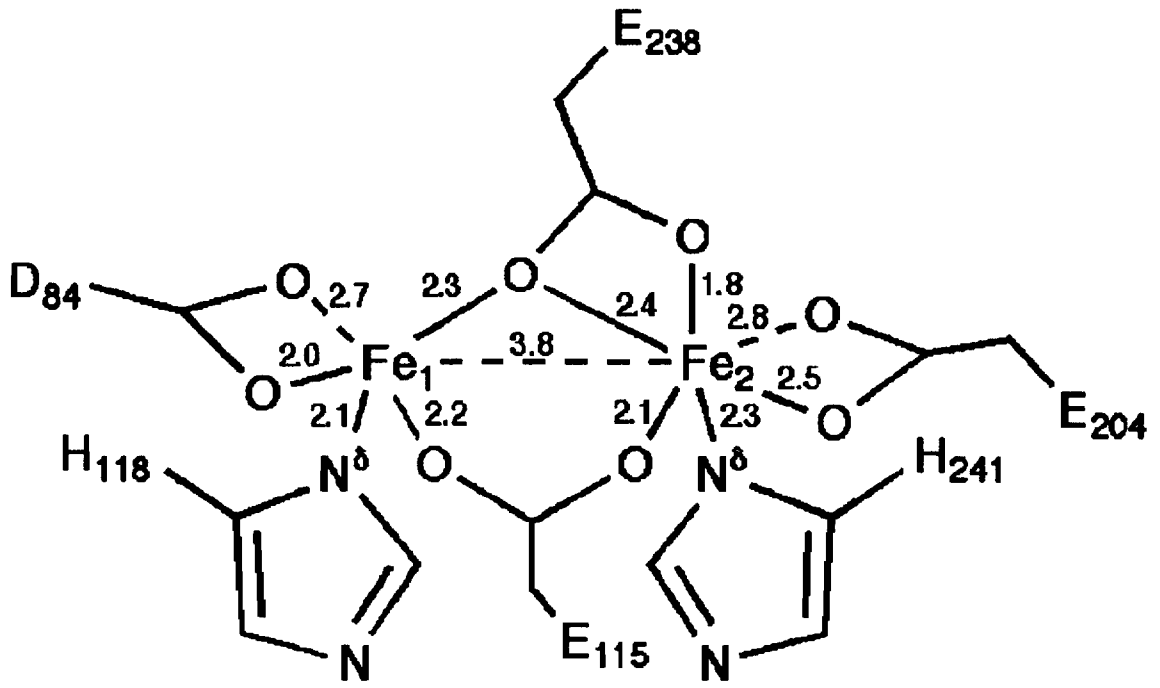

Fig. 3.1 Metal coordination of ferrous wt-R2

Originally published as Fig. 2 in:

Voegtli, W. C., Sommerhalter, M., Saleh, L., Baldwin, J., Bollinger, J. M., Jr., and Rosenzweig, A.C. (2003) Variable coordination geometries at the diiron (II) active site of ribonucleotide reductase R2. *J. Am. Chem. Soc.* **125**, 15822-15830.

If molecular oxygen reacts with the diferrous R2, it will spontaneously oxidize the diiron site and lead to the diferric iron center and a stable tyrosyl radical. Based on the homology to the related diiron protein MMOH, when dioxygen binds the reduced iron center of R2, the oxygen atoms can abstract one electron from each iron and thus forming a peroxo diferric intermediate [Kurtz, 1997; Andersson et al., 1999]. Cleavage of the peroxo complex requires the input of two additional electrons. It has been demonstrated that R2 is dependent on an electron from an external source, e.g. exogenous iron(II) [Covès et al., 1997; Sturgeon et al., 1996], or alternatively, it has been suggested that the source of this electron could be a ferrous iron in the diiron site of the second R2 protomer [Miller et al., 1999; Bollinger et al., 1994a; Bollinger et al., 1994b; Krebs et al., 2000]. Optical, Mössbauer, and RR studies have shown several transient species are formed during oxidation reactions [Liu et al., 1994; Liu et al., 1995a; Broadwater et al., 1998].

In the final step of the activation process, the nearby tyrosyl residue Y122 is oxidized to a stable tyrosyl radical, and the iron site is left in a μ-oxo bridged diferric form, with a water ligand on both irons in *E. coli* R2. The tyrosyl radical can be observed by optical spectroscopy and EPR spectroscopy [Petersson et al., 1980; Galli et al., 1995]. The antiferromagnetically coupled diferric iron center itself is EPR silent, but it gives rise to a characteristic oxo-to-iron charge transfer transition with a broad optical spectrum with maxima at 325 and 370 nm.

The met form R2 where the tyrosine radical is re-reduced is generated spontaneously upon storage of the purified iron-containing protein in solution, and therefore, all crystal structures of oxidized protein have been of the met-R2 state. The met-R2 state can also be generated by selective reduction of the tyrosyl radical using hydroxyurea [Karlsson et al., 1992]. In the crystal structure of *E. coli* met-R2, the iron center is dibridged and the two irons have an octahedral coordination by two histidines, three glutamic acids, one aspartic acid, an oxide ion and two water molecules [Nordlund and Eklund, 1993a]. The distance between the two iron atoms is around 3.3 Å in met-R2. In the original met-R2 structure [Nordlund et al., 1990], both the metals

in the diiron center were assigned as being six-coordinate; however, in a more recently solved high-resolution structure (1.42 Å) Fe1 is 5-coordinate [Hogbom et al., 2003]. In brief, the flexibility of the diferrous cluster is well documented, leaving us unsure of how O_2 might bind to the diiron site. The characterization of substrate analog complexes can bring complementary information to address this question and help us determine the coordinates of the O_2-reaction.

3.2 Peroxo Intermediate in R2 Proteins

A symmetric peroxo adduct is a possible common intermediate to the O_2 activation process in this family of enzymes [Moënne-Loccoz et al., 1999; Moënne-Loccoz et al., 1998a; Broadwater et al., 1998]. This blue colored peroxo intermediate, with a optical absorption maximum between 650-750 nm due to a peroxide-to-Fe^{III} charge transfer transition, has been observed during oxygen activation by the diiron center in MMOH [Liu et al., 1994; Liu et al., 1995b; Ravi et al., 1994], and in Δ^9D although the peroxo complex is catalytically inefficient and leads to an oxidase reaction without substrate desaturation [Broadwater et al., 1999]. In the R2 protein, there is no conclusive evidence for the presence of a peroxo intermediate in the wild type, but this species was observed in the variant proteins R2-D84E and R2-W48F/D84E [Bollinger et al., 1998; Moënne-Loccoz et al., 1998a; Riggs-Gelasco et al., 1998]. The crystal structures of these mutants of R2 in the fully reduced form revealed a very close similarity in the coordination sphere of the diferrous center to that of reduced MMOH.

In the double variant R2-W48F/D84E, the μ-1,2 peroxo diiron(III) intermediate species has been characterized and was shown to lead to the hydroxylation of the phenyl side chain of F208 at the vicinity of the diiron site [Moënne-Loccoz et al., 1998a; Baldwin et al., 2001]. Thus, the O_2 reaction of this double variant R2 is more akin to the reaction of MMOH than that of wild-type R2, in which no significant build-up of a peroxodiiron(III) species is observed. Involvement of a structurally

homologous peroxodiiron(III) intermediate in the reaction pathway of wt-R2 remains uncertain, and reaction mechanisms where such an intermediate is bypassed can be envisioned. For instance, a ferric superoxo species might be reduced by the nearby W48 before recruitment of the other Fe(II) ion into the reaction. Alternatively, a peroxo diferric intermediate may be inaccessible in wt-R2 from *E. coli* for kinetical reasons, but it may still correspond to a transient species, essential to catalysis. To answer these questions, we have used NO as an analog to O_2, and we characterized nitrosyl adducts that suggest that a symmetric diferric peroxo species forms in wt-R2.

3.3 Nitrosyl Complex of R2 as a Peroxo Intermediate Analog

NO has been widely used as an analog of O_2 in iron containing proteins because it often forms stable $\{FeNO\}^7$ nitrosyl adducts [Richter-Addo, 2002]. In heme nitrosyl complexes, the $\{FeNO\}^7$ species are $S = 1/2$ and are best described as low spin Fe^{2+}-NO complexes. On the other hand, the non-heme iron nitrosyl complexes are $S = 3/2$ with a high spin Fe(III) ($S = 5/2$) antiferromagnetically coupled to NO^- ($S = 1$) [Brown et al., 1995]. The quality of NO as a reporter for O_2 binding is exemplified in hemerythrin (Hr), a respiratory diiron protein of several phyla of marine organisms [Stenkamp et al., 1985]. As opposed to diiron proteins like R2, only one Fe(II) in deoxyHr presents an open coordination site, whereas the other iron is six-coordinate. Exposure of deoxyHr to O_2 leads to the formation of a stable (μ-oxo)-(hydroperoxy)diiron(III) complex upon abstraction of the proton from the μ-hydroxy group of the diiron(II) reactant by the terminal peroxide moiety [Holmes et al., 1991; Kurtz, 1999]. The hydroperoxide is believed to hydrogen bond with the μ-oxo group in this complex. When NO is substituted for O_2, an end-on nitrosyl $\{FeNO\}^7$ is formed, and it also engages a H-bond interaction which is likely to involve the μ-hydroxo bridge (Fig. 3.2) [Nocek et al., 1984; Nocek et al., 1988].

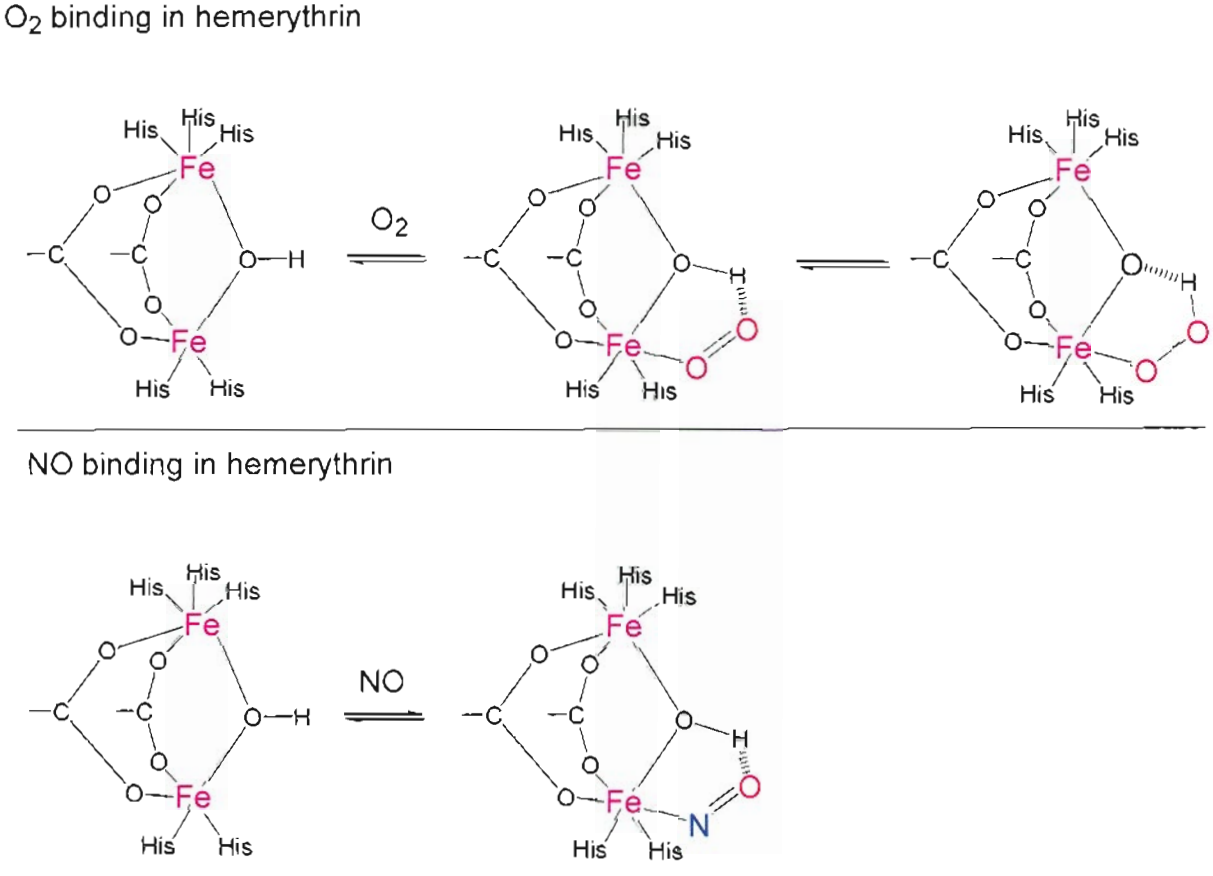

Fig. 3.2 Proposed mechanism for reversible O_2 binding to Hr, and proposed structure for the nitrosyl complex of deoxyHrNO [adapted from Nocek et al., 1988].

In wt-R2, MMOH, and Δ^9D, where the diiron clusters have open coordination sites on both Fe(II), NO can be expected to bind to both Fe(II). Indeed, EPR and Mössbauer characterization of the reaction of NO with R2 and MMOH has brought evidence in favor of the formation of two antiferromagnetically coupled $\{FeNO\}^7$ species [Haskin et al., 1995; Coufal et al., 1999]. There is no submolecular structural information on these NO adducts in MMOH and R2, but an iron-nitrosyl dimer complex was characterized in a carboxylate-bridged non-heme diiron model, Fe_2(Et-HPTB)$(O_2CPh)(NO)_2$, in which two symmetrically positioned [Fe-N-O] units have identical (Fe-N-O) angles of 167° and produce a single ν(N-O) at 1785 cm^{-1}. Its corresponding peroxo adduct, $[Fe_2$(Et-HPTB)$(O_2CPh)(O_2)](BF_4)_2$, is stable only at temperatures below -20℃ [Feig et al., 1996].

3.4 Materials and Methods

The overexpression and purification of wt and variant apo R2 proteins was performed as previously described [Moënne-Loccoz et al., 1998a; Voegtli et al., 2000; Parkin et al., 1998]. The apo proteins were made anaerobic by prolonged purging with argon, and three equivalents of iron (per protein dimers) were added minutes before the addition of NO gas to the headspace. ^{14}NO (purchased from Aldrich) and ^{15}NO (purchased from ICON) gases were bubbled through a 0.1 M KOH solution to remove higher nitrogen oxides (Eq. 3.1).

$$2NO_2 + 2OH^- \rightarrow NO_3^- + NO_2^- + H_2O \quad \text{(Eq. 3.1)}$$

Formation of the nitrosyl adducts was followed by UV-vis spectroscopy in the same Raman capillary cell using a Cary 50 spectrophotometer. RR, FTIR and EPR experiments were performed at enzyme concentrations ranging from 0.5 to 0.7 mM in 50 mM Hepes buffer at pH 7.5 and 5% glycerol. After completion of the RR experiments, the UV-vis spectra were checked to confirm the stability of the complex during the laser illumination.

RR spectra were obtained on a custom McPherson 2061/207 spectrograph (set at 0.67 m with variable gratings) equipped with a Princeton Instruments liquid-N_2-cooled CCD detector (LN-1100PB). Excitation sources consisted of an Argon ion laser (458 nm) and an Innova 302 krypton laser (413 nm). Spectra were collected on samples at room temperature. Frequencies were calibrated relative to aspirin, indene and CCl_4 standards and are accurate to ± 1 cm^{-1}.

The FTIR samples were prepared using the same procedures as in the RR experiments. An 11-μL droplet of the NO-treated samples was deposited on a CaF_2 window in an anaerobic glove box (Coy laboratory products, Inc.). A second CaF_2 window was dropped on the sample to form an optical cell with a pathlength controlled by a 15-μm Teflon spacer. Once the IR cell was securely mounted, the formation of the NO adduct could be confirmed by obtaining its UV-vis spectrum using a Cary 50 spectrophotometer. While the variant proteins form irreversible NO adducts and can be observed at high concentration in the FTIR cell, it is not so with the wt protein since NO binds reversibly to the wt active site. Indeed, exposure of the NO-treated wt sample as a droplet results in a rapid diffusion of free NO to the gas phase. For low temperature experiments, the same IR cell used at room temperature was attached to a closed cycle cryogenic system (Displex, Advanced Research Systems, Inc.). The FTIR spectra were obtained on a Perkin-Elmer system 2000 equipped with a liquid-N_2 cooled MCT detector. Sets of 1000-scan accumulations were acquired at a 4-cm^{-1} resolution. For room temperature experiments, the cell was filled with buffer for background subtraction. For low-temperature photodissociation of the NO adducts, continuous illumination of the samples was performed directly in the FTIR sample chamber with a 50 W tungsten lamp after filtering out heat and NIR emission.

EPR spectra were obtained on a Bruker E500 X-band EPR spectrometer equipped with a superX microwave bridge, a superhigh Q cavity, and a helium flow cryostat (Helitran, Advance Research Systems, Inc.). The experimental conditions were as follows: temperature, 8 K; microwave frequency, 9.23 GHz; microwave

power, 0.02 mW; modulation frequency 100 KHz; and modulation amplitude, 10 G. Quantitation of the EPR signals was carried out by double integration under non-saturating conditions and comparison with a 1.0 mM and 0.3 mM Cu^{II}-EDTA standards.

3.5 Spectroscopic Studies of the Active-Site Nitrosyl Complex

The R2 subunit of *E. coli* RNR contains a diiron site that reacts with O_2 to produce side chain radicals. In wt-R2, the first observable reaction intermediate is a high-valent [Fe^{III}-Fe^{IV}] state called compound X, but in related diiron proteins such as MMOH, Δ^9D, and ferritin, peroxodiiron(III) complexes have been characterized. Substitution of iron ligand D84 by E within the active site of R2 allows an intermediate (μ-1,2-peroxo) diiron species to accumulate. To investigate the possible involvement of a bridging peroxo species within the O_2 activation sequence of wt-R2, we characterized the iron-nitrosyl species that form at the diiron sites in wt-R2, D84E-R2, and W48F/D84E-R2 by using vibrational spectroscopy.

Previous work has shown that the diiron center in wt-R2 binds one NO per iron to form an antiferromagnetically coupled [{FeNO}^{7}]$_2$ center [Haskin et al., 1995]. In the wt and variant proteins, we also observe that both irons bind one NO to form a {FeNO}^{7} dimer where both Fe–N–O units share a common vibrational signature. In the wt protein, ν(Fe-NO), δ(Fe-N-O), and ν(N-O) bands are observed at 445, 434 and 1742 cm^{-1}, respectively, while in the variant proteins the ν(Fe-NO) and δ(Fe-N-O) bands are observed ~10 cm^{-1} higher and the ν(N-O) ~10 cm^{-1} lower at 1735 cm^{-1}. These results demonstrate that all three proteins accommodate fully symmetric [{FeNO}^{7}]$_2$ species with two identical Fe–N–O units. The formation of equivalent NO adducts in the wt and variant proteins strongly favors the formation of a symmetric bridging peroxo intermediate during the O_2 activation process in wt-R2.

UV-vis Spectra

Anaerobic exposure of apo-wt R2, D84E-R2, and D84E/W48F-R2 with Fe(II) and NO gas results in the appearance of new UV-vis absorption features at ~350, ~450, and ~620 nm (Fig. 3.3). These electronic transitions are consistent with nitrosyl to iron charge transfer transitions in $\{FeNO\}^7$ species [Arciero et al., 1985; Arciero and Lipscomb, 1986]. The intensity of these three bands are comparable in the two variant proteins, but only ~60% of that intensity is reached at ~450 and ~620 nm in the wt protein. In all three proteins, the characteristic absorption band at ~450 nm reaches a maximum within the first minute of mixing and remains constant for at least ½ hr at room temperature. The difference in optical density at ~450 nm is due to a difference in NO affinity of the wt diiron site. Indeed, extended vacuum argon-purged cycles of the NO-treated variant proteins has no effects on their absorption spectra, but with the wt enzyme the ~450-nm absorption is greatly decreased, indicating a reversible binding of NO in wt-R2. Reversibility of NO binding was also observed at the non-heme Fe(II) centers in extradiol catechol dioxygenase, lipoxygenase [Nelson, 1987], and superoxide reductase [Clay et al., 2003]. Chiou and Que also showed that irreversible binding of NO to a non-heme iron model is rendered reversible when the three pyridines that compose the tripodal ligand are methylated. The difference in affinity was assigned to a +500 mV shift of the Fe(III)/Fe(II) redox potential [Chiou and Que, 1995a; Chiou and Que, 1995b].

Addition of more than 3 equivalent of Fe does not result in an increase of the 450-nm absorption feature, but it increases the absorption in the near-UV. Further spectroscopic characterization allows us to assign this additional absorption to a $(Cys)_2Fe(NO)_2$ species distinct from the protein diiron active site. Prolonged incubation at high NO concentration also results in an increase in absorption below ~400 nm; this absorption increase corresponds to a growth in diffusion background that may be assigned to protein aggregation promoted by adventitious reaction of NO with protein side chains. A precise quantitative interpretation of the UV-vis characteristics of the NO adducts in the wt and variant proteins is further complicated

by the slow and substoichiometric turnover of the $\{FeNO\}^7$ species formed at the diiron site of wt-R2. Que and collaborators have shown that decay of the NO adducts in wt-R2 is associated with N_2O formation [Haskin et al., 1995]. This NO reductase activity corresponds to a 2-electron reduction of two molecules of NO, and it converts the enzyme into the met form in which the two iron(III) are bridged by a μ-oxo group. Indeed, a slow development on the hour time scale of the characteristic oxo-to-Fe(III) charge transfer bands is observed at 325 and 370 nm.

Although exact extinction coefficients cannot be obtained for the $\{FeNO\}^7$ species formed here due to the problems listed above, and some of these issues might also affect values reported in the literature, a qualitative interpretation of the observed UV-vis absorption intensity is informative. If we assume that two molecules of NO bind at the diiron site protein, i.e. the totality of the ferrous iron added to the variant apoproteins forms $\{FeNO\}^7$ species (and 60% in the wt protein), we calculate a ε_{450} = 1,200 $M^{-1}cm^{-1}$ in agreement with values observed in other iron proteins. Assuming a single NO molecule binds per diiron sites leads to a ε_{450} = 2400 $M^{-1}cm^{-1}$, which is inconsistent with values reported so far. These values range from ~1800 $M^{-1}cm^{-1}$ in the mononuclear non-heme iron protein protocatechuate 3,4-dioxygenase [Orville and Lipscomb, 1993; Wasinger et al., 2003], to 800 $M^{-1}cm^{-1}$ in isopenicillin N synthase [Chen et al., 1989], and 530 M^{-1} cm^{-1} in superoxide reductase [Clay et al., 2003]. Reported extinction coefficients at ~450 nm for $\{FeNO\}^7$ species formed in diiron proteins range from 1200 $M^{-1}cm^{-1}$ in Hr, to 760 $M^{-1}cm^{-1}$ in wt-R2, and 740 $M^{-1}cm^{-1}$ in MMOH.

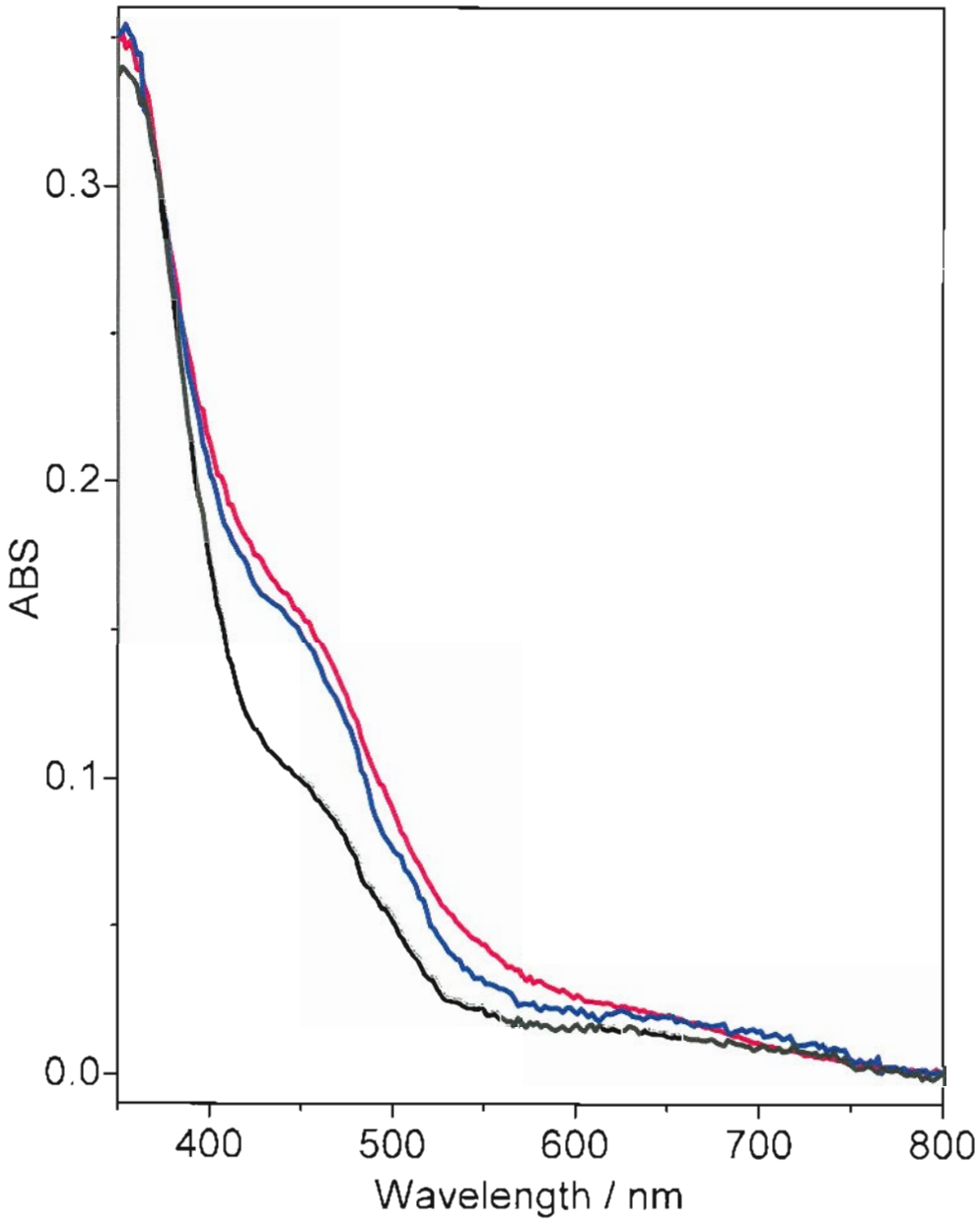

Fig. 3.3 UV-vis absorption spectra of the NO adducts formed in wt-R2 (black), D84E-R2 (blue) and W48F/D84E-R2 (red). In each case, the final concentration of protein was 0.45 mM, 3 equiv Fe(II) was added, and the final concentration of free NO in solution was ~2 mM. The apparent pathlength in the Raman capillaries was ~0.1 cm.

EPR Spectra

Potential iron-nitrosyl complexes that might form in non-heme diiron proteins and their expected EPR signatures are listed in Table 3.1. The EPR spectrum of the NO adducts in wt-R2 shows several components with $g = 4.08$, and $g = 2.04$ (Fig. 3.4). The NO-treated variant proteins show comparable EPR signals with only subtle differences in the relative intensities between the different components of the spectra, and differences in exact g values of the $g \sim 4$ signal. Quantitation of these EPR signals indicates that at least 80% of the Fe added is EPR silent. Similar EPR results with NO-treated wt-R2 were reported earlier by Que and collaborators [Haskin et al., 1995]. The UV-vis data have shown that the great majority if not all of the Fe(II) added to the variant protein forms NO adducts. These $\{FeNO\}^7$ species are rendered EPR silent via antiferromagnetic coupling at the diiron site. In the wt enzyme where only ~60% of $\{FeNO\}^7$ species are formed, the remaining iron unaccounted for by EPR quantitation is predicted to be in the equally EPR-silent diferrous state. These quantitations are consistent with the RR data described in the next section.

species	spin number	*g* value	R2 samples
$\{FeNO\}^7$	$(5/2\ Fe^{III}) - (1\ NO^-) = 3/2$	4.2 - 4.1	< 15%
$Fe^{II}\{FeNO\}^7$	$(2\ Fe^{II}) - (3/2\ \{FeNO\}^7) = ½$	2	not observed
$(\{FeNO\}^7)_2$	$(3/2\ \{FeNO\}^7) - (3/2\ \{FeNO\}^7) = 0$	Silent	> 80%
$\{Fe(NO)_2\}^9$	$(1/2\ Fe^I) - (0\ 2NO^+) = ½$	2.04	3%

Table 3.1 Potential iron-nitrosyl complexes in R2

The EPR signals at $g \sim 4$ correspond to $S = 3/2$ species characteristic of a mononuclear $\{FeNO\}^7$ complex formally described as a $S = 5/2$ high-spin ferric center antiferromagnetically coupled to an $S = 1$ NO^- ligand [Brown et al., 1995]. These EPR-active species are likely to originate from partial occupancy of the diiron sites, and they represent less than 15% of the total iron added. Indeed, Mössbauer spectroscopy

has shown that one site of the cluster (proposed to be Fe2 in the nomenclature used in structures of R2) has a greater affinity and that mononuclear species with Fe(II) bound only at this site can be prepared [Bollinger et al, 1997]. In wt-R2, the derivative signal maximizes at $g = 4.08$ while it is at $g = 4.26$ in the variant proteins. This slight increase in rhombicity in the variant proteins indicates that the mononuclear site is different in these proteins than in wt-R2. This difference might reflect the binding of the single Fe(II) to opposite sites in R2-wt and the D84E variants, but crystal structures of D84E-R2 and D84E/Y122F-R2 partly loaded with Fe(II) suggest that the same Fe2 site is preferentially occupied [Voegtli et al., 2003].

Another EPR signal observed at $g = 2.04$ and 2.03 represents less than 3% of the iron added and is characteristic of $(RS)_2$-Fe-$(NO)_2$ species [McDonald et al., 1965]. Crystal structures of wt-R2 show that several cysteine side chains are surface exposed and may allow the formation of intermolecular complexes [Nordlund et al., 1990; Nordlund and Eklund, 1993; Logan et al., 1996]. Intramolecular complexes might be formed as well: within an R2 monomer, C268 and C272 appear to be in sufficiently close proximity to allow the formation of such a dithiol-dinitrosyl iron species. The signal at $g = 1.98$ is due to free NO in solution. The free NO signal varies slightly in intensity from sample to sample, and we suspect it may relate to differences in the freezing time.

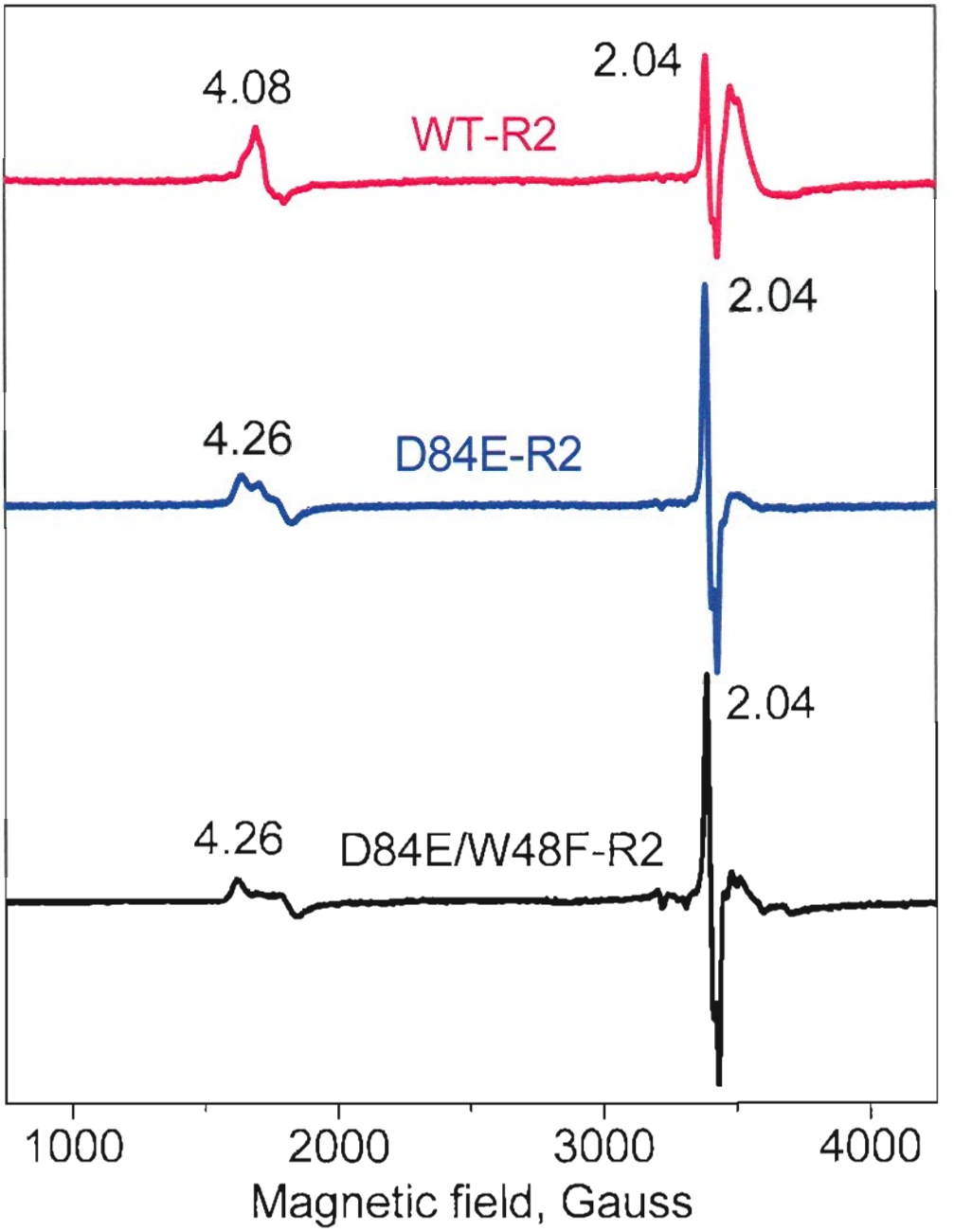

Fig. 3.4 EPR spectra of the NO adducts formed in wt-R2 (top), D84E-R2 (middle), and W48F/D84E-R2 (bottom). In each case, the protein concentration was 0.2 mM, the apo protein was preloaded with 3 equiv Fe(II), and the concentration of free NO in solution was ~2 mM.

RR Spectra

Room temperature RR spectra were obtained using a 458-nm excitation within the 450-nm absorption band of the NO adducts of wt and variant R2 proteins (Fig. 3.5). In the RR spectra of wt-R2, a band at 445 cm^{-1} shifts to 438 (-7) cm^{-1} with ^{15}NO isotope labeling. Two other isotope sensitive bands are observed at 879 and 1742 cm^{-1} with downshifts of 16 and 29 cm^{-1}, respectively. Three corresponding isotope sensitive bands are observed in the variant R2-D84E and R2-D84E/W48F (Fig. 3.5 and Table 3.2). The vibrations observed between 445 and 455 cm^{-1} are assigned to ν(Fe-NO), which are usually more strongly enhanced than δ(Fe-N-O), and the isotope sensitive bands observed between 1735 and 1742 cm^{-1} are assigned to ν(N-O). The observed ^{15}N-isotope shifts are consistent with these assignments. For each protein, one additional isotope sensitive band is observed between 875 and 900 cm^{-1}. These frequencies are outside the range of any fundamental vibrational modes of a [Fe-N-O] unit. On the basis of their large N-isotope sensitivity, we assign these signals to combination bands between the Fe-N-O stretching and bending modes. The deduced δ(Fe-N-O) frequencies are 434 cm^{-1} in wt-R2 and 442 cm^{-1} in D84E-R2 and D84E/W48F-R2, with ^{15}N-isotope shifts between -9 and -8 cm^{-1} (Table 3.2). It is noteworthy that in Figure 3.5, the RR spectra are normalized on a sharp and relatively intense band observed at 1004 cm^{-1}. This non-resonant Raman vibration corresponds to the breathing mode of phenyl rings from the fifteen phenylalanine side chains present in wt-R2 (Fig. 3.5). Using this internal standard, comparison of the intensity of the Fe-N-O stretching vibrations in the three R2 proteins confirms that only 60% of $\{FeNO\}^7$ species forms in wt-R2 compared to the variant proteins.

The observed frequencies are consistent with a $S = 3/2$ $\{FeNO\}^7$ species, and, along with a recent characterization of the nitrosyl complex formed at the mononuclear non-heme iron site of superoxide reductase (SOR) [Clay et al., 2003] and iron site of superoxide dismutase (FeSOD), they represent the only set of ν(N-O) and ν(Fe-NO) frequencies determined in a non-heme iron protein. An extensive set of frequencies is available for $\{FeNO\}^7$ species in hemoproteins and porphyrin models

[Vogel et al., 1999; Park et al., 2000; Coyle et al., 2003], but heme $\{FeNO\}^7$ species adopt a $S = 1/2$ low-spin configuration, and the influences of structural parameters on their vibrational frequencies remain controversial. The ν(Fe-NO), δ(Fe-N-O) and ν(N-O) observed in the NO adducts of wt and variant R2 proteins are within the range of frequencies reported so far for bent $S = 3/2$ $\{FeNO\}^7$ (Table 3.2). The variation in frequencies between the wt and variant proteins indicates an increase in electron density donated from the NO to the iron in the variant proteins.

The most striking observation is that for each protein, the RR data reveal a single [Fe-N-O] unit. The absence of any broadening of the RR bands indicates that if both $\{FeNO\}^7$ species that form at the diiron sites contribute to the spectra, they must adopt very similar configurations to form a symmetric $[(Fe\text{-}NO)]_2$ cluster. The only alternative interpretation of the RR results, where one of the [Fe-N-O] unit within the $[(Fe\text{-}NO)]_2$ cluster is RR silent, can be ruled out. First, the absorption intensity at ~450 nm indicates that both [Fe-N-O] units contribute to this absorption feature, and there is therefore no reason to believe the 458-nm excitation might not provide for resonance enhancement to one of these chromophoric species. Second, we have repeated the RR experiments using different laser excitations. Substituting the 458-nm excitation with a 442-nm laser line produced nearly identical RR data, with no variations in the shapes or positions of the isotope sensitive bands and no new RR bands. With a 413-nm excitation, the three isotope sensitive bands enhanced with excitation within the 450-nm ligand to metal charge transfer (LMCT) band are very weak and barely detected above the non-resonant signals. Finally, as detailed in the next section, although additional ν(N-O) signals were detected by FTIR spectroscopy, none originated from an iron nitrosyl species at the diiron site.

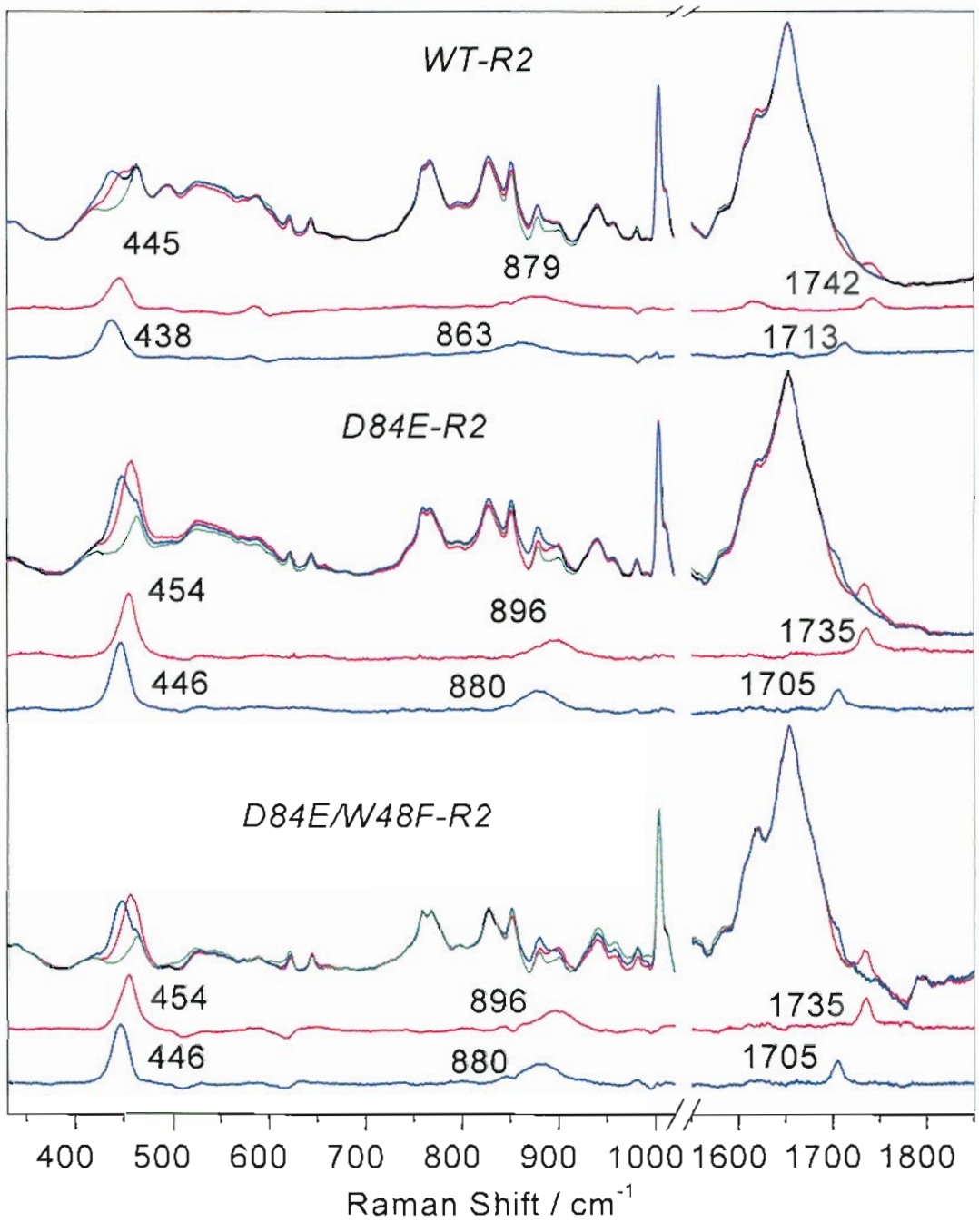

Fig. 3.5 Room temperature RR spectra of wt-R2, D84E-R2, and W48F/D84E-R2. For each protein, the spectra of the Fe(II) loaded (green), ^{14}NO adduct (red), and ^{15}NO adduct (blue) are shown, as well as the ^{14}NO adduct minus Fe(II) loaded (red) and the ^{15}NO adduct minus Fe(II) loaded (blue) difference spectra. Minor signals at 490 and 590 cm^{-1} in wt-R2 correspond to ν_s(Fe-O-Fe) of the resting and photoactivated μ-oxo diferric cluster formed by reaction of the reduced enzyme with trace O_2 contamination.

{FeNO}^{7}	ν(Fe-NO) (Δ^{15}N)	δ(Fe-N-O) combination band	ν(N-O) (Δ^{15}N)
Hr[a]	433 (-6)	421 (-6)	Not observed
wt-R2[b]	445 (-7)	434 (-9), 879 (-16)	1742 (-29)
D84E-R2[b]	454 (-8)	442 (-8), 896 (-16)	1735 (-30)
D84E/W48F-R2[b]	454 (-8)	442 (-8), 896 (-16)	1735 (-30)
SOR[c]	475 (-7)		1721 (-31)
Fe(NO)(Me_3TACN)(N_3)$_2$[d]	497 (-8)		1712 (-31)
FeSOD[e]	482 (-7)	469 (-7), 951 (-14)	1774 (-30)

Table 3.2 Vibrational frequencies of iron nitrosyl complexes

[a] [Nocek et al., 1988]

[b] [Lu et al., 2004b]

[c] [Clay et al., 2003]

[d] [Brown et al., 1995]

[e] [Jackson et al., 2003; Lu et al., unpublished results]

The RR experiments described above were carried out with 3 equiv of iron, where 2 equiv are expected to form a $[\{FeNO\}^7]_2$ cluster to which we assigned the observed Fe-N-O vibrations. The fate of the remaining 1 equiv of iron remains unclear. This substoichiometric amount of iron is used because the theoretical value of 4 Fe(II) per R2 homodimer is never achieved, and 3.0-3.2 iron per dimer is the maximum loading capacity of R2 proteins [Lynch et al., 1989; Ochiai et al., 1990; Ravi et al., 1994]. Accordingly, experiments with 3 and 4 equiv give identical RR spectra. Recently, Hendrich and coworkers [Pierce et al., 2003] have shown that the binding of iron(II) in the R2 homodimer is a strongly anticooperative process and that two iron(II) are loaded in one protomer while loading of the other protomer occurs only during the O_2 activation. It is not known if the reaction with NO, akin to that with O_2, allows for the loading of the second protomer.

To clarify this issue we compared the RR spectra of apo-R2 samples loaded with 1 and 2 equiv of iron before the exposure to NO (Fig. 3.6). In these spectra, the three ^{15}N isotope-sensitive signals are observed with no change in frequency or bandwidth. After normalization of these spectra with the phenylalanine non-resonant Raman band, the relative intensity of the Fe-N-O vibrational modes were compared. With 1 equiv of iron(II), the Fe-N-O vibrational bands already represent 55±10% of the intensity observed with 2 equiv of iron, while variation in intensity between samples produced with 2, 3, or 4 equiv are within the margin of error of the experiments. Thus, the RR data confirm that only 2 equiv of iron(II) bind per R2 proteins and they show that the reaction of this diiron(II) cluster with NO does not allow the binding of additional iron at the second protomer.

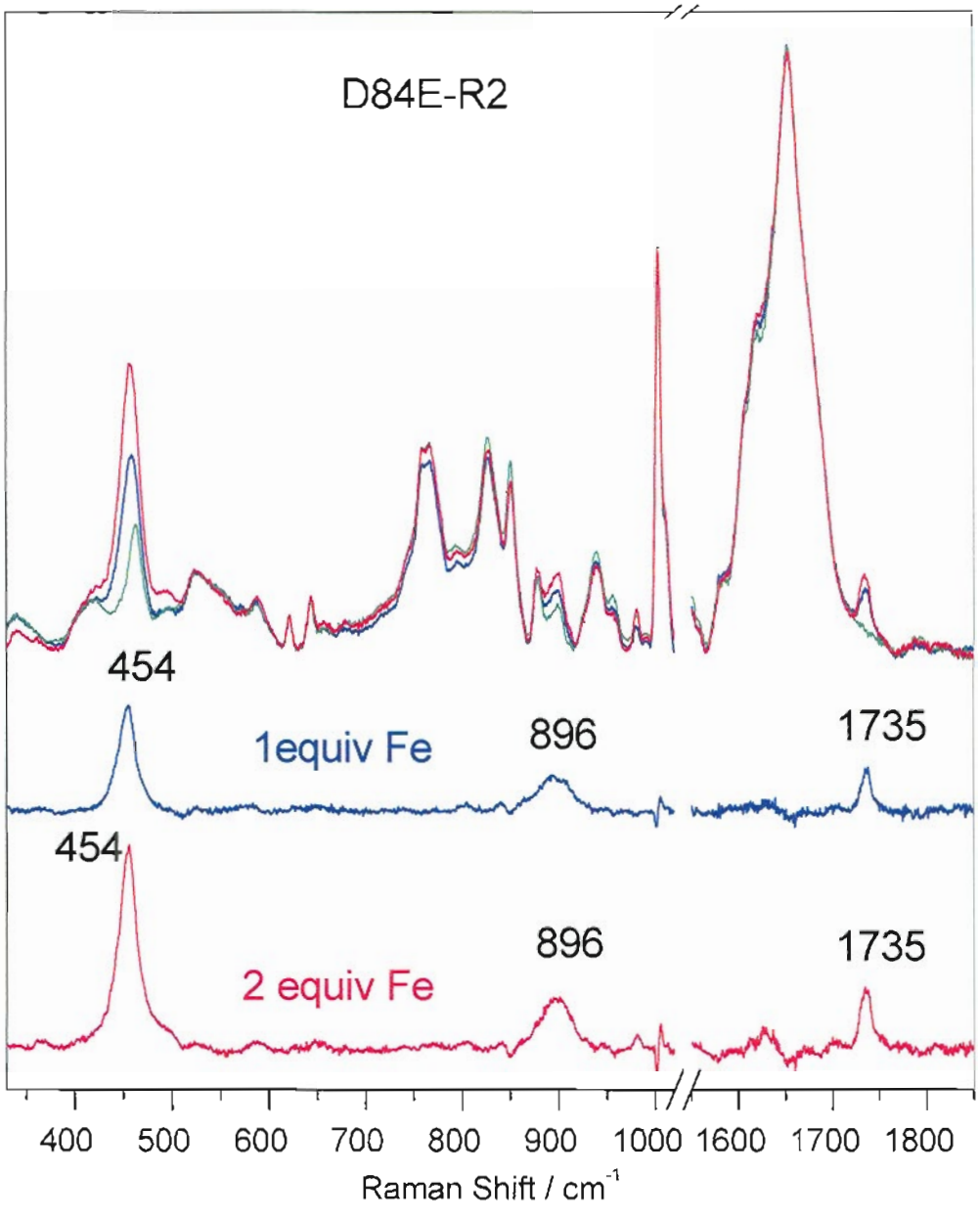

Fig 3.6 Room temperature RR spectra of R2-D84E loaded with 2 equiv of Fe(II) (green), loaded with 1 equiv of Fe(II) and exposed to NO (blue), and loaded with 2 equiv of Fe(II) and exposed to NO (red) are shown, as well as the 1 equiv iron loaded NO adduct minus Fe(II) loaded (blue) and the 2 equiv iron loaded NO adduct minus Fe(II) (red) difference spectra. The NO adduct in R2-wt shows the same changes in the relative intensity of its Fe–N–O vibrations with 1 and 2 equiv of iron.

FTIR Spectra

To provide further confirmation for the symmetric nature of the $[\{FeNO\}^7]_2$ clusters formed in the wt and variant R2 proteins, these complexes were also characterized by FTIR spectroscopy. At 20 °C, the NO stretches are isolated by subtraction of a buffer blank (Fig. 3.7, left). In wt-R2, the nitrosyl complex is labile and significant dissociation takes place during the mounting of the FTIR cell. Samples loaded with 3 equiv Fe(II) show no ν(N-O) bands above the background signal. In the variant proteins, NO binds irreversibly to the diiron site, and one strong ν (N-O) band is observed within a few cm^{-1} from the ν(N-O) observed in the RR spectra and is readily assigned to the same $\{FeNO\}^7$ species at the diiron site.

It is much more difficult to produce good FTIR blanks with frozen samples at cryogenic temperatures than with samples in the liquid state. Despite these experimental problems, difference spectra against blanks are of sufficient quality to confirm that the species observed at 20 °C also form at 15 K. Difference spectra of much higher quality can be obtained by taking advantage of the photolabile character of metal-bound exogenous ligand [Bagley et al., 1994]. Light induced FTIR difference spectra of NO-treated wt and variant R2 proteins display a single ν(N-O) that corresponds within 3 cm^{-1} to the one observed in the RR experiments (Fig. 3.7, right). The observed frequencies at 15 K are downshifted 3 cm^{-1} from those measured at room temperature, and no other feature appears in the low temperature difference spectra. These results provide an overlap between experiments carried out at room temperature (UV-vis and RR spectroscopy) and cryogenic temperatures (EPR spectroscopy) and allow us to conclude that the $[\{FeNO\}^7]_2$ species formed at the diiron active site adopt a symmetric geometry in which both iron-nitrosyl groups display identical vibrational signatures.

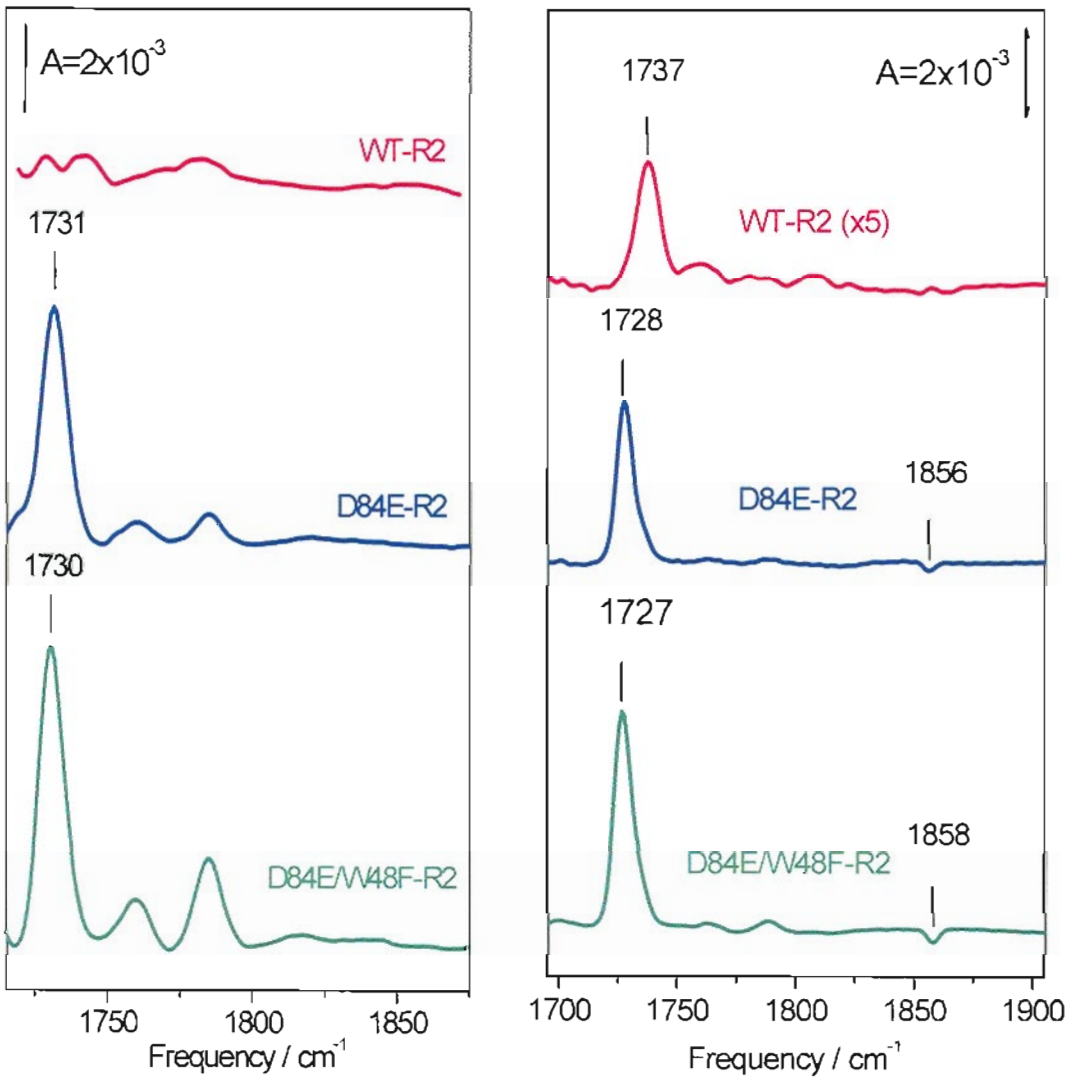

Fig. 3.7 FTIR spectra of nitrosyl complex of wt-R2, D84E-R2 and D84E/W48F-R2. In each experiment the protein concentration is 0.7mM and 3 equivalent of iron was added before exposure to NO.
- Left panel: The room temperature difference spectra are obtained using NO adducts minus buffer blanks.
- Right panel: The low temperature difference spectra are obtained by subtracting data collected before and after illumination. The wt-R2 difference spectrum was multiplied by a factor of 5 for comparison.

3.6 Spectroscopic Studies of a Cysteine-Based Nitrosyl Complex

As more Fe(II) is added, another two bands at 1761 and 1785 cm^{-1} are also observed in FTIR spectra (Fig. 3.8, left). Identical frequencies in the wt and variant proteins, and their ^{15}N-isotope dependence confirm their assignment to ν(N-O) modes. The bands at 1761 and 1785 cm^{-1} are assigned to the $[(Cys)_2$-Fe-$(NO)_2]$ cluster also observed earlier by EPR spectroscopy; this assignment is based on the following evidences: 1) these two bands are weak when 2 equivalent of iron is added to the apo-proteins but their intensity can be greatly increased as 4 equivalent of iron is added 2) while the ν(N-O) from the NO adducts at the diiron site are perturbed by the mutations studied here, the 1760 and 1785 cm^{-1} bands are identical in all three proteins 3) treatment of the iron-loaded protein with mercury prior to the addition of NO inhibits the formation of this nitrosyl species (Fig. 3.8, right), but has no effects on the NO adducts at the diiron active site. 4) The ν(N-O) doublet associated with the $[(Cys)_2Fe(NO)_2]$ cluster is not observed in light-induced difference spectra at 15K (Fig. 3.7), consistent with its lack of visible absorption feature in the $[(Cys)_2Fe(NO)_2]$ cluster. The assignment of cysteine-iron-nitrosyl complex is further confirmed by the observation of very similar ν(NO)s at 1764 and 1790 cm^{-1} in a self-assembling $[(Cys)_2$-Fe-$(NO)_2]$ cluster formed with a cysteine/iron/NO mixture (Fig. 3.9). The $(Cys)_2$-Fe-$(NO)_2$ species is also associated with an increase in UV-vis absorption at ~350 nm. The Fe-NO species in the active site, with a UV-vis absorption at ~450 nm, is not resonance enhanced with a 413-nm excitation, but this excitation enhances the RR spectra of the $[(Cys)_2$-Fe-$(NO)_2]$ cluster in R2 (Fig. 3.10, left) and in the self-assembling cysteine models (Fig. 3.10, right). The 645 cm^{-1} band which downshifts by 21 cm^{-1} with ^{15}NO is tentatively assigned to a $\nu_s(Fe(NO)_2)$.

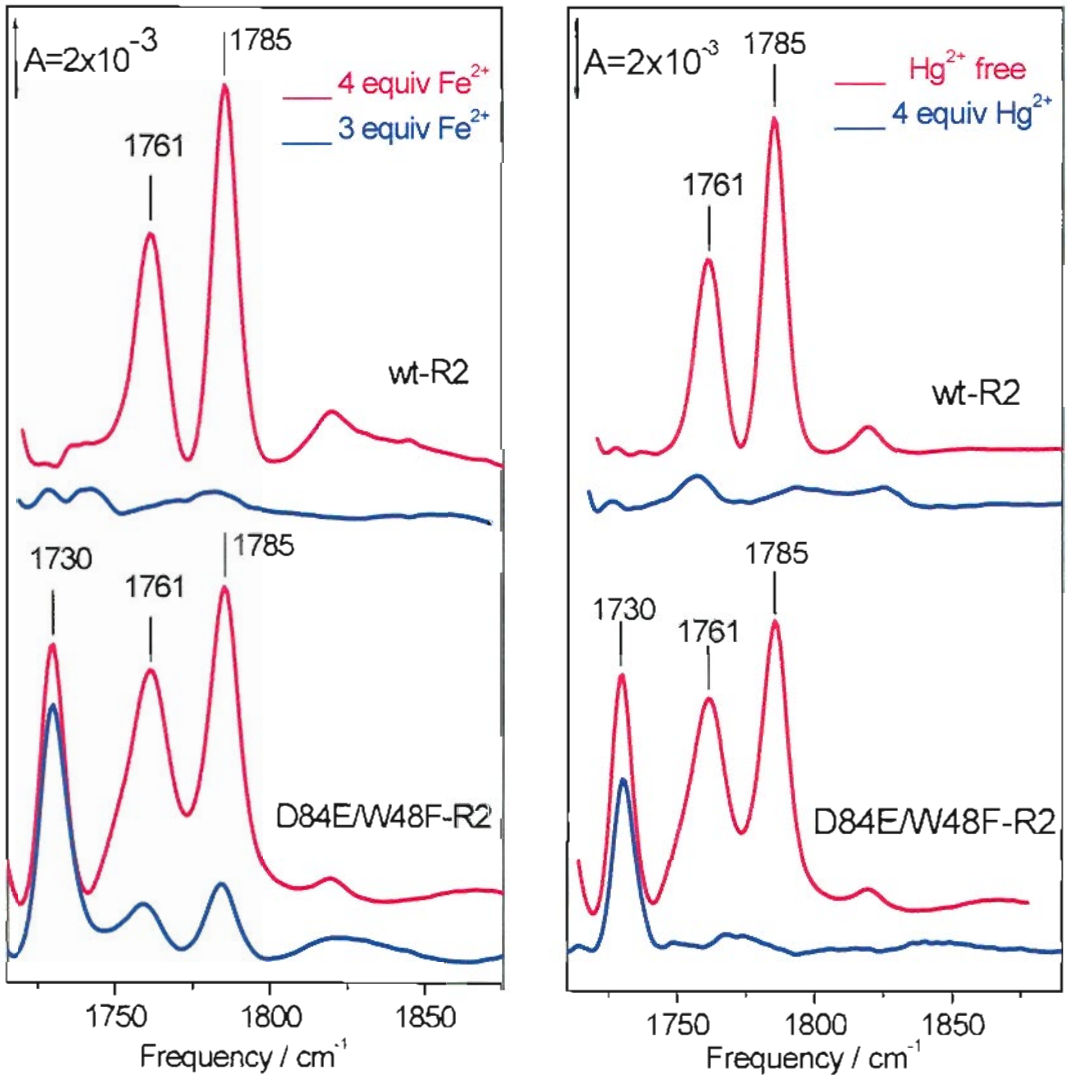

Fig 3.8 Room temperature FTIR spectra of R2-NO complex. The final protein concentrations of wt-R2 and W48F/D84E-R2 were 0.7 mM. The difference spectra are obtained using NO adducts minus buffer blanks.
- Left panel: untreated R2 with 3 equiv Fe(II) (blue) and 4 equiv Fe(II) (red)
- Right panel: untreated R2 with 4 equiv Fe(II) (red), and the R2-NO complex pre-treated with 4 equiv of $HgCl_2$ (blue).

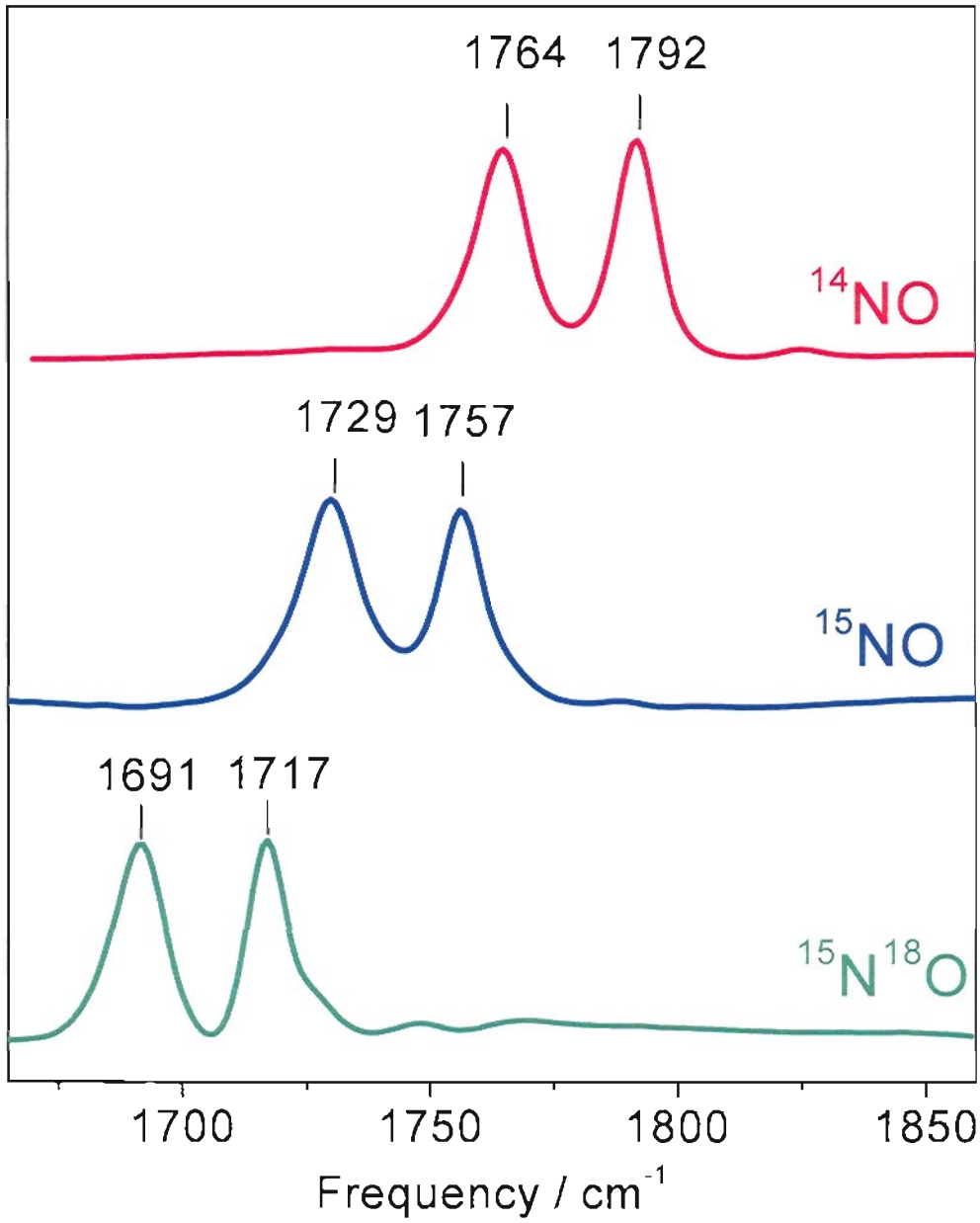

Fig. 3.9 Room temperature FTIR spectra of $(Cys)_2$-Fe-$(NO)_2$ model in D_2O (pD 7).

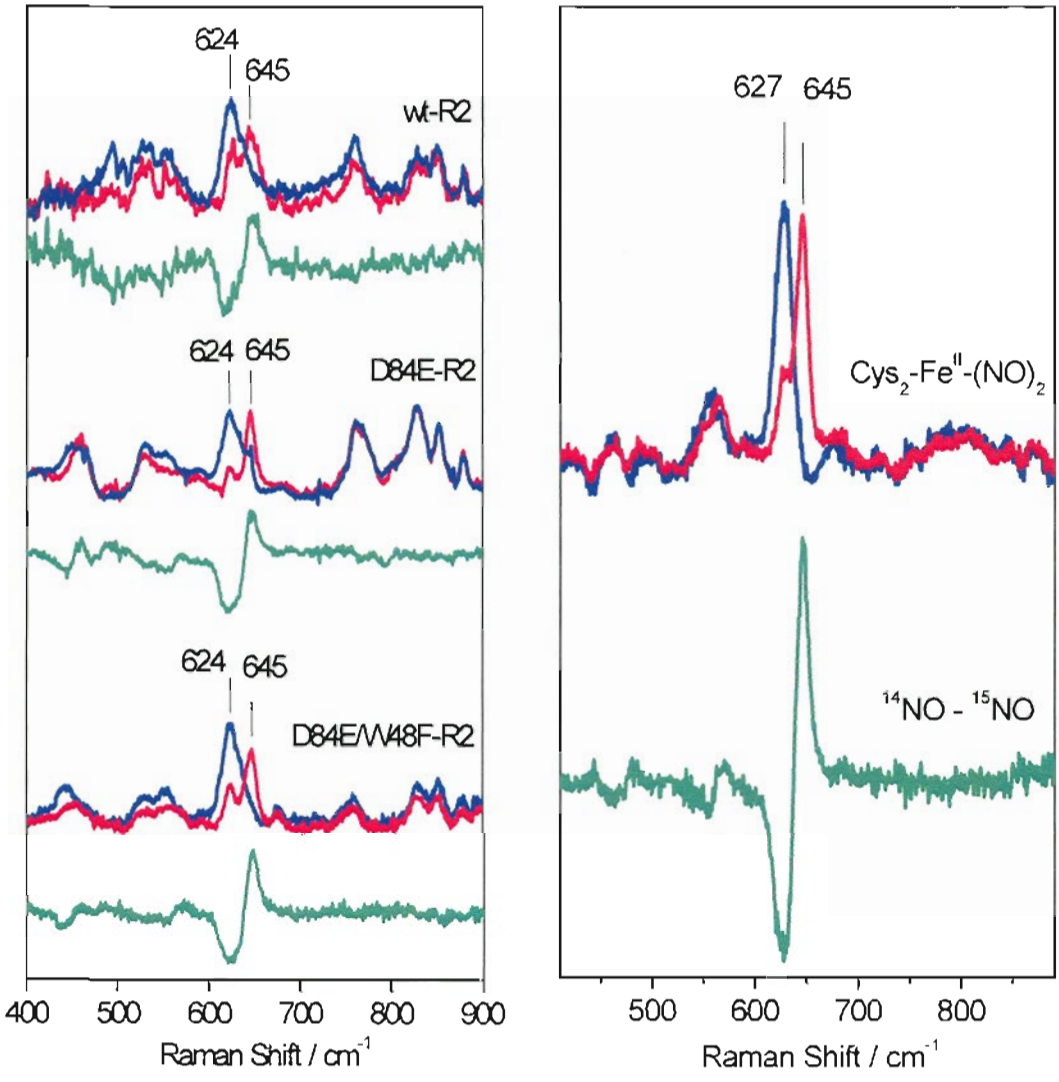

Fig. 3.10 Low-frequency RR spectra of R2-NO and $(Cys)_2$-Fe-$(NO)_2$ model. All RR spectra were obtained with a 413-nm excitation (10 mW) and continuous samples translation to minimize laser-induced NO-dissociation.
- Left panel: RR spectra of the ^{14}NO (red) and ^{15}NO (blue) complexes of wt-R2, D84E-R2, and D84E/W48F-R2. ^{14}NO minus ^{15}NO difference spectra are also shown (green).
- Right panel: Equivalent RR data obtained with the $(Cys)_2$-Fe-$(NO)_2$ model.

3.7 Discussion

We have characterized several nitrosyl complexes in wt and variant R2 proteins using vibrational spectroscopy. Our results show that, in all three proteins, the two [Fe-N-O] units that form within a diiron cluster are indistinguishable from their ν(Fe-NO), δ(Fe-N-O) and ν(N-O). The set of Fe-N-O vibrational frequencies observed in wt-R2 is changed only slightly by the D84E substitution, whereas the W48F substitution has no effect on these frequencies. From the observation of symmetrical binding of one NO to each iron in these diiron centers, we infer that the O_2 reactions of all three proteins are likely to proceed via a common symmetrically bridged peroxodiiron(III) complex.

Using a combination of spectroscopic techniques, we have shown that NO reacts with reduced R2 proteins to form three distinct iron-nitrosyl species. The major species is a $[\{FeNO\}^7]_2$ complex (> 80%) in which two irons bind one NO molecule each and are antiferromagnetically coupled. A second species is a mononuclear $\{FeNO\}^7$ complex (< 15%), which is expected to be located at the protein diiron site since the apo proteins can only be loaded with 3 equiv Fe(II) [Pierce et al., 2003]. Subtle variations in the $g \sim 4$ EPR signal of this complex in the wt and variant proteins are consistent with this conclusion. A third species (1-3%) is assigned to a $(Cys)_2Fe(NO)_2$ complex, which must involve surface exposed Cys side chains. The spectroscopic features that we assign to this species match those observed here with a self-assembling model complex. EPR signature for $R_2Fe(NO)_2$ species were observed previously in R2, MMOH, and ferritin [Drapier et al., 1991; Lee et al., 1994]. None of the proteins studied here showed evidence of a [Fe(II)-$\{FeNO\}^7$] complex, which is accompanied by a characteristic EPR signal at $g = 2.78$ as seen in the nitrosyl adduct of Hr. This quantitative information is extracted from the EPR data and is supported by the visible absorption and RR spectroscopic results.

Structure of the [(FeNO)$_2$] Cluster in Wt-R2 and Variant Proteins

Binding of one molecule of NO on each of the iron ions within the active site pocket was expected, but it is striking that both of these $\{FeNO\}^7$ species share the same vibrational signature. The possibility that one of the FeNO units might not contribute to the vibrational spectra was ruled out by varying the excitation wavelengths used in the RR experiments and by parallel FTIR experiments. The vibrational frequency modes of an [Fe-N-O] unit are expected to depend on its iron coordination (number and nature of the ligands, geometry, and chirality) as well as the microenvironment of the NO group (steric constraints, dielectric constant, hydrogen bonding interactions). Obviously, counterbalancing effects might allow two nonequivalent $\{FeNO\}^7$ species to share the same Fe-N-O vibrational signatures, but the most likely explanation is that the diiron sites in wt and variant R2 proteins stabilize two equivalent $\{FeNO\}^7$ species.

Our results indicate that the two iron nitrosyl units must share the same coordination number and geometry. Carboxylate ligands bring flexibility to the diiron site because they can adopt a wide variety of coordination geometries (i.e., monodentate or bidentate, terminal or bridging). Crystal structures of chemically reduced and photoreduced R2 proteins have revealed symmetric diiron sites with both irons four-coordinated [Nordlund et al., 1993b], whereas CD and MCD measurements predicted an asymmetric diiron(II) site with one iron pentacoordinated and the other tetracoordinated [Pulver et al., 1995]. Recent crystal structures of R2 proteins reconstituted by infusion of Fe(II) into apoprotein crystals support this asymmetric geometry [Voegtli et al., 2003]. While the addition of one NO ligand per iron site could produce one pentacoordinated and one hexacoordinated $\{FeNO\}^7$, carboxylate shifts could take place to produced two $\{FeNO\}^7$ with identical coordination number and nature, i.e. one imidazole and three carboxylate ligands. Such rearrangement is also likely to take place during the O_2 reaction with D84E-containing variant R2 proteins, given that the two Fe^{III} irons are equivalent in all the bridging peroxide

intermediates characterized so far [Bollinger et al., 1998; Baldwin et al., 2003]. The same argument can be made for the geometry and chirality of these nitrosyl and peroxo complexes.

The Fe-N-O vibrations observed in wt-R2 and variant proteins are comparable to those reported for the NO adduct of superoxide reductase [Clay et al., 2003], and the six coordinated iron-nitrosyl model complex [Fe(Me_3TACN)(NO)-(N_3)$_2$], where (Me_3TACN) is N,N',N"-trimethyl-1,4,7-triazacylononane (Table 2.2). As discussed earlier by Clay et al. [Clay et al., 2003], the isotope shifts reported for the ^{15}NO and $^{14}N^{18}O$ and the intensity of the RR band at 497 cm^{-1} in [Fe(Me_3TACN)(NO)-(N_3)$_2$] are consistent with its assignment to the ν(Fe-NO) mode rather than the δ(Fe-N-O). The lower ν(Fe-NO) observed in superoxide reductase is accompanied by a 32 cm^{-1} downshift of the ν(Fe-S_{Cys}), and was assigned to a trans effect where both ligands compete for the same π- and σ-bonding interactions with the Fe(II). Yet, lower ν(Fe-NO) are observed in the NO adducts of wt and variant R2 proteins where no such trans effect is expected to take place. These low frequencies are likely to reflect interactions of the nitrosyl group with its microenvironment. In Hr, where a low ν(Fe-NO) is also observed [Coufal et al., 1999], a hydrogen-bond interaction between the nitrosyl oxygen and the μ-hydroxy group that bridges the two irons is expected to decrease the electron donating character of the nitrosyl group toward the iron. Steric interactions might also prevent the nitrosyl ligands from adopting the optimal bent geometry which maximizes the electron donation from the NO π* to the Fe(II) d orbitals and result in a weakening of both Fe-NO and N-O bonds. Clearly, more work is needed to ascribe the variations in Fe-N-O frequencies to changes in specific structural features, but the similarities of the Fe-N-O vibrational signatures in the wt and variant R2 proteins already allows us to draw conclusions regarding their O_2 reactions.

Relevance to O_2 Reaction Intermediate in R2 Proteins

Exposure of wt-R2 and variant proteins to NO gas results in the formation of two identical $\{FeNO\}^7$ units within the diiron active site (Fig. 3.11). Notably, even when the formation of the $[\{FeNO\}^7]_2$ cluster is incomplete as in wt-R2, the binding of only one NO molecule to form an $[Fe(II)\text{-}\{FeNO\}^7]$ cluster is not observed, demonstrating cooperative binding of NO at the diiron site. With NO, which does not favor a μ-1,2 bridging configuration, NO binding to one iron favors the binding of another NO molecule at the second iron site. However with O_2, the binding of two O_2 molecules to form two equivalent iron-superoxo complexes within the diiron site is expected to be unfavorable, in terms of both entropy and enthalpy, and a single O_2 can bind in a bridging fashion. Thus, the behavior of wt-R2 toward NO suggests that its active site is designed to promote the binding of O_2 in a bridging configuration. The symmetry of the μ-1,2 peroxo intermediate observed in R2-W48F/D84E is preserved in the structure of the NO adducts with two indistinguishable $\{FeNO\}^7$ units, and the formation of a similar $[\{FeNO\}^7]_2$ cluster in wt-R2 supports the presence of a similar symmetric peroxodiiron(III) intermediate in the O_2 reaction of wt-R2.

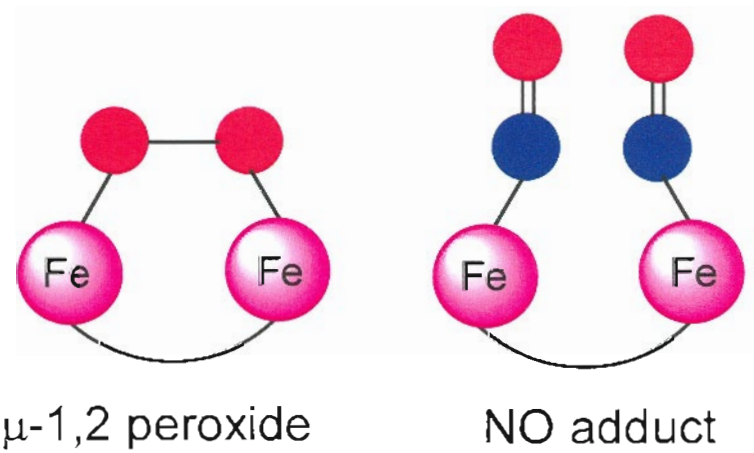

Fig. 3.11 Structure of the proposed peroxide and NO adducts in R2 proteins.

CHAPTER 4

THE AZIDO COMPLEX IN METHANE MONOOXYGENASE HYDROXYLASE AND ITS IMPLICATIONS FOR O_2 ACTIVATION*

4.1 Catalytic Cycle in MMOH

MMOH utilizes O_2 and a carboxylate-bridged diiron center to oxidize methane to methanol. The enzyme is an $\alpha_2\beta_2\gamma_2$ heterodimer and requires the presence of a 16-kDa regulatory protein, MMOB, to optimize the hydroxylase activity. In the presence of the regulatory protein MMOB, the reduced form of MMOH (H_{red}) binds and reductively activates dioxygen, proceeding through a putative superoxo species, and then forms a diiron(III) peroxide intermediate (H_{peroxo}), which evolves into a diiron(IV) dioxo species (Q), which in turn reacts with methane (Fig. 4.1). Q is the species that hydroxylates methane, leaving MMOH in the resting diiron(III) form called H_{ox} [Liu et al., 1995c].

---

* Material in this chapter has been published in this or similar form in *J. Am. Chem. Soc.* and is used here with permission of the American Chemical Society.

Lu, S., Sazinsky, M. H., Whittaker, J. W., Lippard, S. J., and Moënne-Loccoz, P. (2005) Fourier Transform Infrared Characterization of the Azido Complex of Methane Monooxygenase Hydroxylase from *Methylococcus capsulatus* (Bath). *J. Am. Chem. Soc.* **127**, 4148-4149.

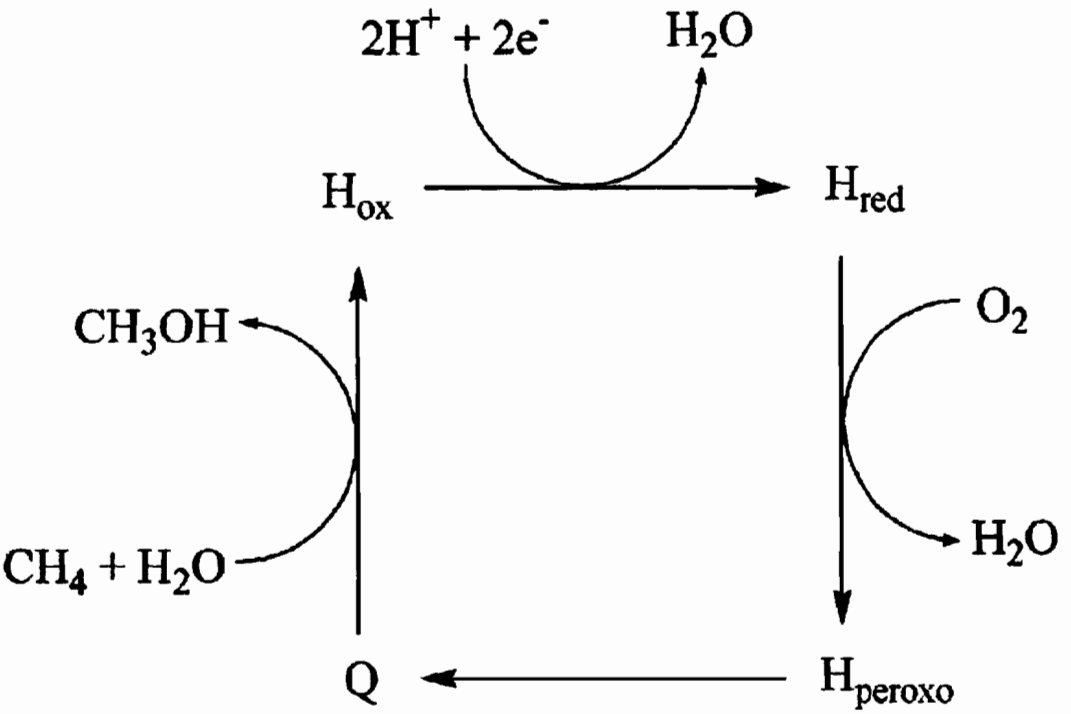

Fig. 4.1 The catalytic cycle of MMOH.

Originally published as Fig. 1 in:

Gherman, B. F., Baik, M. H., Lippard, S. J., and Friesner, R. A. (2004) Dioxygen activation in methane monooxygenase: A theoretical study. *J. Am. Chem. Soc.* **126**, 2978-2990.

4.2 Peroxo Intermediate of MMOH

H_{peroxo} is the first spectroscopically observable intermediate that occurs after mixing of H_{red}/2MMOB with dioxygen, and presents characteristic Mössbauer and optical spectroscopic features [Liu et al., 1994; Liu et al., 1995b; Lee and Lipscomb, 1999; Dunietz et al., 2000; Wallar and Lipscomb, 2001]. On the basis of DFT calculations, binding of O_2 at the dinuclear iron center of MMOH occurs with dissociation of a coordinated water molecule. The release of one water molecule into solution provides a significant gain in entropy, and the thermodynamics of formation of H_{peroxo} are predicted to be downhill with both iron atoms in a high spin configuration. [Dunietz et al., 2000]. However, this process is poorly understood at present and many conflicting observations have been made. For example, the formation of H_{peroxo} was reported to be pH independent [Liu et al., 1995a], whereas a different study found a sharp decrease in the H_{peroxo} formation rate with increasing pH [Lee and Lipscomb, 1999]. A symmetric diiron(III) H_{peroxo} with a nonplanar μ-η^2:η^2-O_2^{2-} binding mode is energy favored by DFT calculation (Fig. 4.2), and the homolytic cleavage of the O-O bond of H_{peroxo} yields the catalytically competent intermediate Q, which has a di(μ-oxo)diiron(IV) core [Gherman et al., 2004]. Lipscomb and coworkers have studied the effects of solvent pH and deuteration on the transient kinetics of H_{peroxo} and support a catalytic model with a heterolytic cleavage of an asymmetrical H_{peroxo} [Lee and Lipscomb, 1999].

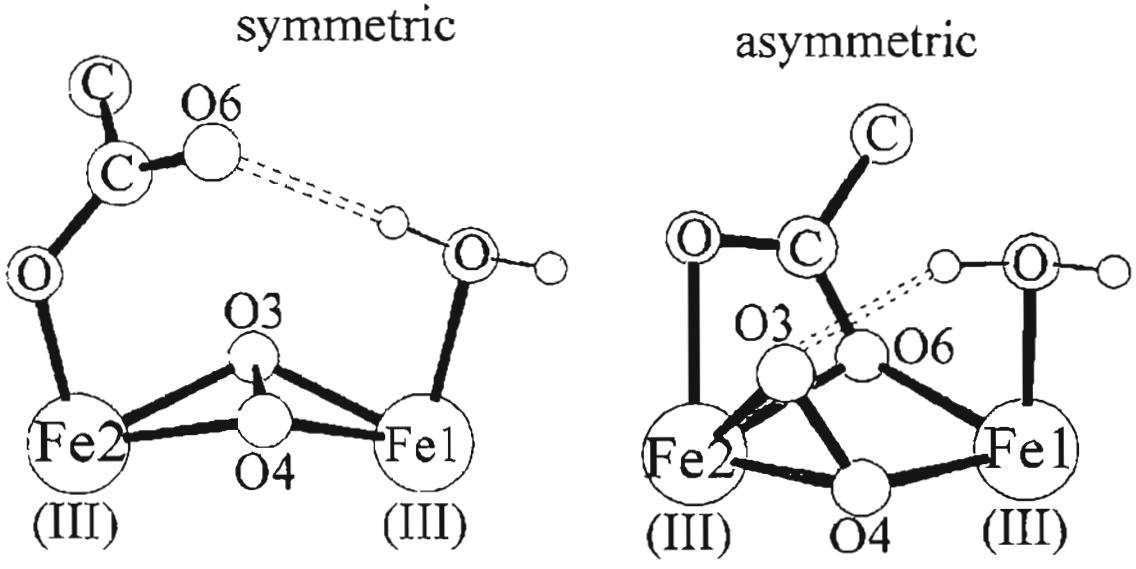

Fig. 4.2 Possible geometries for H_{peroxo} based on DFT calculations [Gherman et al., 2004]. Dashed lines represent hydrogen bonds.

Originally published as Fig. 6 in:

Gherman, B. F., Baik, M. H., Lippard, S. J., and Friesner, R. A. (2004) Dioxygen activation in methane monooxygenase: A theoretical study. *J. Am. Chem. Soc.* **126**, 2978-2990.

4.3 Azido Complexes in Diiron Proteins

A complementary approach to elucidate the structure of the peroxo diiron(III) intermediate is through the spectroscopic characterization of the analogous azido diiron(III) complexes. Because the highest occupied non-bonding π^* orbitals of azide are homologous to the filled π^* orbitals of peroxide, azido complexes can provide important structural details regarding the transient peroxo species. Azido complexes of ferric proteins are well-suited for vibrational characterization, because they exhibit a broad azide-to-iron(III) LMCT band at ~440 to 450 nm with an extinction coefficient of ~3,000 $M^{-1}\cdot cm^{-1}$. The $\nu_{as}(N_3)$ mode can be observable by RR or FTIR spectroscopy, and the impact of the asymmetric isotope labeling in $^{15}NN_2$ has been shown to correlate with the coordination geometry of the azide group [Pate et al., 1989]. Free azide in solution favors a [$^-$N=N$^+$=N$^-$] resonance form and exhibits a $\nu_{as}(N_3)$ vibration at 2056 cm^{-1} that shifts, as a single component, to 2039 cm^{-1} with $^{15}NN_2$. However, when the azide is coordinated to iron(III), the contribution of the resonance form [Fe^{3+}–N^{2-}–N$^+$≡N], relative to [Fe^{3+}–N$^-$=N$^+$=N$^-$], increases, and the $\nu_{as}(^{15}NN_2)$ splits into two components. In diiron systems, the greatest splitting is expected when the azide group adopts a μ-1,1 bridging geometry, while a η^1-terminal geometry produces a smaller splitting, and a symmetric μ-1,3 bridging geometry results in no splitting (Fig. 4.3).

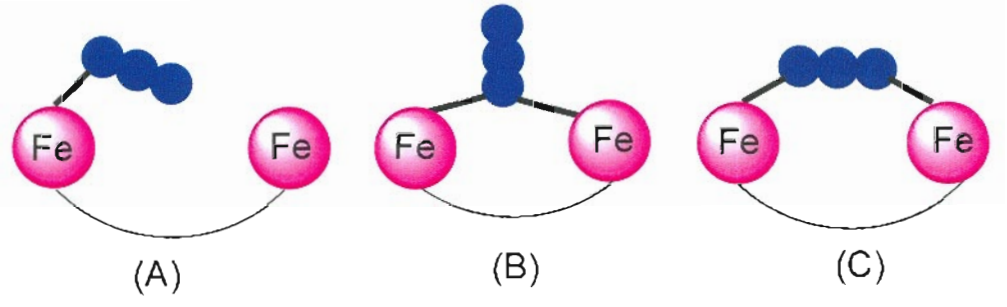

Fig. 4.3 Possible binding geometries of azide to diiron centers: terminal-η^1 (A), bridging μ-1,1 (B), and bridging μ-1,3 (C).

A RR study of the Δ^9D-azido complex exemplifies the sensitivity of the azide ligand to the geometrical variability of diiron clusters [Ai et al., 1997]. At pH 6.2, a dominant $\nu_{as}(N_3)$ mode was observed at 2100 cm^{-1} and was assigned to a μ-1,3 bridging geometry due to its lack of splitting with $^{15}NN_2$. In contrast, at high pH, the spectrum shows a $\nu_{as}(N_3)$ at 2073 cm^{-1} that splits by 12 cm^{-1} with $^{15}NN_2$, indicating a η^1-terminal complex. This pH dependence, with $pK_a \sim 8$, was proposed to reflect the protonation of a hydroxo bridge in the η^1-terminal azido complex. Thus, in addition to providing valuable information about the coordination geometry of peroxo diiron species, the azido group is also a good reporter of protonation events at the active site.

In an effort to advance the structural characterization of MMOH, we used FTIR spectroscopy and took advantage of the photolabile character of iron-azido complexes. Specifically, "dark" minus "illuminated" FTIR difference spectra at cryogenic temperatures allow us to extract the $\nu_{as}(N_3)$ vibrations from metal bond azido group from all other background signals. The extracted frequency and its isotope sensitivity, in turn, provide valuable information about the azido-metal coordination and hydrogen bond interactions within the active site pocket. We used an analogous approach when studying iron nitrosyl complexes in R2 [Lu et al., 2004b], which was described in chapter 3. To demonstrate the feasibility of this approach, we used the well characterized azido complex of the iron-containing superoxide dismutase (FeSOD) of *E. coli* [Lah et al., 1995; Xie et al., 2002; Tierney, et al., 1995], and used the same experimental conditions with the azido complex of MMOH.

4.4 Materials and Methods

The azido complex of FeSOD was prepared at room temperature using a 1.5 mM enzyme concentration (3 mM in monomer) in 50 mM phosphate pH 7.0 and 10 mM sodium azide. UV-vis spectra were recorded directly on the FTIR cell before and after the FTIR experiments. The extent of azido complex formation was estimated to be 35% by comparing the UV-vis absorption increase at 430 nm with that observed in

saturating conditions (i.e., 100 mM azide). In the MMOH experiments, the enzyme concentration was ~1 mM in 25 mM MOPS pH 7.0 and 50 mM azide. Comparison of the UV-vis absorption change with that observed in saturating conditions (500 mM) suggests that ~60% of azido complex was formed for FTIR sample.

For each experiment, an 11-μL droplet of the azido complex was sandwiched between two CaF_2 windows with a 15-μm Teflon spacer. A Cary 50 spectrometer was used to obtain a UV-vis spectrum of the sample in the FTIR cell before mounting it to a closed-cycle cryogenic system (Displex, Advanced Research Systems). The cryostat was installed in the FTIR sample compartment and kept in the dark while the temperature dropped to 15 K. The temperature of the sample was monitored and controlled with a Cry-Con 32 unit. Series of FTIR spectra of 1000-scan accumulation were collected with a 4 cm^{-1} resolution using a Perkin-Elmer system 2000 equipped with a liquid-N_2 cooled MCT detector. Photolysis was induced by continuous illumination of the sample in the FTIR sample chamber using a 50 W tungsten lamp after filtering out heat and NIR emission. The amplitude of the "dark" – "illuminated" FTIR difference spectra was observed to reach a plateau after illumination period ranging from 15-20 min, and subsequent illumination did not produce further changes.

4.5 Spectroscopic Studies of FeSOD-N_3

Before we characterize the azido complex with diiron enzyme of MMOH, we first present FTIR data obtained on the structurally well-characterized terminal azido complex of FeSOD. The iron center in FeSOD has a trigonal-bipyramidal geometry with three histidines, one aspartate, and one axial solvent molecule engaged in a hydrogen bond network to which the carboxylate of D156 also participates (Fig. 4.4). The coordinated solvent molecule has been implicated in the coupling of proton and electron transfer, cycling between hydroxo-iron(III) and aqua-iron(II) [Lah et al., 1995]. The geometry of the oxidized form presents an open coordination site that can

be occupied by azide at neutral pH and by a second hydroxide at pH > 7 [Tierney et al., 1995].

From previous RR spectroscopy, the ν_{as}(NNN) mode is observed at 2057 cm^{-1}. When the complex is formed with $^{15}NN_2$, ν_{as}(NNN) splits into two components at 2039 and 2051 cm^{-1} [Xie et al., 2002]. Accordingly, the FTIR difference spectrum "dark" minus "illuminated" shows these same frequencies (± 1 cm^{-1}) as positive bands, associated with negative bands at 2025 and 2014 cm^{-1} assigned to the dissociated $^{14}N_3^-$ and $^{15}NN_2^-$, respectively (Fig. 4.5). The percentage of photolyzed population which could be trapped at 15 K was deduced from curve fitting analysis. For FeSOD-N_3, when the concentration of free azide is comparable with enzyme concentration, the dark spectrum can be fitted with two Gaussian curves: one at 2045 cm^{-1} (free azide) and one at 2056 cm^{-1} that corresponds to the iron-azido complex. The positive signal in the "dark" minus "illuminated" spectrum represents 17 ± 5% of the signal observed at 2056 cm^{-1}. For such enzyme as MMOH, which has a relative lower azide binding affinity, the contribution of free azide is so large that the total concentration of azido complex formed cannot be determined from the dark FTIR spectrum at 15 K. Using the UV-vis absorption at room temperature and assuming no severe change in binding affinity as the temperature is lower to 15 K, the photolysis is estimated at 15 ± 10%. In contrast, hemoprotein-carbonyl complexes readily reached 100% photolysis under the same experimental conditions. The lower photolysis yield of the azido complexes, however, is not unexpected because the larger size of N_3^- compare to CO and the electrostatic attraction between the photolyzed azide anion and iron(III) are expect to promote geminate rebinding at 15 K. Moreover, different side-chain configurations sampled by the protein dynamics and trapped at 15 K produce a distribution of protein conformers, of which only a fraction present a migration route for the dissociated ligand.

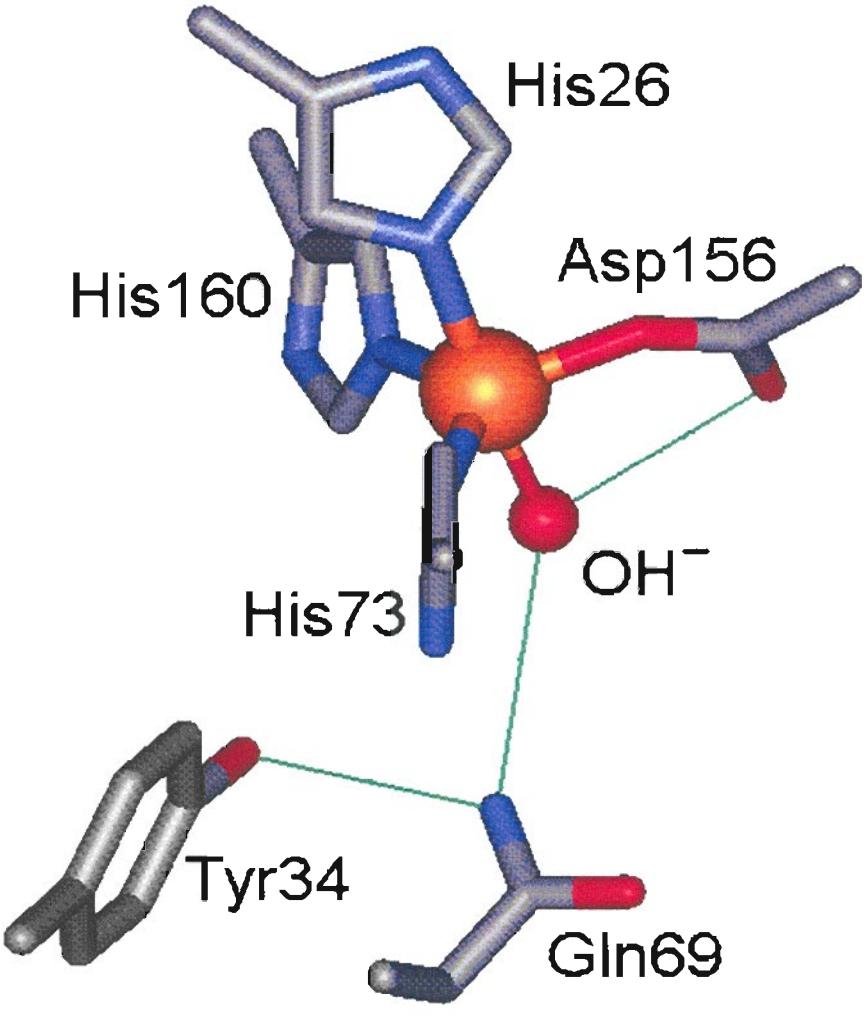

Fig 4.4 Iron site structure of oxidized FeSOD from *E. coli* (PDB accession code: 1ISB)

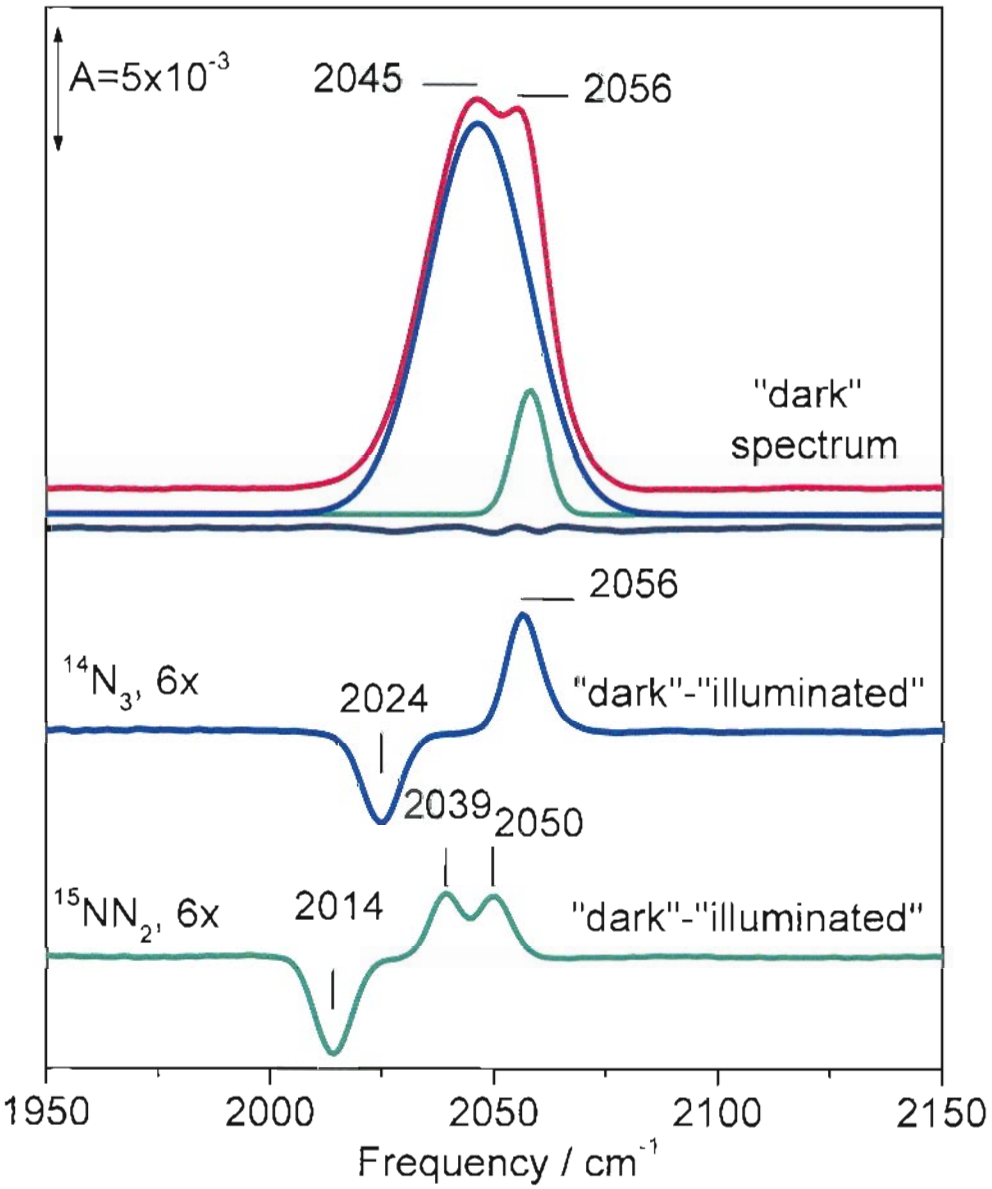

Fig. 4.5 FTIR spectra of FeSOD-N_3 obtained at 15 K. The top trace (red) is a "dark" spectrum of FeSOD-N_3 showing the iron bound azide (2056 cm^{-1}) and excess azide in solution (2045 cm^{-1}). The overlapping curve fit (black dotted line), is obtained with two Gaussian components (green and blue solid lines). The residual from the fit is also shown (black). The middle and lower traces correspond to the "dark" minus "illuminated" FTIR difference spectrum obtained with the sample by adduct of $^{14}N_3$(blue) and $^{15}NN_2$ (green), and both of them are multiplied by 6. The iron bound azide corresponds to the positive peak, and photodissociated azide in nearby pocket corresponds to the negative peak.

4.6 Spectroscopic Studies of MMOH-N_3

Incubation of MMOH in 500 mM sodium azide results in the appearance of a ~440 nm absorbance band in the UV-vis spectrum, which may be readily assigned to an azide-to-iron(III) LMCT band (Fig. 4.6). Several lines of evidence indicate that this absorption spectrum corresponds to an enzyme-bound complex. When the complex formed in 500 mM azide is concentrated by ultrafiltration (Centricon 50, Amicon), the retentate exhibits the expected absorption increase, whereas the eluate shows no absorption from free ferric azide. RR spectra of MMOH-N_3 are obtained with 458-nm excitation within the azide-to-iron(III) charge transfer band. A broad band at ~370 cm^{-1} in the spectrum of the azide complex but absent in the spectrum of $MMOH_{ox}$ is identified as a ν_{as}(Fe-N_3) from its 4-cm^{-1} downshift with $^{15}NN_2$ (Fig. 4.7). Attempts at detecting the ν_{as} (NNN) mode using RR spectroscopy were unsuccessful due to a significant fluorescent background in the high frequency range of the RR spectra.

The ν_{as} (NNN) of MMOH-N_3 were extracted from low temperature FTIR spectra in "dark" minus "illuminated" difference spectra. The ν_{as} (NNN) occurs at 2077 cm^{-1} and spits into two bands at 2059 and 2073 cm^{-1} with $^{15}NN_2$ (Fig. 4.8A and 4.8B). The ν_{as}(NNN) band is 21 cm^{-1} higher than in FeSOD-N_3 and 5 cm^{-1} higher than the η^1-terminal azido complex formed in Δ^9D. The 14 cm^{-1} splitting of ν_{as} (NNN) with $^{15}NN_2$ is comparable to that observed in the FeSOD-N_3 and the pH 7.8 form of Δ^9D-N_3. This splitting is consistent with a η^1-terminal binding of azide to the diiron(III) cluster in MMOH, as μ-1,1 or μ-1,3 bridging geometries are expected to give rise to greater and smaller splittings, respectively. The vibrational data define an azide binding that favors the [Fe^{3+}–N^{2-}–N^{+}≡N] resonance form relative to the symmetric [Fe^{3+}–N^{-} =N^{+}=N^{-}] one. Incubation of the MMOH-azide complex in D_2O results in a 6 cm^{-1} downshift of the ν_{as}(NNN) and suggests that the azido group is engaged in hydrogen bond interaction(s) at the diiron site (Fig. 4.8C). Such a hydrogen bonding interaction at the 1N atom of the azido group is expected to increase the asymmetry of the two N-N bonds and to upshift ν_{as}(NNN).

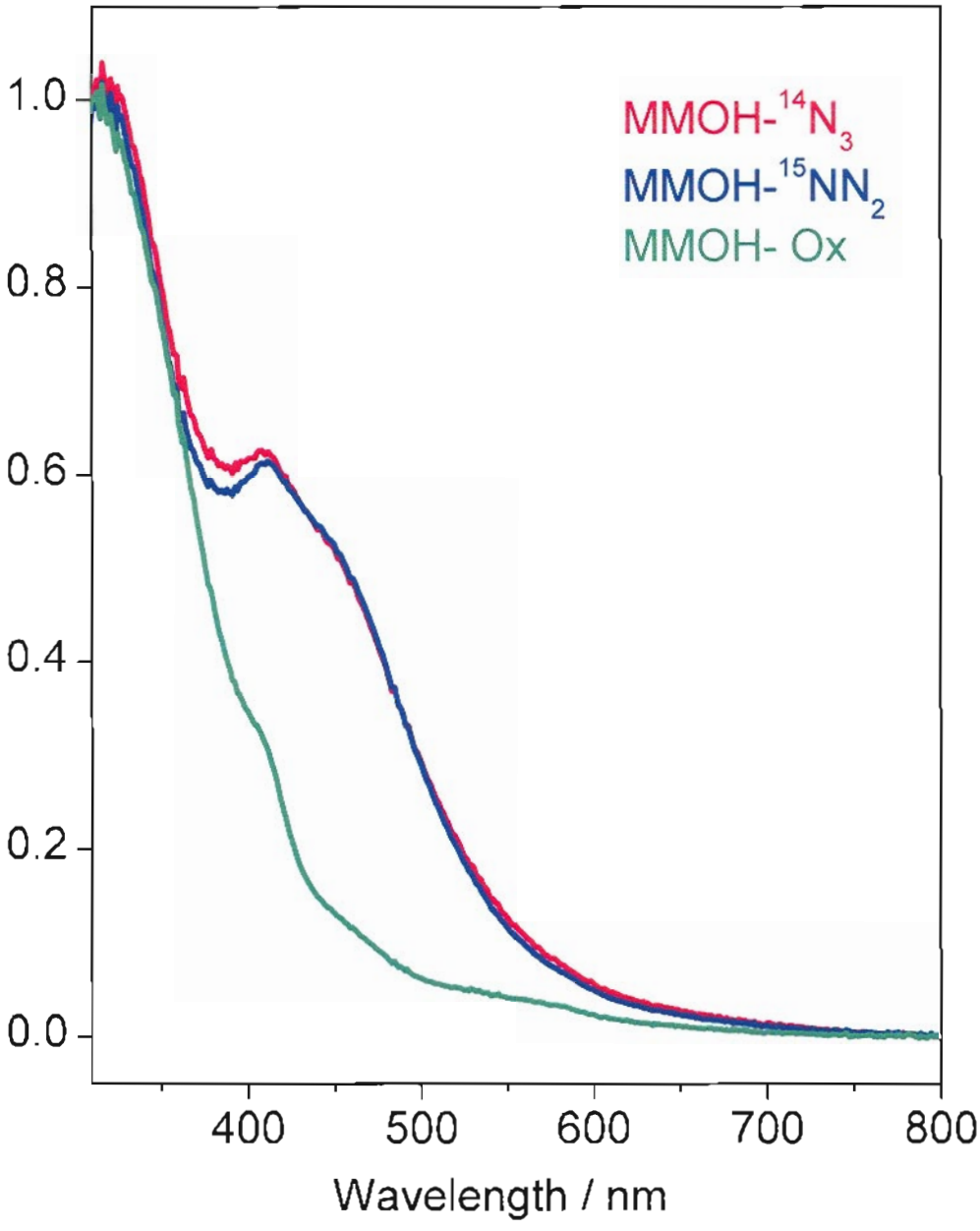

Fig 4.6 Room temperature UV-vis absorption spectra of MMOH-$^{14}N_3$ (red), MMOH-$^{15}NN_2$ (blue), and oxidized MMOH (green) obtained directly from RR sample in capillary (0.1 cm pathlength).

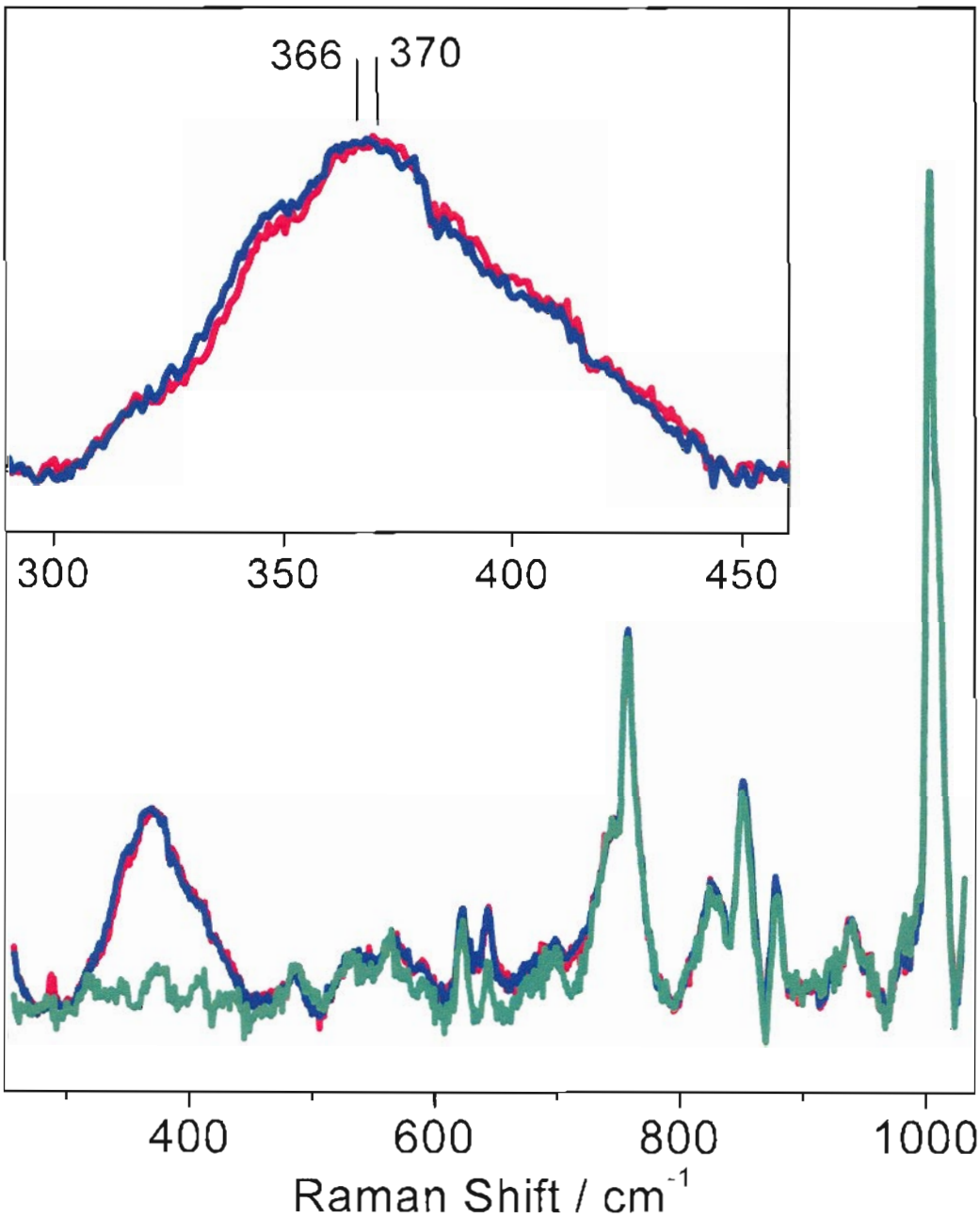

Fig. 4.7 Room temperature RR spectra of oxidized MMOH (green), MMOH-N_3 (red) and MMOH-$^{15}N^{14}N_2$ (blue). RR spectra were obtained with 458-nm excitation.

Deuterium exchange at the hydrogen bond donor will diminish the strength of the hydrogen bond and result in a downshift of the ν_{as}(NNN). The terminal water molecule bound to Fe1 in all MMOH crystal structures is a likely source of the H-bond donor.

The FTIR difference spectra of the $^{14}N_3$ and the $^{15}N^{14}N_2$ complexes of MMOH also display negative signals at 2136 cm^{-1} (Fig. 4.8A) and at 2114 and 2132 cm^{-1} (Fig. 4.8B), respectively. These frequencies are 6 cm^{-1} higher than ν_{as}(NNN) from hydrazoic acid in aqueous solution [Moore and Rosengren, 1966]. As in deuterated hydrazoic acid, Fermi resonance splitting of the ν_{as}(NNN) is observed with deuterated samples (Fig. 4.8C). Thus, the photodissociation of the iron-azido complex in MMOH is accompanied by a proton transfer that results in the formation of an N_3H molecule that remains trapped within the substrate pocket.

A comparison of the signal intensities in the FTIR difference spectra of MMOH-N_3 and FeSOD-N_3 suggests that, like in FeSOD-N_3, 17% of photolyzed azide is trapped at 15 K in MMOH. While rebinding starts to occur at 50 K in FeSOD, the temperature must be raised above 200 K to observe the rebinding of azide to MMOH. This observation suggests a higher energy barrier, which must include the reorganization energy associated with the proton transfer associated with the photolysis in MMOH. The FTIR experiments on MMOH-N_3 were reproduced with 2 and 4 equiv of MMOB, but the presence of this regulatory protein had no effect on the results described above (Fig. 4.9). Perturbation upon addition of MMOB might have been anticipated, since MMOB is believed to dock at the hydrophobic cleft of the $\alpha_2\beta_2\gamma_2$ dimer interface of MMOH and strongly influences the O_2-reactions of the diiron cluster [Walters et al., 1999].

Previous studies on azido-Δ^9D complex showed that the contribution of alternative terminal η-1 and bridging μ-1,3 geometries of azido iron complex could be affected by pH [Ai et al., 1997]. However, with varying the pH from 6.0 to 8.5 had no significant effect on the vibrational signature of MMOH-N_3 (Fig 4.10).

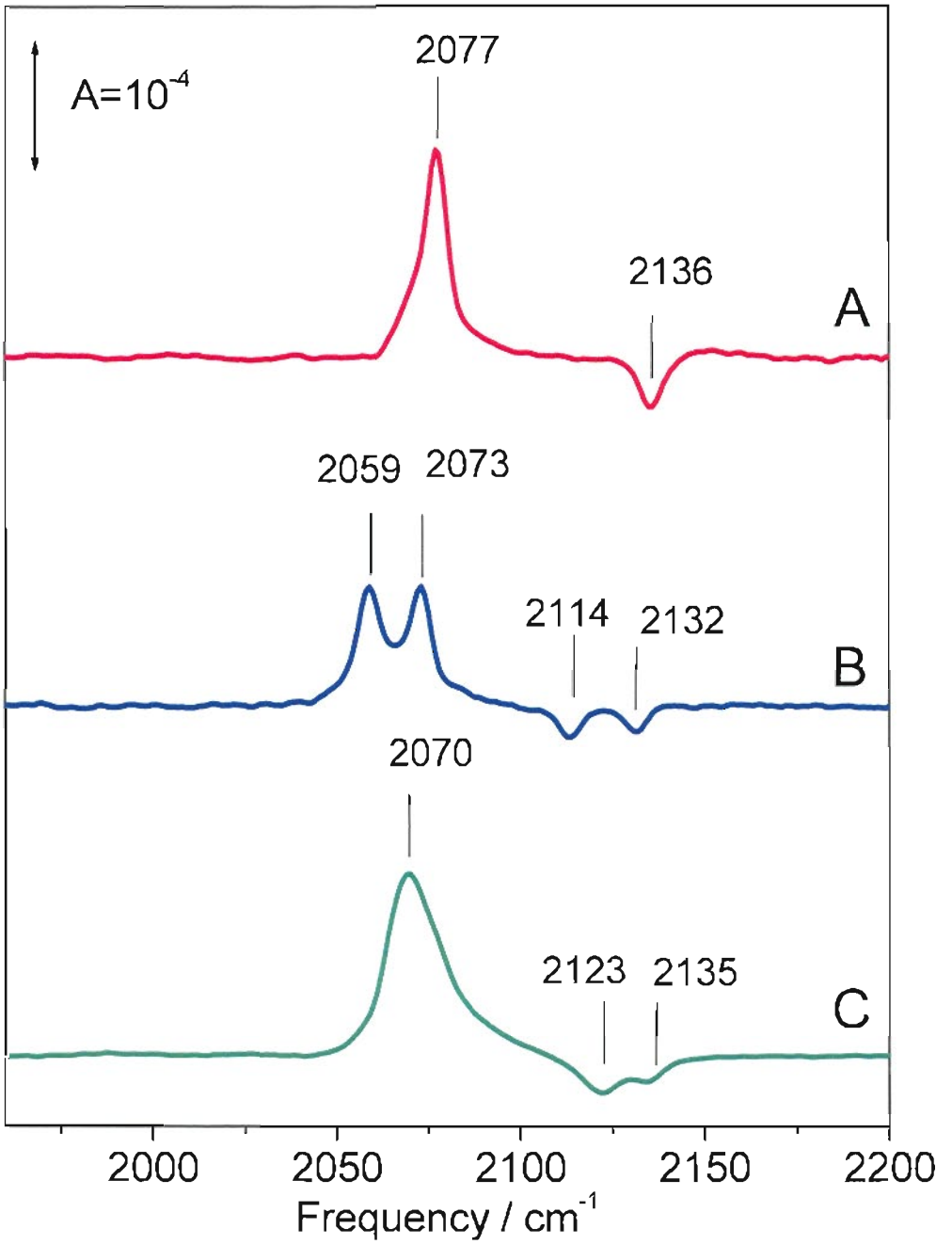

Fig. 4.8 FTIR difference spectra ("dark" minus "illuminated") of the azido complexes in MMOH at 15 K. MMOH-$^{14}N_3$ complex (A), MMOH-$^{15}N^{14}N_2$ complex (B), and MMOH-$^{14}N_3$ complex in D_2O (C). The enzyme concentration of MMOH was 1 mM, and the total azide concentration was 50 mM.

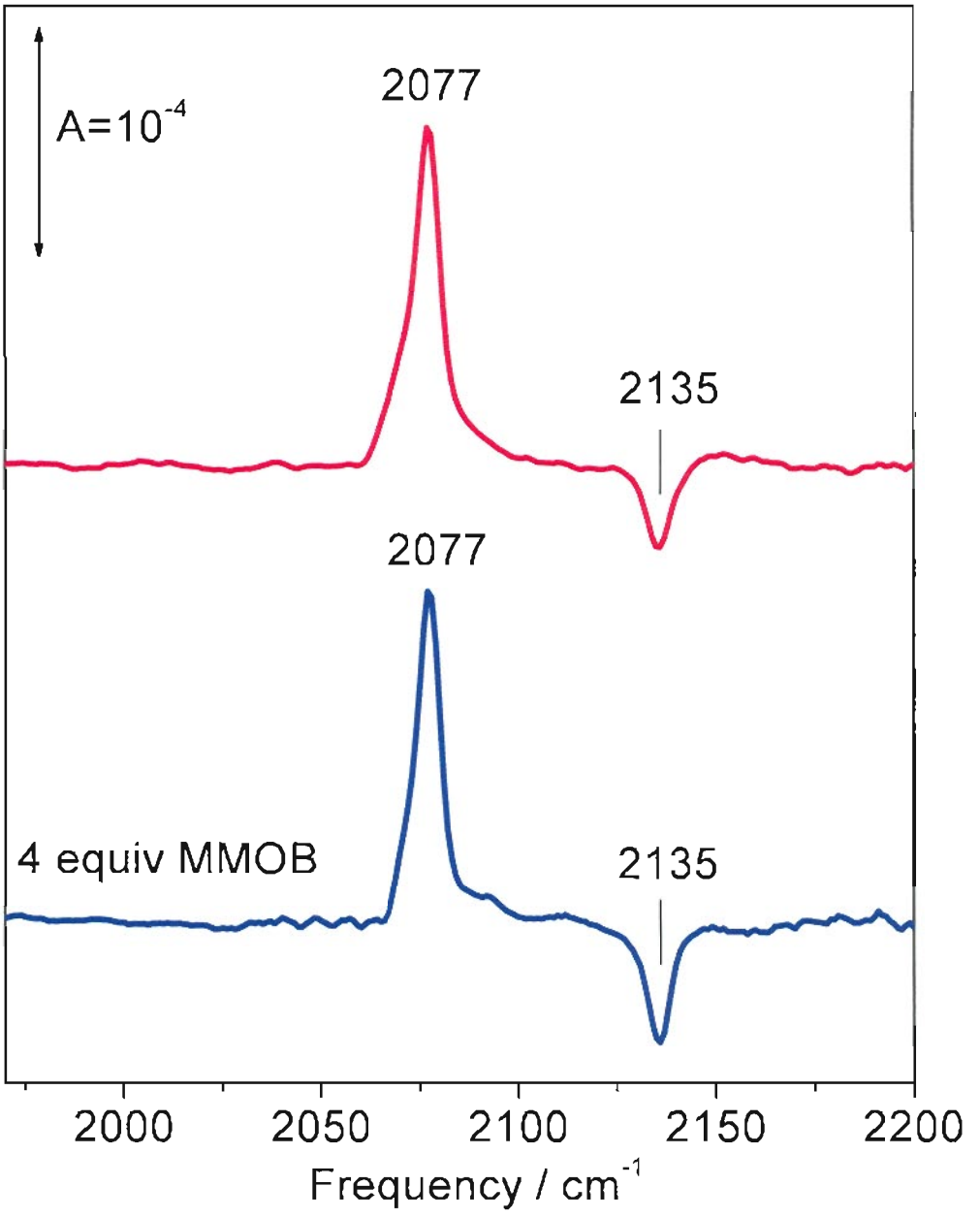

Fig. 4.9 FTIR spectra of MMOH-N_3 in absence of MMOB (red), and with 4 equiv MMOB present (blue).

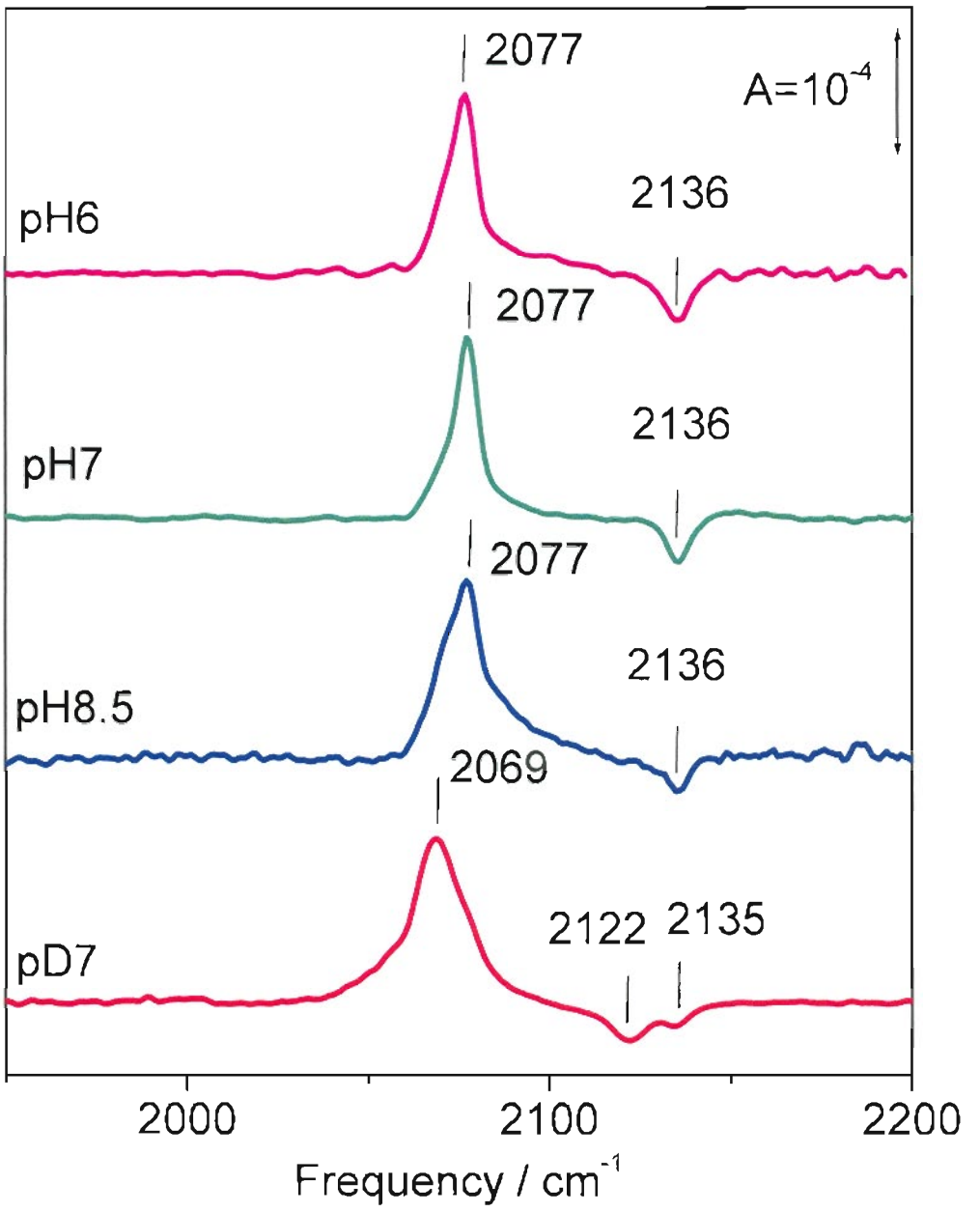

Fig. 4.10 Low temperature FTIR difference spectra ("dark" minus "illuminated") of MMOH-N_3 in pH 6 (A), pH 7 (B), pH 8.5 (C), and in D_2O (D). The enzyme concentration of MMOH is 1 mM, and the total azide concentration was 50 mM.

4.7 Discussion

The vibrational signature of MMOH-N_3 indicates that the azide is bound terminally to one iron(III) atom and that the azide-N1 atom is engaged in a hydrogen bonding interaction (Fig. 4.11). An aqua ligand would constitute a good candidate for a hydrogen bond donor to the azido complex and could also act as a proton donor during the photolysis process. This proton transfer from the aqua ligand to the leaving azide group would allow the photolysis to occur without a change in the overall charge of the diiron cluster. It also suggests an azide binding that differs significantly from what was recently observed in a crystal structure of the azido complex of toluene/*o*-xylene monooxygenase [Sazinsky et al., 2004]. In this related diiron enzyme, the azido group is bound asymmetrically in a μ-1,1 semi-bridging geometry and engages a hydrogen bond interaction at its N3 atom.

The azide binding geometry has mechanistic significance to the O_2 activation in MMOH. Two geometries of peroxo binding in diiron centers have been proposed based on DFT calculations (Fig. 4.11). The η^1-terminal binding of azide to the diiron(III) cluster supports an asymmetric binding geometry for the peroxo intermediate, and the hydrogen bond interaction we proposed between the azide-1N atom and aqua ligand fits the hydrogen bond interaction between the peroxide group and the aqua ligand of Fe1 proposed in the calculated structure. In the DFT calculations, the hydrogen bond interactions engaged by this aqua ligand play a critical role in the energetics of the superoxo and peroxo complexes [Gherman et al., 2004]. The light-induced proton transfer we have observed at 15 K between the azido group and his hydrogen-bond partner suggests that cleavage of the O-O bond in the peroxo intermediate might be associated with a proton transfer and a structure of Q distinct form the di-μ-oxo cluster often proposed in the literature (Fig. 4.11).

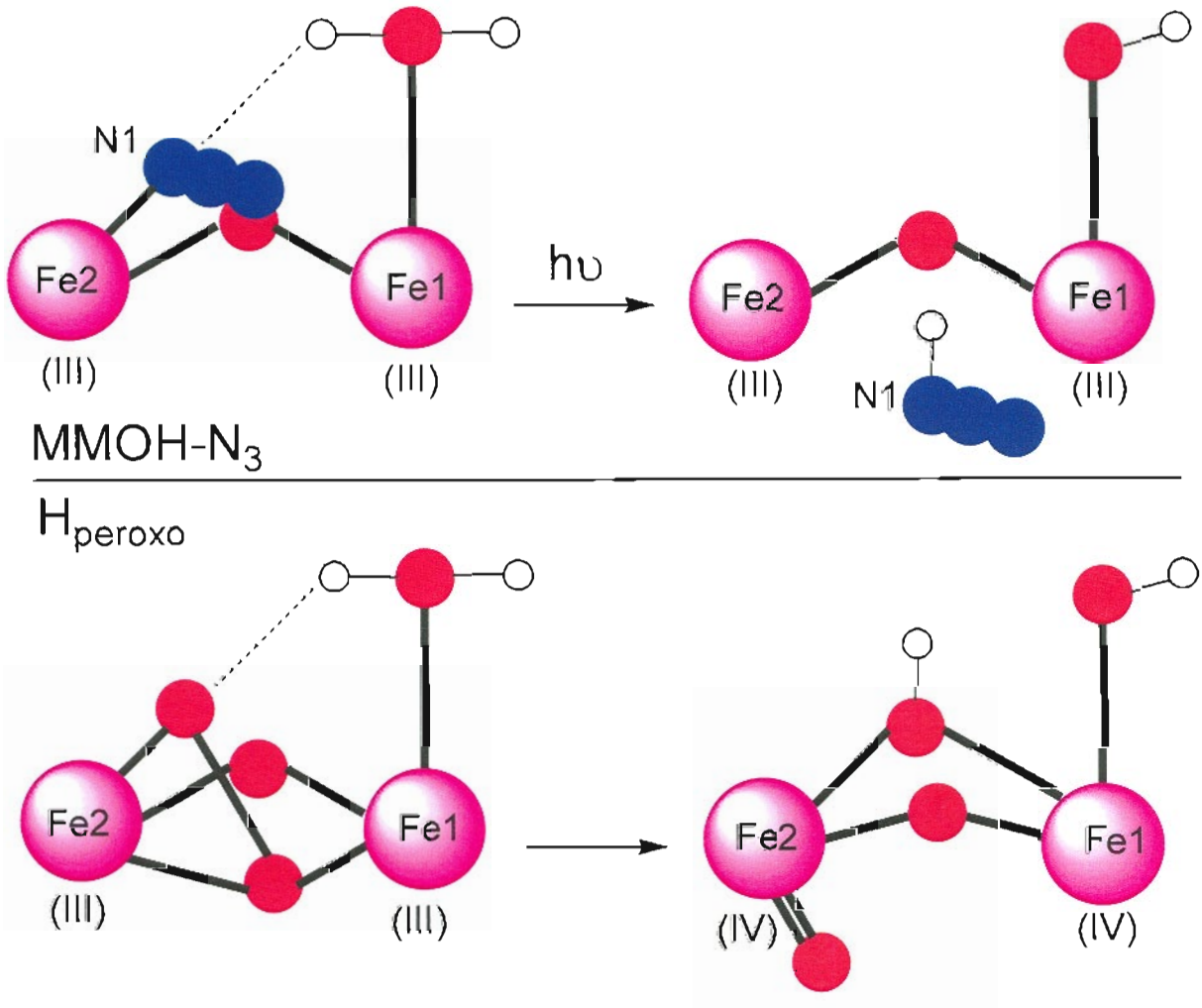

Fig. 4.11 Structure comparison of azido adduct of MMOH with H_{peroxo}. The photolysis of the azido complex and the decay of the peroxo intermediate are proposed to be coupled with a proton transfer.

CHAPTER 5

CARBONYL COMPLEXES IN NO REDUCTASES AND THEIR IMPLICATIONS FOR NO ACTIVATION*

5.1 Denitrifying NO reductases

Denitrification represents an alternative to oxygen respiration and utilizes a series of enzymes to convert nitrate to nitrogen gas, with nitrite, nitric oxide, and nitrous oxide as obligatory intermediate products (Equation 5.1) [Zumft, 1997; Castresana et al., 1994; de Vries and Schroder, 2002].

$$NO_3^- \rightarrow NO_2^- \rightarrow NO \rightarrow N_2O \rightarrow N_2 \quad \text{(Eq. 5.1)}$$

The reduction of NO to N_2O is catalyzed by a heme/non-heme diiron clusters anchored at the core of an integral membrane protein complex [Wasser et al., 2002]. This reaction is key to the denitrification process since it is responsible for the formation of the N-N bond leading to N_2 (Equation 5.2).

$$2H^+ + 2e^- + 2NO \rightarrow N{=}N{=}O + H_2O \quad \text{(Eq. 5.2)}$$

Interstingly, denitrifying NO reductases (NORs) show structural similarity to the heme-copper superfamily of terminal oxidases, which catalyze the reduction of O_2 to water. As with terminal oxidases, electron carriers to NOR may involve quinol, di-copper, or soluble and membrane bound cytochrome *c* [Richardson, 2000; Suharti et al., 2001]. NORs from *Paracoccus denitrificans* and other gram-positive bacteria have

---

* Material in this chapter has been published in this or similar form in *J. Am. Chem. Soc.* and is used here with permission of the American Chemical Society.

Lu, S., Suharti, de Vries S., and Moënne-Loccoz, P. (2004) Two CO molecules can bind concomitantly at the diiron site of NO reductase from Bacillus azotoformans. *J. Am. Chem. Soc.* **126,** 15332-15333.

been most extensively studies and are designated cNOR as they include a heme *c* on a NORc subunit (17 kDa). The second subunit, NorB (53 kDa), is homologous to the large subunit of cytochrome oxidases with six conserved histidine residues that bind one low-spin heme *b* (bis-His), one high-spin heme *b* (mono-His), and one non-heme iron (tris-His) [Girsch and de Vries, 1997; Ostermeier et al., 1997; Hendriks et al., 1998]. The non-heme iron is labeled Fe_B in analogy with Cu_B in cytochrome oxidase. A detailed RR study has confirmed that one heme *b* is a low-spin species, while the other, heme b_3, is a pentacoordinated high-spin heme which displays a unique absorbance at 595-600 nm in the oxidized state [Moënne-Loccoz and de Vries, 1998b]. Soluble or membrane-bound *c* cytochromes or pseudoazurin are predicted to transfer electrons to the heme *c* group of NorC, which via the low-spin heme *b* in NorB reduces the binuclear heme/non-heme diiron site where NO is reduced to N_2O.

Several gram-negative bacteria, e.g. *Ralstonia eutropha*, and archaeon such as *Pyrobaculum aerophilum*, have been shown to utilize NOR enzymes lacking a *c*-type cytochrome, and instead include a quinol binding site at their electron acceptor side [Cramm et al., 1999; de Vries et al., 2003].

Recently NOR was also isolated from the gram-positive bacteria *Bacillus azotoformans* [Suharti et al., 2001]. The purified enzyme consists of two subunits and contains one non-heme iron, two copper atoms, and two *b*-type hemes per enzyme complex, but no heme *c*. The enzyme contains a binuclear $Cu_2(\mu\text{-Cys})_2(His)_2$ core analogous to Cu_A in cytochrome *c* oxidase, which can transfer one-electron by cycling between $(Cu_2)^{2+}$ and $(Cu_2)^{3+}$ [Tsukihara et al., 1995; George et al., 2001; Iwata et al., 1995]. In addition, the protein can accept electrons from menaquinol via a putative quinol binding site. Thus, differences between NORs lie in their respective electron acceptor sites and can be arranged in three classes: cNOR, qNOR and qCu_ANOR (Fig. 5.1) [de Vries and Schroder, 2002]. Notably, all NORs characterized to date present poor oxidase activity and do not coupled NO reductase activity to vectorial proton pumping [Giuffre et al., 1999; Shapleigh and Payne, 1985].

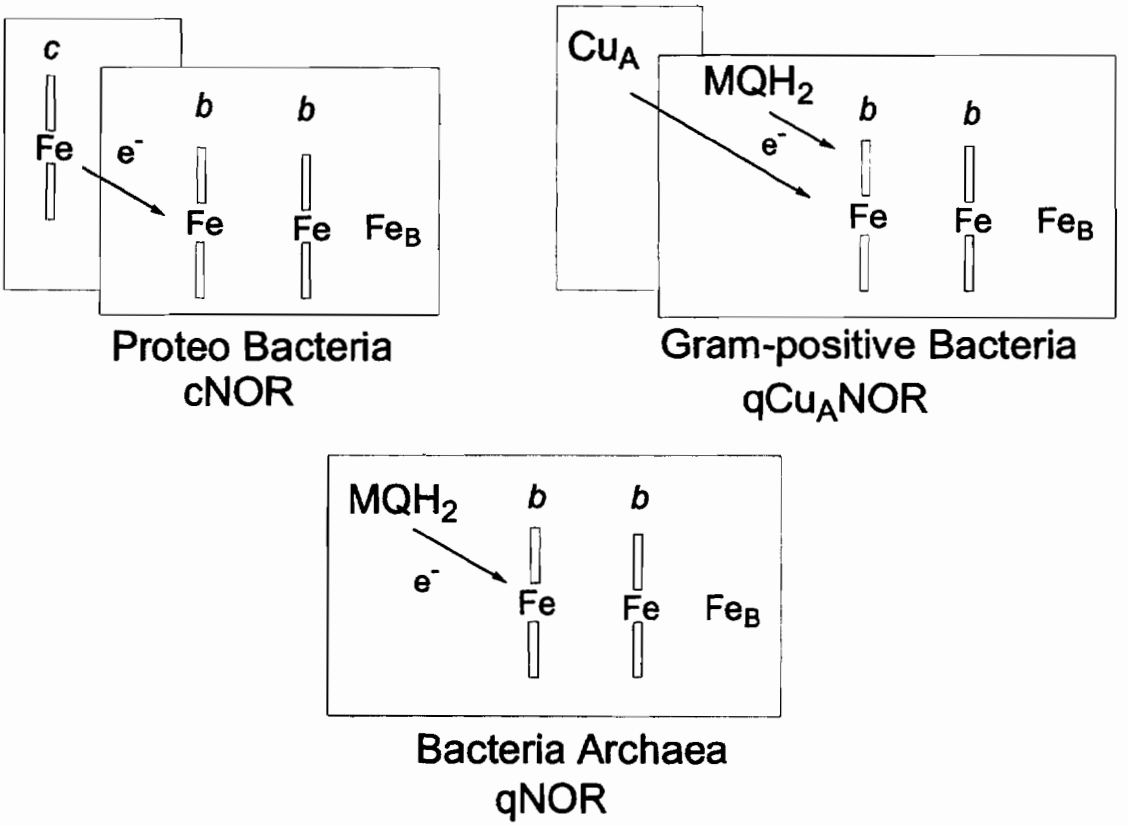

Fig. 5.1 Various types of NOR proteins in bacteria and archaea.

5.2 Putative Mechanistic Model

Although no crystal structure is yet available for any NOR, the heme Fe–Fe_B distance is expected to be approximately 3.5 Å based on the ν_{as}(Fe-O-Fe) observed in oxidized cNOR [Moënne-Loccoz et al., 2000]. This distance is much shorter that the 5 Å distance between the heme a_3 and Cu_B in cytochrome oxidase [Tsukihara et al., 1996; Ito et al., 1991]. This difference is consistent with the lack of a μ-oxo bridge in cytochrome oxidase where the magnetic coupling between the two metals is proposed to originate from a peroxide bridge, or via hydroxy and aqua ligands of Cu_B and heme a_3 [Ralle et al., 1999; Ferguson-Miller and Babcock, 1996]. There is a general agreement that reduction of NO is catalyzed by the dinuclear center made up of the high-spin heme *b* and Fe_B, and if both metals bind one NO molecule, the close proximity of these two irons may be essential to promote the formation of a N-N bond [Moënne-Loccoz and de Vries, 1998; Moënne-Loccoz et al., 2000;Wasser et al., 2002].

RR data on cNOR show that in the fully reduced enzyme the catalytic heme is pentacoordinated to a neutral histidine, while this histidine ligand is lost in the oxidized state (Fig. 5.2). Indeed, the ferric heme remains five-coordinated and its sole axial ligand is an oxo group bridging the two irons. From the description of the oxidized and reduced state of the enzyme, a catalytic cycle was proposed [Girsch and de Vries, 1997; Moënne-Loccoz et al., 2000]. Reduction of the diiron site weakens the oxo bridge and favors the formation of the heme Fe(II)-His bond. The enzyme can bind one NO molecule per ferrous iron. As observed in several hemoproteins, e.g., hemoglobin or soluble guanylyl cyclase [Deinum et al., 1996; Kharitonov et al., 1995], the heme Fe(II)-His bond is broken after the binding of NO, forming an initial six-coordinate heme-nitrosyl, which then goes on to form a pentacoordinate heme nitrosyl complex [Stone and Marletta, 1996]. The close proximity of the two nitrosyl groups destabilizes these otherwise poorly reactive $\{FeNO\}^7$ species and promotes formation of the N-N bond. The product N_2O leaves the active site while formation of an oxo bridge completes the catalytic cycle.

To test the hypothesis that the catalytic cycle of NOR transits through a iron-nitrosyl dimer, we used an analogous strategy to the one we used in previous chapters on O_2-activating diiron enzymes, using CO as an NO analog. We compare two NO reductases from denitrifying bacteria, cNOR from *Paracoccus denitrificans*, and qCu_ANOR from *Bacillus azotoformans*, to determine whether mechanistic differences exist within this family of enzymes. Ligand shuttling, electron transfer and proton translocation, are discussed.

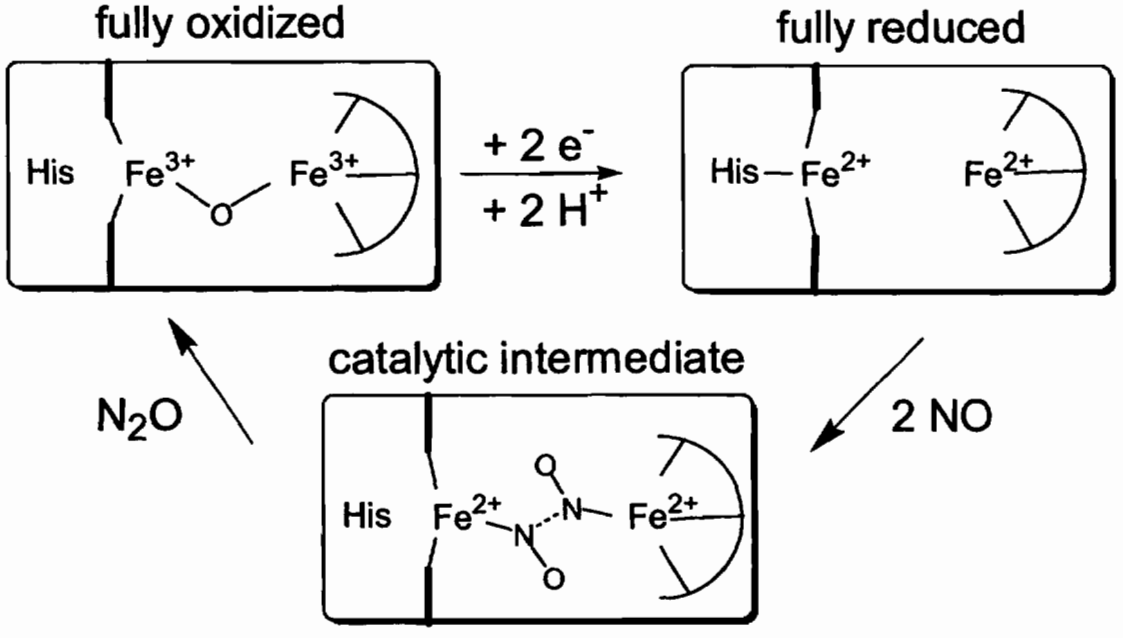

Fig. 5.2 Proposed catalytic turnover of cNOR [Moënne-Loccoz et al., 2000]. RR studies demonstrated that in the oxidized enzyme, the heme is 5-coordinate with an axial μ-oxo ligand that bridges the two iron(III) ions. Upon reduction, the μ-oxo bridge is hydrolyzed, but the heme iron remains 5-coordinate through ligation to an axial histidine.

Originally published as Fig. 4 in:

Moënne-Loccoz, P., Richter, O. H., Huang, H., Wasser, I. M., Ghiladi, R. A., Karlin, K. D., and de Vries, S. (2000) Nitric oxide reductase from Paracoccus denitrificans contains an oxo-bridged heme/non-heme diiron center. *J. Am. Chem. Soc.* **122**, 9344-9345.

5.3 Materials and Methods

The cNOR and qCu_ANOR was purified as previously reported and stored under liquid nitrogen [Girsch and de Vries, 1997; Suharti et al., 2001]. Typical enzyme concentrations for RR experiments were 50-100 μM and 150-200 μM for FTIR, in a pH 7.0 buffer solution of 20 mM potassium phosphate with 0.05% dodecyl maltoside. Reduction to the ferrous state was achieved by addition of 1 μL aliquots of a 100 mM sodium dithionite solution to an argon-purged 22-μL solution of reduced enzyme. CO was added to the headspace to reach ~1atm partial pressure (^{12}CO, CP grade, Air Products; and ^{13}CO, 99% ^{13}C, Cambridge Isotope Laboratory). The CO complexes of NOR were then transferred to Raman capillaries, or loaded to FTIR cells inside the anaerobic glove box. The UV-vis spectra of the samples were collected in the same cells before and after the RR and FTIR experiments to confirm the formation of the CO-complex and its stability during data collection [Loehr and Sanders-Loehr, 1993].

RR spectra were obtained on a McPherson 2061/207 spectrograph (0.67 m) equipped with a Princeton Instruments liquid-N_2-cooled (LN-1100PB) CCD detector. Excitation sources consisted of an Innova 302 krypton laser (413 nm) and a Liconix 4240NB He/Cd laser (442 nm). Spectra were collected in a 90°-scattering geometry on samples at room temperature with a collection time of a few minutes, whereas longer times and a backscattering geometry were used for low-temperature experiments. For FTIR experiments, a 21-μL droplet of the CO-treated samples was deposited on a CaF_2 window in an anaerobic glove box (Coy laboratory products, Inc.). A second CaF_2 window was dropped on the sample to form an optical cell with a pathlength controlled by a 50-μm Teflon spacer. For room temperature FTIR experiments, the cell was connected to a thermostatic water bath set at 20 °C. For low temperature experiments, the same IR cell used at room temperature was attached to a closed cycle cryogenic system (Displex, Advanced Research Systems, Inc.). The FTIR spectra were obtained on a Perkin-Elmer system 2000 equipped with a liquid-N_2 cooled MCT detector. Sets of 2000-scan accumulations were acquired at a 4 cm^{-1} resolution.

Continuous illumination of the samples was performed directly in the FTIR sample chamber with a 50 W tungsten lamp after filtering out heat and NIR emission.

5.4 Spectroscopic Studies

UV-vis Spectroscopy

Exposure of dithionite-reduced qCu_ANOR to CO results in UV-vis absorption changes that are consistent with the binding of CO to a high-spin heme (Fig.5.3). In the reduced enzyme, absorbance maxima in qCu_ANOR are at 425, 530, and 560 nm, respectively, consistent with the presence of heme *b* and absence of heme *c*. The difference spectra show the effect in α/β and γ bands upon CO binding (Fig. 5.3C). The spectrum is very similar to the CO-difference spectra obtained for ferrous myoglobin and for the NO reductase from *P. denitrificans* (cNOR) [Girsch and de Vries, 1997].

RR Spectroscopy

The high-frequency RR spectrum of dithionite-reduced NOR obtained with 413-nm excitation is shown in Figure 5.4 (trace A). RR spectra of metalloporphyrins obtained with Soret excitation are dominated by totally symmetric modes of the porphyrin ring. In reduced NOR, the oxidation-state marker band ν_4 is observed at 1360 cm^{-1}, a frequency characteristic of ferrous hemes. The absence of a shoulder at ~1372 cm^{-1} confirms the complete reduction of the enzyme. The spin-state marker band ν_3 has two contributions at 1472 and 1492 cm^{-1}, revealing the presence of both high- and low-spin species, respectively (Fig. 5.4, A). Because the relative resonance enhancement of the two hemes present in NOR is unknown, one cannot quantitate the ratio from their respective RR signals. Nonetheless, these data are consistent with a 1:1 HS:LS ratio.

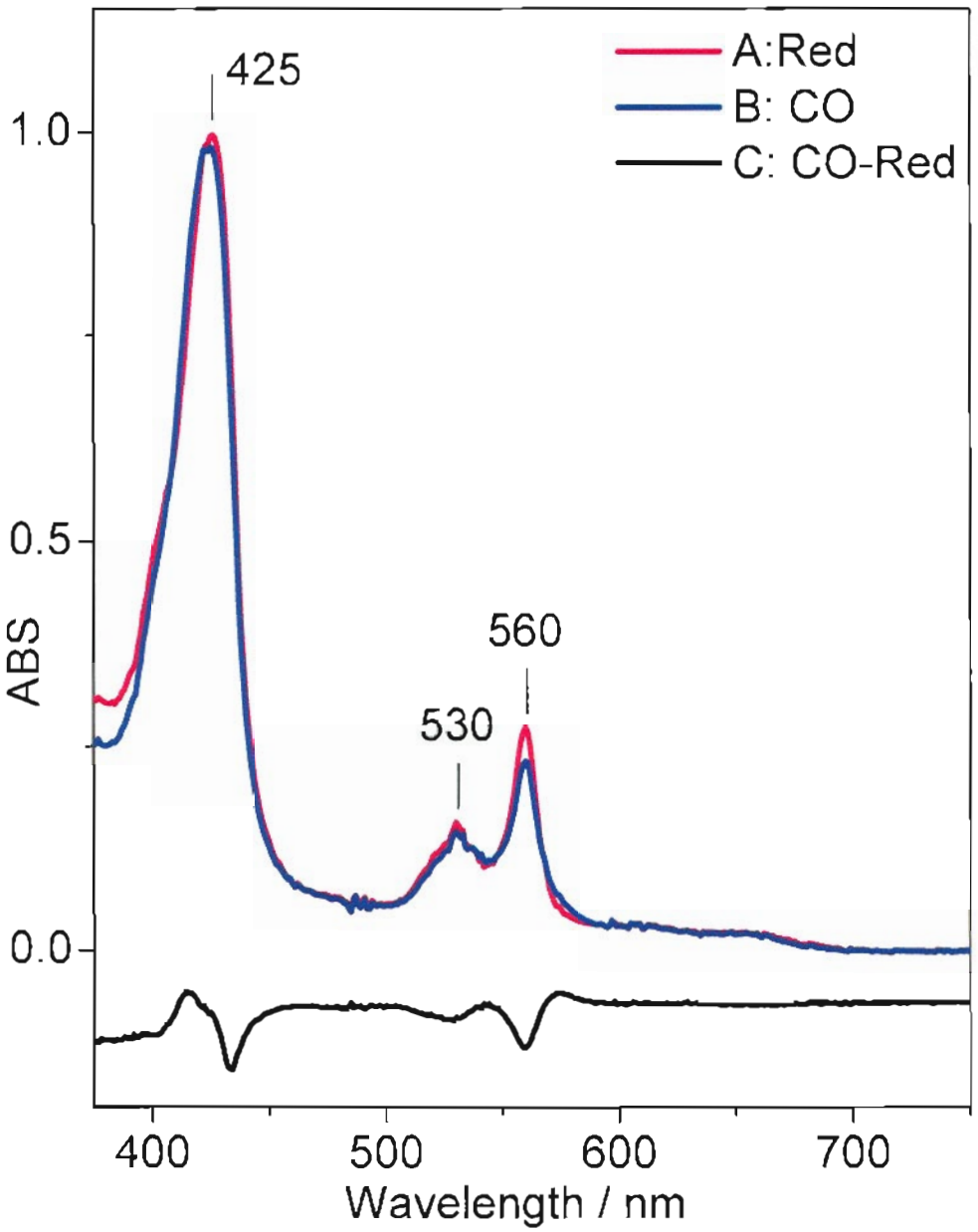

Fig 5.3 UV-vis absorption spectra of reduced qCu_ANOR (A), its CO complex (B), and the difference spectrum of "CO bound" minus "reduced" (C). These spectra were obtained in a 0.1-cm pathlength capillary and enzyme concentration of 45 μM.

Upon addition of CO to reduced NOR, the appearance of a high-frequency band on the ν_4 vibration at 1372 cm^{-1}, as well as changes in the ν_3 region with a loss of the 1472 cm^{-1} band of the high-spin species, indicates CO binding (Fig. 5.4B). Similar spectral changes are observed in deoxymyoglobin upon binding of CO [Tsubaki et al., 1982]. The power dependence of the observed RR changes is consistent with the photolabile character of heme-CO complexes. At higher laser power or at temperature of 15K, the 1372 cm^{-1} characteristic of the Fe^{II}-CO complex diminishes as CO is released. We conclude that CO binds to the high-spin *b* heme of fully reduced NOR and converts it to a 6-coordinate low-spin species.

The low-frequency RR spectra of the CO complex to reduced NORs are shown in Figure 5.5. The ^{13}CO isotopic substitution study allows unambiguous identification of the Fe-CO vibrational modes. The RR band of qCu_ANOR-CO at 495 cm^{-1} (downshifts 3 cm^{-1} with ^{13}CO) is assigned to the ν_{Fe-CO} stretching mode and compared well with the 477cm^{-1} band in cNOR-CO [Moënne-Loccoz et al., 2000]; A small RR band of qCu_ANOR-CO at 526 cm^{-1} (downshifts 3 cm^{-1} with ^{13}CO) is consistent with the ν_{Fe-CO} stretching mode of a 5-coordinated heme [Li and Spiro, 1988; Ray et al., 1994], but this species is absent at 90 K. Thus, as proposed with the binding of NO, CO binding to qCu_ANOR may promote the dissociation of the Fe-His bound. While the ν(Fe-His) was measured in fully reduced cNOR [Moënne-Loccoz and de Vries, 1998], no ν(Fe-His) mode could be detected in qCu_ANOR, supposedly because of a lack of resonance enhancement, which further suggest variations in the proximal ligand arrangement in qCu_ANOR and cNOR.

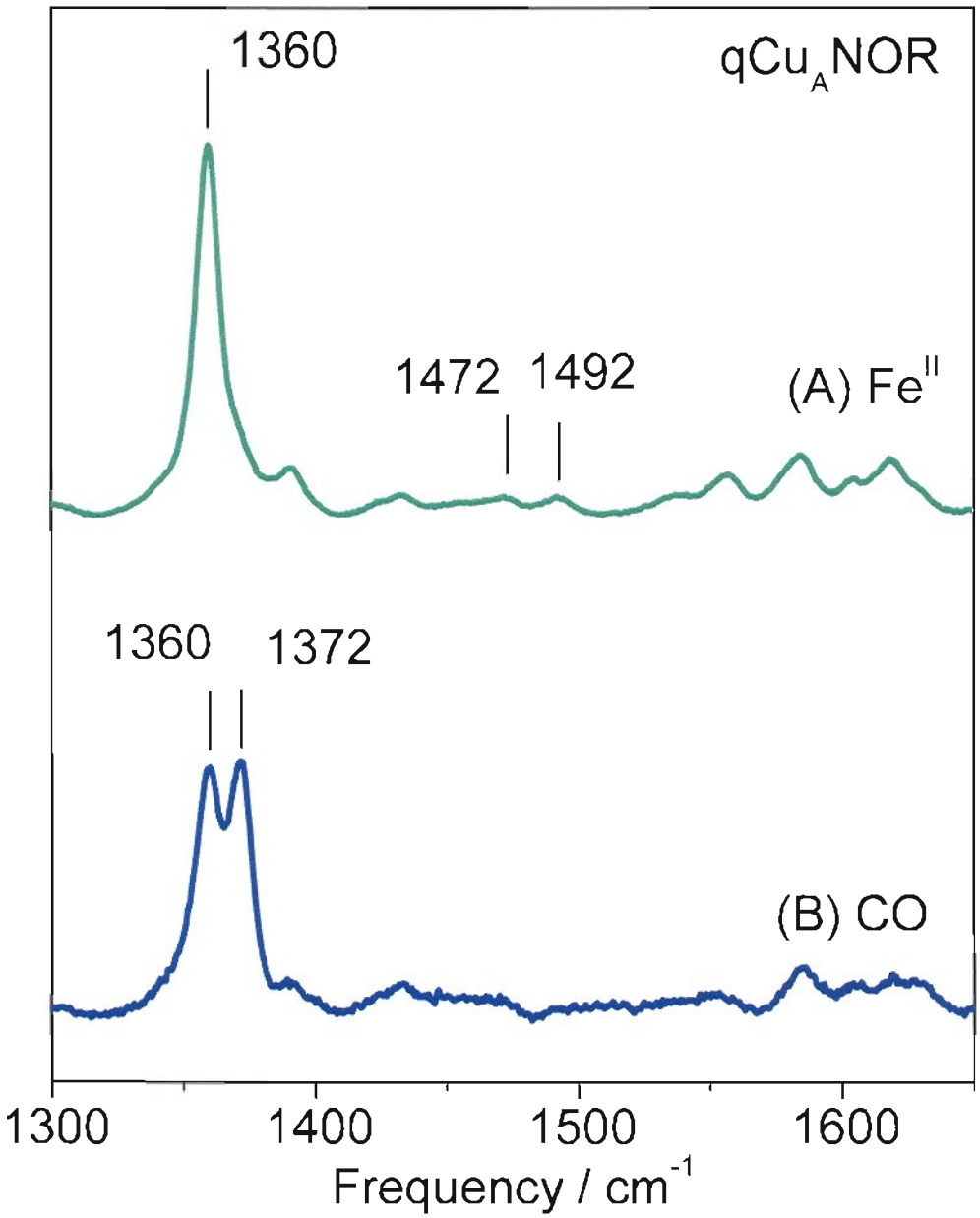

Figure 5.4 Room temperature RR spectra of dithionite-reduced qCu$_A$NOR before (green, A), and after (blue, B) exposure to CO. The 413-nm laser excitation was kept below 0.5 mW and the sample was mounted to a reciprocating translation stage to prevent photodissociation of the heme-CO complex. The heme skeletal mode ν_4 is known as the oxidation state marker band and is observed at ~1360 cm^{-1} in reduced hemes but at ~1370 cm^{-1} in reduced heme-carbonyl complexes.

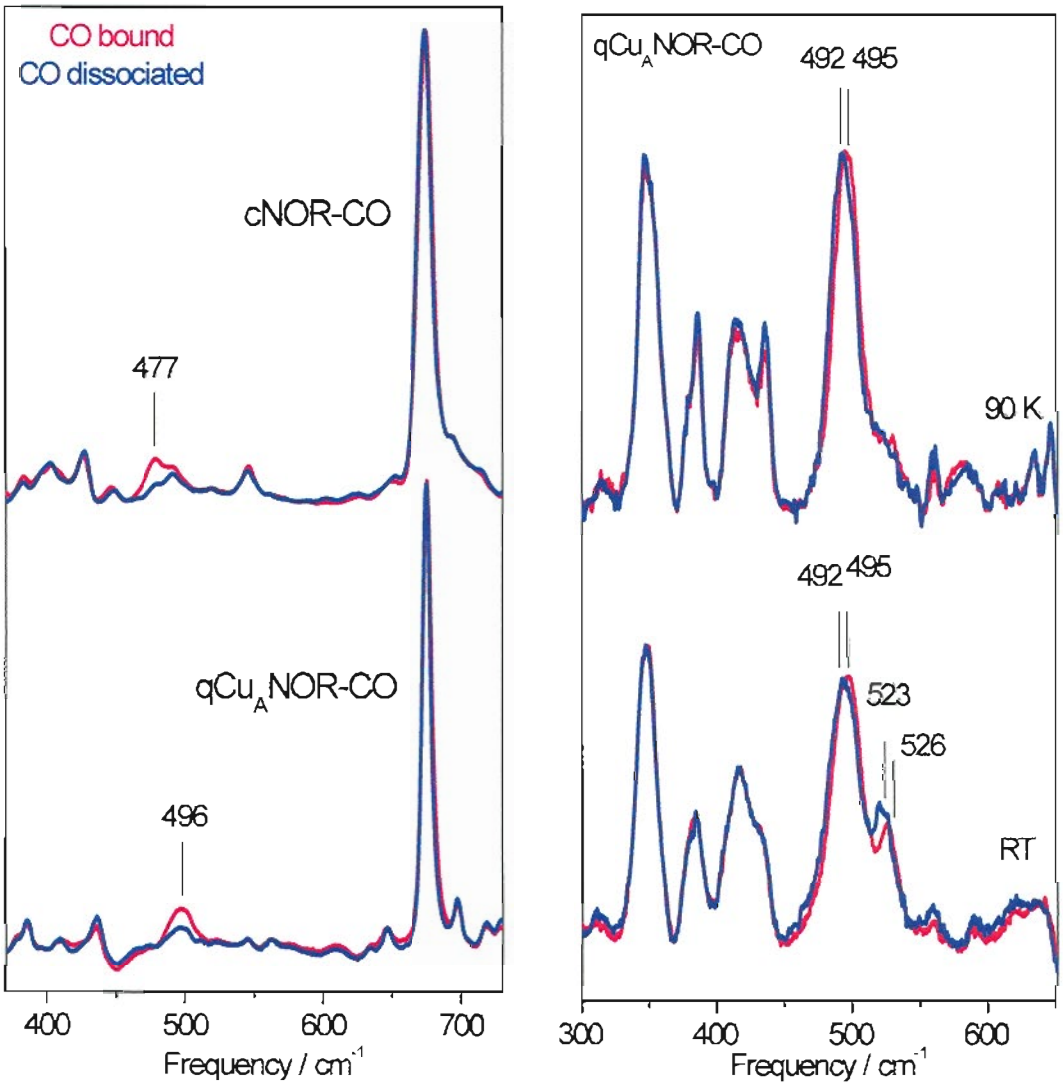

Fig. 5.5 Low-frequency RR spectra of qCu$_A$NOR-CO and cNOR-CO obtained with a 413-nm excitation.
- Left panel: RR spectra obtained at 100 K where CO geminate rebinding is prominent (red) and at 15 K where the photolyzed complex is trapped (blue).
- Right panel: RR spectra of the ^{12}CO (red) and ^{13}CO (blue) complexes of qCu$_A$NOR obtained at 90 K (top) and room temperature (bottom).

FTIR Spectroscopy

Room temperature (^{12}CO minus reduced) FTIR difference spectrum of cNOR identifies only one ν(C-O), but two ν(C-O)s are obtained with qCu_ANOR (Fig. 5.6, left). For cNOR, the 1973 cm^{-1} ν(C-O) stretching mode characterized here by FTIR was also observed in the RR spectrum at 1970 cm^{-1} by 44 cm^{-1} downshift with ^{13}CO [Moënne-Loccoz and de Vries, 1998b]. For qCu_ANOR, the band at 1972 cm^{-1} downshifts by 45 cm^{-1} with ^{13}CO and is readily assigned to the ν(C-O) from the heme-CO complex. The second band at 2068 cm^{-1}, not found in cNOR, downshifts 47 cm^{-1} to 2021 cm^{-1} with ^{13}CO. This ν(C-O) is consistent with a non-heme iron carbonyl complex (Fe_BCO) where backbonding donation from the iron d_π orbitals to the carbonyl π^* orbitals is weakened compared to that observed in heme-CO complexes. Taking into account the increased extinction coefficient of higher ν(C-O) vibrations [Alben et al., 1981], the integrated areas of the non-heme and heme ν(C-O) suggest that the two iron-carbonyl species are present in comparable concentrations.

At 15 K, FTIR ("dark" minus "illuminated") difference spectrum of cNOR displays a symmetric and sharp ν(C-O) band at 1972 cm^{-1} (Fig. 5.6, right) that is nearly identical to the signal observed in the room temperature data. This signal is consistent with the photolabile character of heme-CO complexes. The isotopic shifts of these signals with ^{13}CO demonstrate that all correspond to ν(C-O) modes (Fig. 5.6, right-C). Moreover, the intensity of the 1972 cm^{-1} band in the light induced FTIR difference spectrum indicates that complete photodissociation of the heme-CO complex and rebound inhibition is achieved at 15 K. Increasing the temperature to 100 K or above allows total rebinding of the photodissociated CO to the heme iron (Fig. 5.7, left). This temperature dependence is consistent with an efficient geminate recombination process as observed in myoglobin rather than a non-geminate recombination process as found in cytochrome *c* oxidase. Indeed, in cytochrome *c* oxidase (CcO), the photodissociated CO binds to the Cu_B and is released only above 200 K [Alben et al., 1981]. The 2121 cm^{-1} negative band is assigned to the dissociated

CO in substrate pocket, which is also observed in Mb-CO complex with a frequency of 2130 cm^{-1}.

The FTIR ("dark" minus "illuminated") difference spectrum of qCu_ANOR obtained at 15 K is much more complex. A group of partially resolved components form a cluster of bands between 1950 and 1990 cm^{-1} that can be assigned to distinct but comparable heme-CO conformers within the substrate pocket. Such distributions of heme ν(C-O) have been observed in many hemoproteins including globins and terminal oxidases [Ansari et al., 1987; Einarsdottir et al., 1989; Wang et al., 1995; Mitchell et al., 1996]. In addition to this cluster of bands, we observe a positive band at 1910 cm^{-1} and a S-signal with a positive band at 2045 cm^{-1} and a negative band at 2066 cm^{-1} (Fig. 5.7, right). Comparison of different samples of qCu_ANOR show some variation in the relative intensity of the ~1970 cm^{-1} cluster of bands compared to that of the 1910 and 2045/2066 cm^{-1} signals, but the intensity ratio of the latter two signals remains constant. The interdependence of these two photoinduced features is also confirmed by the influence of temperature on the FTIR difference spectra. Specifically, when the temperature is raised to ~100 K, the 1910 cm^{-1} band and the 2045/2066 cm^{-1} S-signal are unaffected, but the intensity at ~1970 cm^{-1} decrease presumably because of geminate rebinding of the photodissociated CO to the heme iron, as is seen at high chloride concentration.

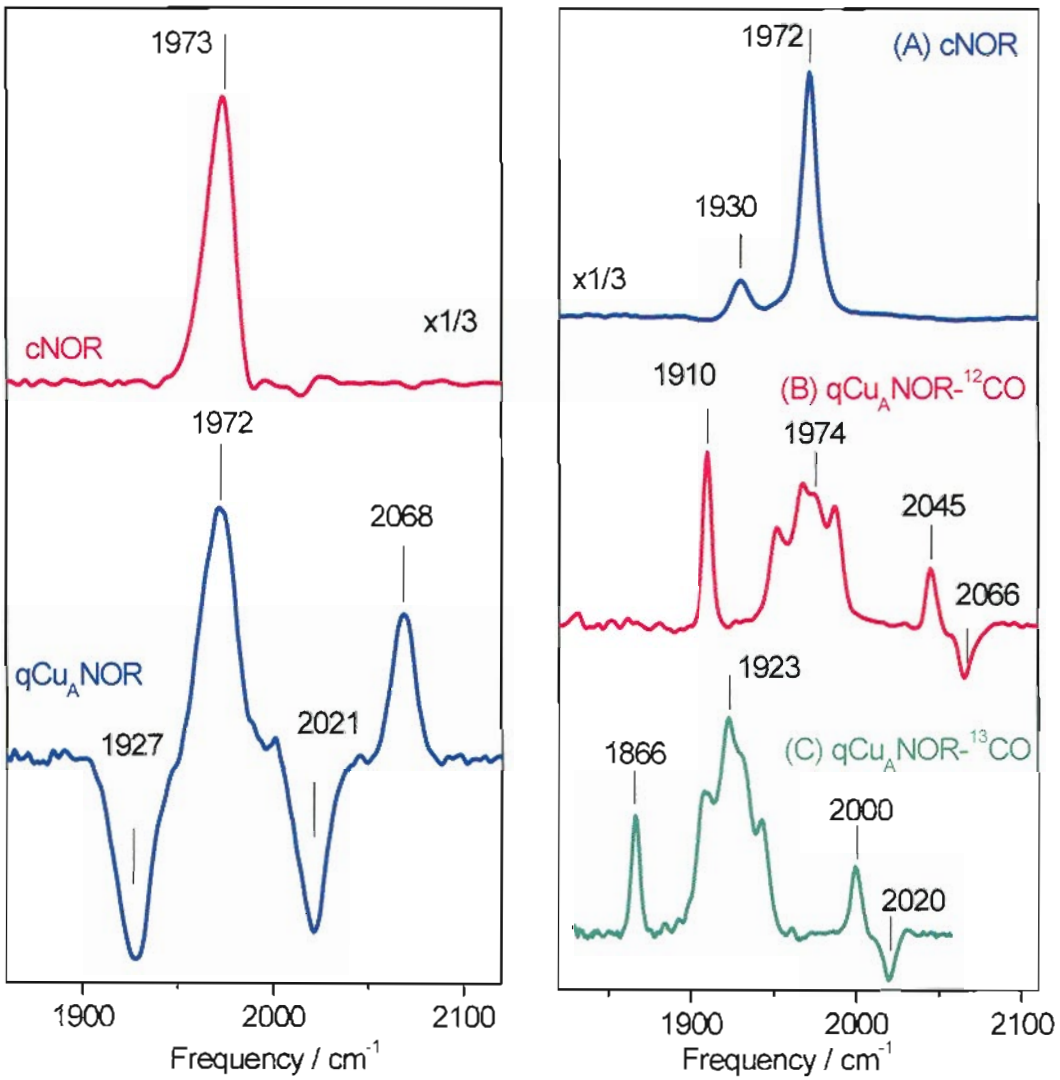

Fig. 5.6 FTIR spectra of cNOR-CO and qCu$_A$NOR-CO.
- Left panel: Room temperature spectra of cNOR (top, ^{12}CO – reduced) and qCu$_A$NOR (bottom, ^{12}CO – ^{13}CO)
- Right panel: Low temperature Light induced difference FTIR spectra of cNOR (top) and qCu$_A$NOR (middle). The ^{13}CO spectra of qCu$_A$NOR are also shown (bottom). Comparison of the ^{13}CO trace with ^{12}CO trace shows isotopic shifts expected for all ν(C-O) modes. This comparison of different qCu$_A$NOR samples also illustrates the minor variations in relative intensities between ν(C-O) modes.

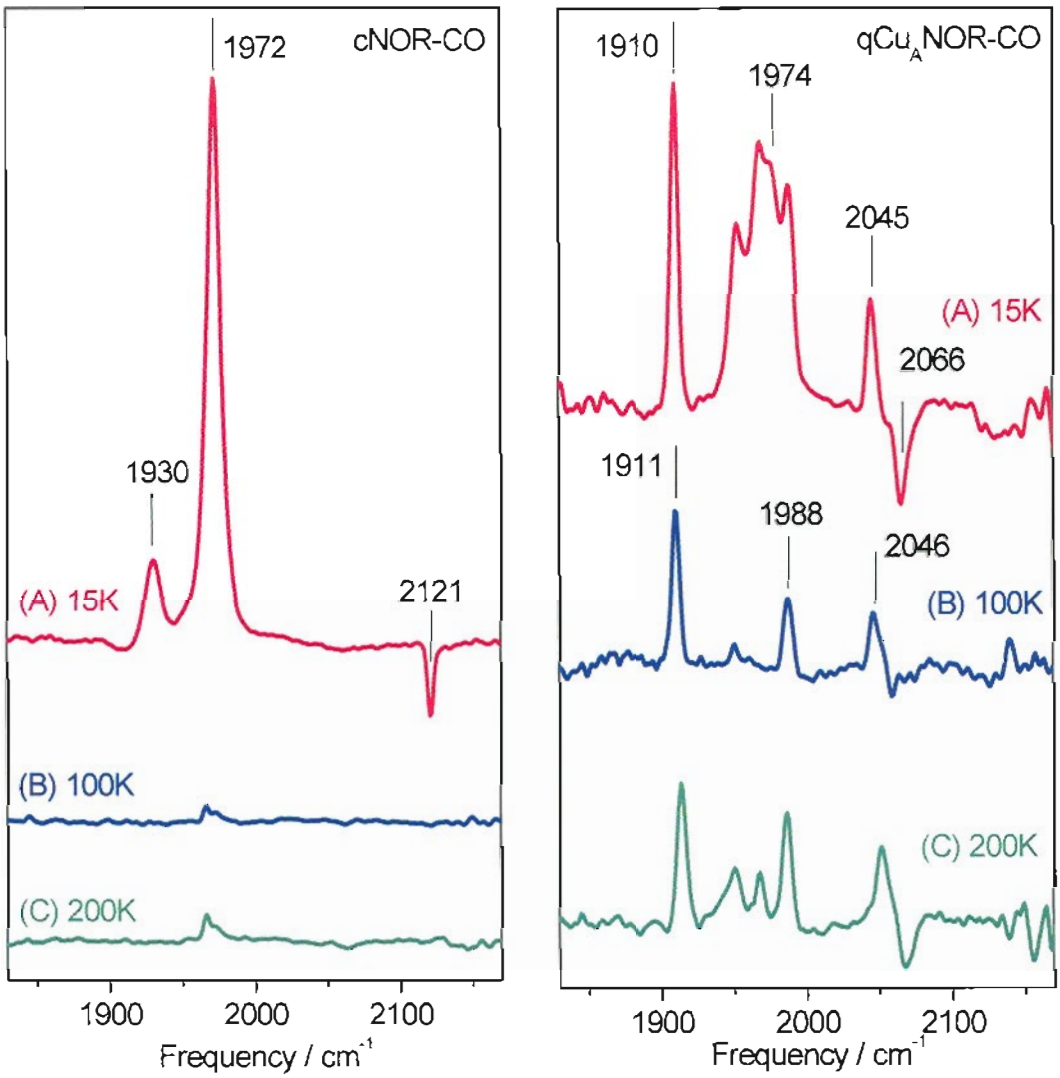

Fig. 5.7 Light-induced FTIR difference spectra of cNOR-CO and qCu_ANOR-CO.
- Left panel: Spectra of cNOR-CO obtained at 15 K (red), 100 K (blue), and 200 K (green). The enzyme concentration is 0.4 mM with a 50-μm Teflon spacer.
- Right panel: Spectra of qCu_ANOR-CO obtained at 15 K (red), 100 K (blue), and 200 K (green). The enzyme concentration is 0.2 mM with a 50-μm Teflon spacer.

5.5 Effect of Chloride

As described above, the room temperature (^{12}CO minus ^{13}CO) FTIR difference spectrum identifies two ν(C-O)s (Fig. 5.8, left-A) when Cl^- is absent. Interestingly, if qCu_ANOR is exposed to high chloride concentration (i.e., 3 M), the ν(C-O) from Fe_BCO at 2068 cm^{-1} is lost and only the heme-CO is detected as a single ν(C-O) band at 1970 cm^{-1} (Fig. 5.8, left-B). This form of qCu_ANOR is equivalent to that of cNOR, where FTIR detects CO binding exclusively at the heme, regardless of the chloride content. At 15 K and in the presence of 3 M chloride, ("dark" minus "illuminated") FTIR difference spectrum displays a single ν(C-O) at 1970 cm^{-1} (Fig. 5.8, left-D) that is nearly identical to the signal observed in the room temperature data. In the absence of excess chloride, the ("dark" minus "illuminated") FTIR difference spectrum obtained at 15 K suggested that two CO molecules bind concomitantly at the diiron site of qCu_ANOR.

During our attempt to determine the binding affinity constant for chloride in qCu_ANOR, it quickly became apparent that the effect of chloride is complex and perturbed by other factors, such as detergent concentration (dodecyl maltoside) and protein monomer-dimer equilibrium. To eliminate concerns of detergent interference and to better simulate the native environment of the enzyme, we reproduced our FTIR experiments directly on *B. azotoformans* membrane fragments (Fig. 5.8, right). Whole membrane FTIR analyses targeting CO complexes of terminal oxidases have been used in the past by James Alben and collaborators [Shapleigh et al., 1992; Mitchell et al., 1998]. Membranes were isolated in 50 mM Tris-HCl buffer, followed by successive washes in phosphate buffer to remove excess chloride before reduction and exposure to CO. As observed upon CO photolysis with the purified protein, a ν(C-O) band indicative of a semi-bridging heme-CO was found at 1914 cm^{-1} but disappeared when membranes were exposed to a high concentration of chloride (Fig. 5.8, right-B).

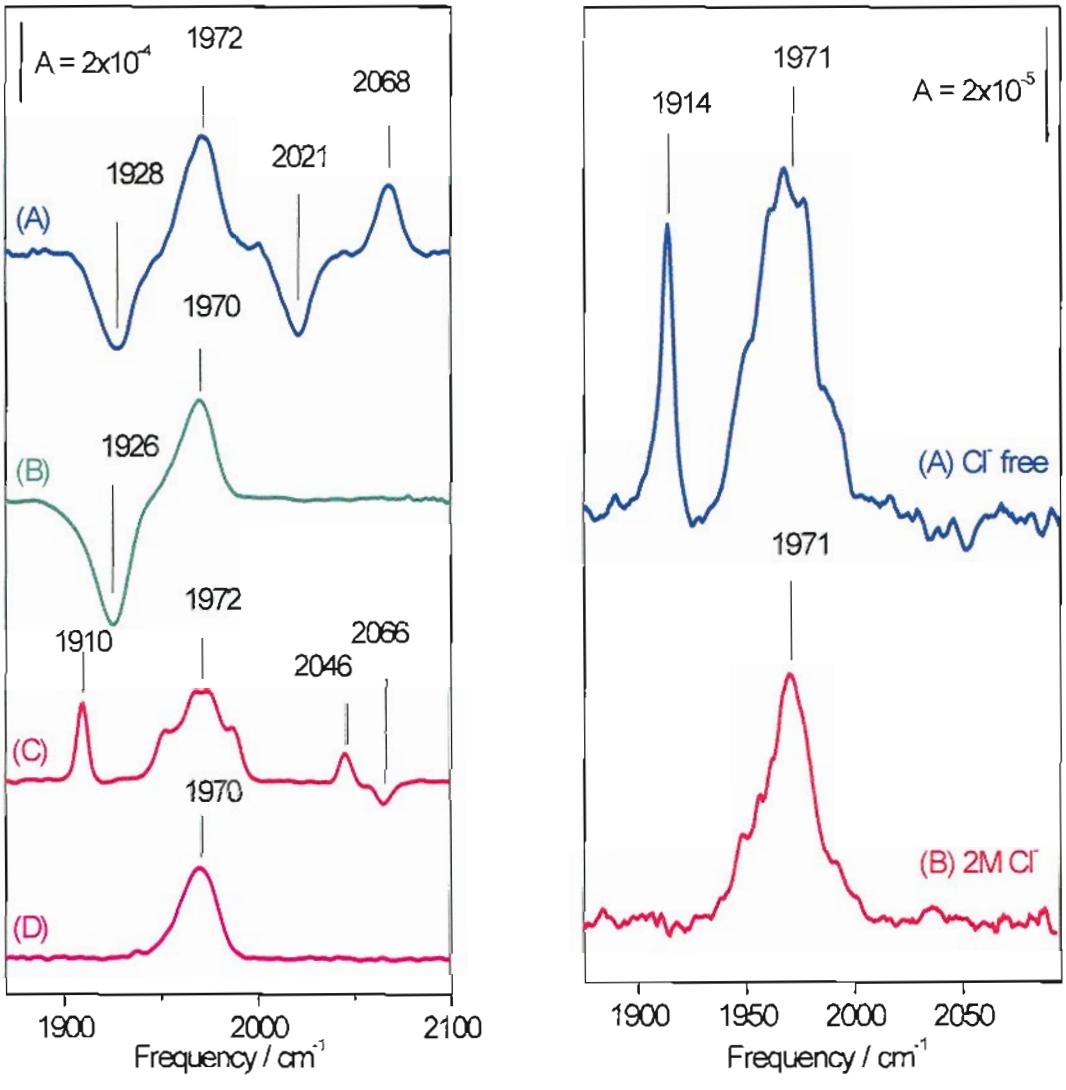

Fig. 5.8 FTIR spectra of qCu_ANOR-CO.
- Left panel: ^{12}CO minus ^{13}CO difference spectra of isolated enzyme are obtained at room temperature with Cl^- free (A) and in presence of 3 M Cl^- (B). The corresponding 15 K light-induced difference spectra are also shown (C and D, respectively).
- Right panel: Low temperature light induced difference spectra of membrane fragment with Cl^- free (A) and in presence of 3 M Cl^- (B).

5.6 Discussion

Our results from RR and FTIR lead us to the following interpretation (Fig. 5.9). As stated above, the 1970 cm^{-1} cluster of bands in qCu_ANOR is assigned to ν(C-O) bands from the heme iron carbonyl in distinct configurations within the active site. Accordingly, discreet configurations are observed at cryogenic temperatures while in room temperature spectra of these configurations lead to a Gaussian distribution centered at 1973 cm^{-1}. In addition to these discreet but comparable heme-CO configurations, a ν(C-O) at 1910 cm^{-1} correspond to a semi-bridging configuration of the heme-CO with the non-heme iron that is stabilized at low temperature. Indeed, carbonyls bridging two metals display ν(C-O) bands downshifted by as much as 200 cm^{-1} compared to terminal CO groups, and semi-bridging configurations with intermediate ν(C-O) have also been reported in inorganic compounds [Nakamoto, 1997]. As the heme-CO adopts a bridging configuration between the two irons, the electron density on the non-heme iron increases and results in a ν(C-O) shift in Fe_BCO from 2066 cm^{-1} to 2045 cm^{-1}. Thus, the photodissociation of the bridging CO is accompanied by an S-signal originating from Fe_BCO that occurs at 2045 cm^{-1} in the dark spectrum and at 2066 cm^{-1} after illumination (Fig. 5.9, A). This latter frequency matches the 2068 cm^{-1} stretch observed for the non-heme Fe-CO at room temperature where the bridging CO is not observed. Concomitant detection by room temperature FTIR of the ν(C-O) from the heme a_3 and the Cu_B carbonyl complexes has been reported previously in cytochrome ba_3 from *Thermus thermophilus* [Koutsoupakis et al., 2002]. However, these data were interpreted in terms of a binding equilibrium involving a single CO ligand bound either to heme a_3 or Cu_B within the active site. Accordingly, the CO bound to heme a_3 readily binds to the Cu_B site upon photodissociation from the heme moiety. In contrast, photodissociation of the heme-CO complex in qCu_ANOR results in a perturbation of the ν(C-O) signal associated with the non-heme-CO complex indicating that two molecules of CO bind concomitantly at the diiron site.

Chloride can affect metalloproteins structure and function via direct binding to the metal center or by inducing conformational changes through interactions with protein side chains. For example, chloride acts as a heterotrophic ligand in hemoglobin where it binds at the 2,3-diphosphoglycerate site. In CcO, XAS studies have shown direct chloride binding to Cu_B. In preliminary experiments with *B. azotoformans* membrane fragments rather than isolated qCu_ANOR, we have confirmed that the chloride effect is also observed, but more experiments are required to determine whether the decreased CO affinity at the non-heme iron site is due to direct coordination to $Fe_B(II)$ or if chloride acts indirectly by perturbing the substrate pocket structure. Chloride could mimic a native effector, e.g., a specific anionic molecule, a small regulatory protein or a specific lipid interacting with the protein matrix. Our FTIR results have revealed significant variations in CO binding properties for cNOR and qCu_ANOR, and for solubilized NOR and membrane fragments. The effect of chloride on the family of terminal oxidase is notoriously complex and range from direct binding to cuprous Cu_B [Scott et al., 1988; Li et al., 1987; Ralle et al., 1999], to bridging the heme a3 iron(III) and $Cu_B(II)$ [Moody, 1996; Fabian et al., 2001], and to binding at heterotropic sites [Li and Palmer, 1993; Orii et al., 1995; Moody, 1996]. The same is likely to be true with NORs, and it is easy to imagine that the chloride binding affinity for these binding sites could vary between membrane-embedded and solubilized enzymes, and between isoform of NORs.

In conclusion, while conditions can be found when only one CO bind at the fully reduced active sites of NORs, our study show that two interacting iron-carbonyls can be present at the same time at the diiron site. This experimental observation clearly strengthens a mechanistic model where the formation of an iron-nitrosyl dimer, i.e., a $[\{FeNO\}^7]_2$ unit, promotes the N-N bond formation.

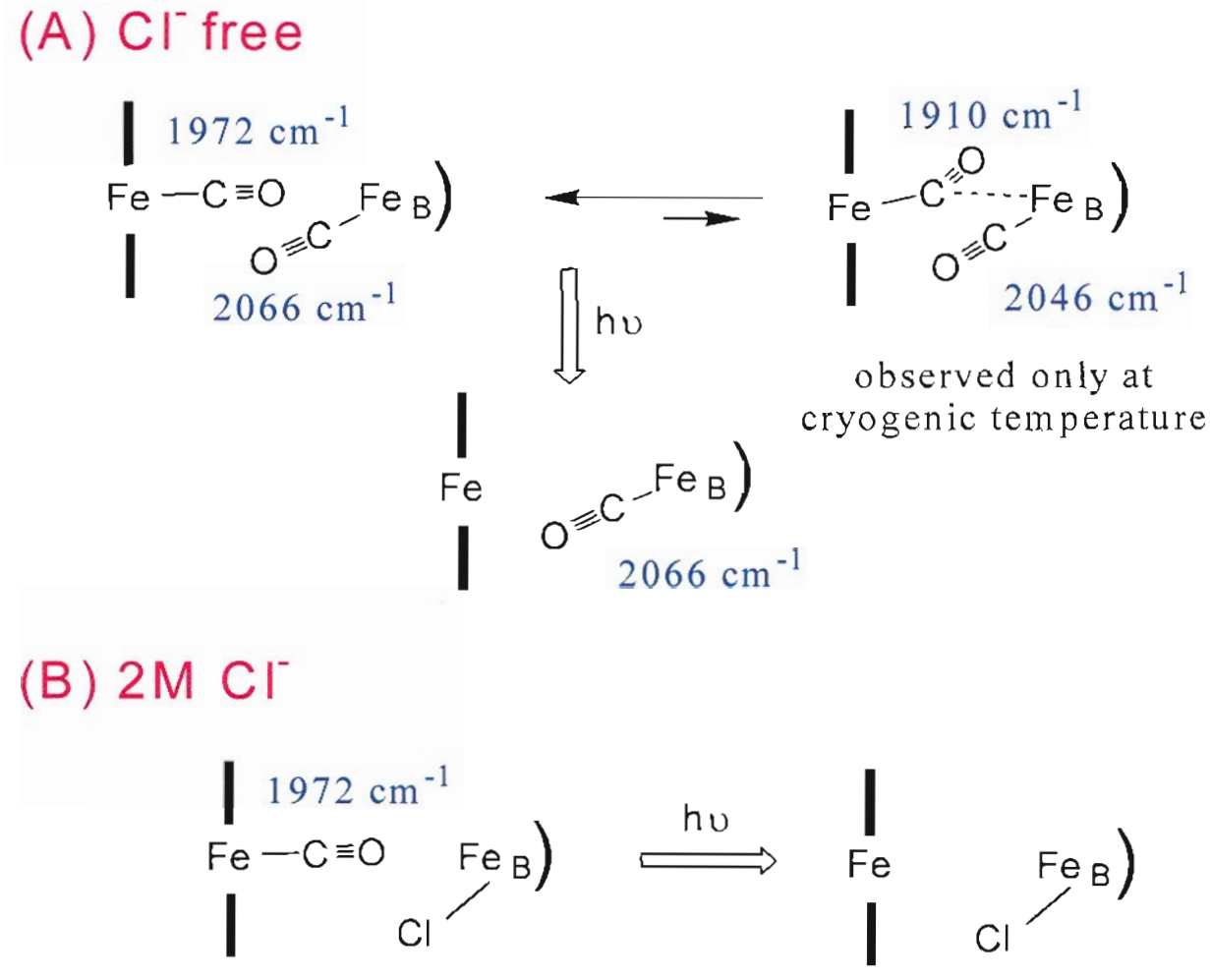

Fig. 5.9 Different configurations adopted by the CO ligands in qCu_ANOR. In the absence of excess chloride, CO binds to the non-heme iron Fe_B and the heme iron, and at 15 K the heme carbonyl adopt a semi-bridging configuration which perturbs the stretching frequency of the Fe_BCO. In presence of Cl^-, Fe_B becomes inactive for CO binding.

CHAPTER 6

CHARACTERIZATION OF INTERMEDIATE SPECIES USING MICROSECOND FREEZE-HYPERQUENCHING (MHQ)*

6.1 Rapid Freeze Quench Techniques

RR spectroscopy represents a unique tool to investigate the structure of reaction intermediates in metalloenzymes. Compared to other spectroscopic methods, it presents the advantage of selectively detecting chromophoric intermediates via resonance enhancement in ligand-to-metal or metal-to-ligand charge transfer, or $\pi \rightarrow \pi^*$ electronic transitions, and it provides direct information on speciation and chemical-bonding properties. Combining RR spectroscopy with rapid freeze quench (RFQ) techniques, where a reaction mixture is quenched at low temperature, can provide submolecular information on trapped reaction intermediates and help mapping the reaction coordinates.

In 1998, the combination of RFQ techniques and RR spectroscopy were first used to characterize a peroxo diiron(III) reaction intermediate in a non-heme diiron enzyme [Moënne-Loccoz et al., 1998a]. This transient intermediate, identified as a bridging μ-1,2 peroxo diiron(III) species, was produced in a W48F/D84E-R2 variant protein from *E. coli* and an intermediate in a phenylalanine monooxygenase reaction

---

* Material in this chapter has been published in this or similar form in *J. Raman Spectrosc.* and is used here with permission of John Wiley and Sons, Ltd.

Lu, S., Wiertz, F. G. M., de Vries, S., and Moënne-Loccoz, P. (2005) Resonance Raman characterization of a high-spin six-coordinate iron(III) intermediate in the metmyoglobin -azido complex formation trapped by microsecond freeze-hyperquenching (MHQ). *J. Raman Spectrosc.* **36**, 359 – 362.

[Baldwin et al., 2001]. The characterization of this peroxo intermediate was quickly followed by analogous vibrational studies of intermediates in two other non-heme diiron-containing proteins, Δ^9D and ferritin [Broadwater et al., 1998; Moënne-Loccoz et al., 1999]. The μ-1,2 peroxo species of wild-type frog ferritin, which participates in the physiological ferroxidase activity of the protein, is significantly short-lived and requires rapid freeze-quenching within ~25 ms after mixing. In this work liquid ethane was used as a cryosolvent in the preparation of RFQ samples, and eliminated previous problems of isopentane interference [Moënne-Loccoz et al., 1999]. Additionally, in a case study that used the azide binding reaction to met-Mb, Hildebrandt and coworkers showed that ms-RFQ and RR spectroscopy could provide kinetic information [Oellerich et al., 2000].

Recently, a major improvement in RFQ methodology was reported by Cherpanov and de Vries [Cherpanov and de Vries, 2004]. This new technique is referred to as microsecond freeze-hyperquenching (MHQ) because it allows trapping of transient species less than 100 μs after sample mixing. Specifically, a mixing time of ~20 μs is achieved using a tangential mixing chamber with a volume of ~1 nL and high operating pressures and linear flow rates (up to 400 bar and 200 $m \cdot s^{-1}$). This recent improvement permits a shorter distance between the exit nozzle and the freezing medium and alleviates problems of sample dilution and Raman contributions from cryosolvent. The MHQ "snow" is scraped from the cold plate and collected under liquid nitrogen and packed in EPR tubes for RR investigation. The snow can also be resuspended in isopentane for UV-vis spectroscopic analysis.

In initial studies, Cherpanov and de Vries used the reaction of horse heart met-Mb with azide as a model system to validate MHQ, and determine the minimal sample aging time of their prototype [Cherpanov and de Vries, 2004]. These experiments not only confirmed the decreased freezing time achieved by this instrument, but the UV-vis analysis also suggested that an intermediate species might be trapped during these experiments. These samples give us an opportunity to confirm that these samples were amenable to RR spectroscopy and allowed us to bring further evidence in support

of the accumulation of an intermediate species in the course of azide binding to met-Mb. We found that RR spectra from early samples trapped within 95 μs after exposure to azide, displayed porphyrin modes indicative of a six-coordinate high-spin species distinct from that of met-Mb, or of met-Mb azido complex observed in MHQ samples with longer delay times. This first study illustrates the promise of coupling the MHQ techniques and RR spectroscopy.

6.2 Materials and Methods

Myoglobin from horse heart was purchased from Sigma-Aldrich (>90% purity) and stock solutions were prepared in double-distilled water to a concentration of 1.4 mM. Prior to use, the myoglobin stock solution was diluted with a 125 mM citrate buffer pH 5.2 at a 1:1 ratio. A 2 M stock solution of sodium azide was prepared in 125 mM citrate buffer at pH 5.2. The final concentrations after rapid-mixing were 1 M azide and 0.35 mM total myoglobin. The reaction of azide with met-Mb was performed at 10 °C. After spraying the reaction mixture on the rotating cold-plate, liquid nitrogen was carefully poured into the cylinder. The samples were scraped off the wall of the cylinder and collected in Greiner tubes with liquid nitrogen. The samples were packed in EPR tubes fitted with a polypropylene filter at the end. An aluminum funnel was mounted on the top of the EPR tube. After cooling the funnel, the samples in liquid nitrogen were poured into the funnel, and a cork was set on the top of the funnel to raise the pressure and facilitate the samples flow into the EPR tube. The samples were packed in the EPR tubes with a pre-cooled rod and the samples were stored in liquid nitrogen until used.

RR spectra were obtained in a backscattering geometry on samples kept at 90 K with a liquid nitrogen coldfinger [Loehr and Sanders-Loehr, 1993]. The 413-nm excitation from a Kr^+ laser (Coherent, Innova 302) was kept below 20 mW and data accumulation of a few minutes was sufficient to reach high signal-to-noise ratio. A Kaiser supernotch filter was used to attenuate the Rayleigh scattering, and the

backscattered light was analyzed with a McPherson 207 spectrograph equipped with a Princeton Instruments liquid nitrogen-cooled (LN-1100PB) CCD detector as described in earlier chapters.

6.3 Transient met-Mb-Azido Complex

The RR data obtained on the MHQ samples corroborate the existence of a trapped intermediate. Figure 6.1 shows RR spectra of MHQ samples containing 100% met-Mb (Fig. 6.1A), those trapped within 95 and 245 μs of reaction with azide (Fig. 6.1B and 6.1C, respectively), and 100% of met-Mb azido complex (Fig. 6.1D). The two controls (i.e., starting material and end product) were sprayed and frozen under conditions identical to those used for the reaction mixtures. As reported previously [Oellerich et al., 2000], RR spectrum of met-Mb collected at 90 K displays skeletal porphyrin modes indicative of a 6-coordinate HS/LS mixture. Analogous modes in the azido complex spectrum correspond to a pure six-coordinate low-spin species. For instance, the ν_4 band is observed at 1372 cm^{-1} in met-Mb and is composed of a high-spin component at 1370 and a low-spin component at 1375 cm^{-1} whereas the met-Mb azido complex presents a single ν_4 component at 1376 cm^{-1}. Similarly, the ν_3 band is observed at 1483 cm^{-1} in met-Mb and at 1510 cm^{-1} in the met-Mb azido complex. Using the same experimental conditions to record RR spectra of diluted solution of met-Mb and its azido complex [Song and Asher, 1991], we determined that the same peak intensities were observed in the ν_4 region for both samples, and thus, RR spectra of the MHQ samples were normalized with the ν_4 peak intensity. The RR spectrum of the 245-μs MHQ sample (Fig. 6.1C) can be recomposed as ~40% met-Mb and ~60% azido complex, leaving a residual RR trace that represents less than 3% of the raw data (Fig. 6.2C'). In contrast, the spectrum of the MHQ sample at 95 μs (Fig. 6.1B) cannot be recomposed as a combination of the two control spectra. Indeed, subtracting more than ~60% met-Mb or more than ~20% of the azido complex of met-Mb starts generating negative features inconsistent with RR spectroscopy. Thus, the spectrum of

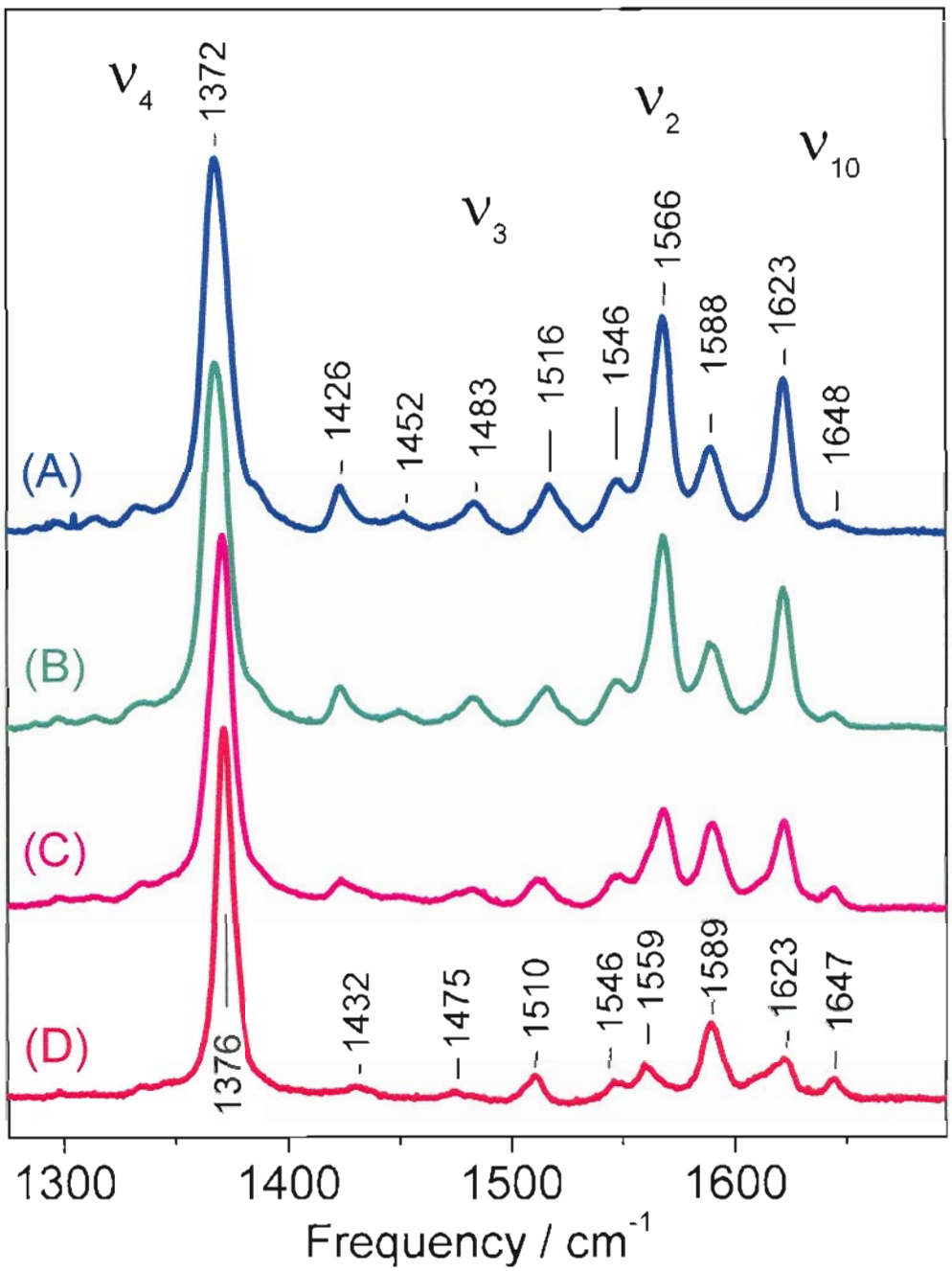

Fig. 6.1 High-frequency RR spectra of met-Mb (A), 95 μs-MHQ (B) and 245 μs-MHQ samples (C) after mixing of met-Mb with azide, and of met-Mb pre-incubated with azide (D).

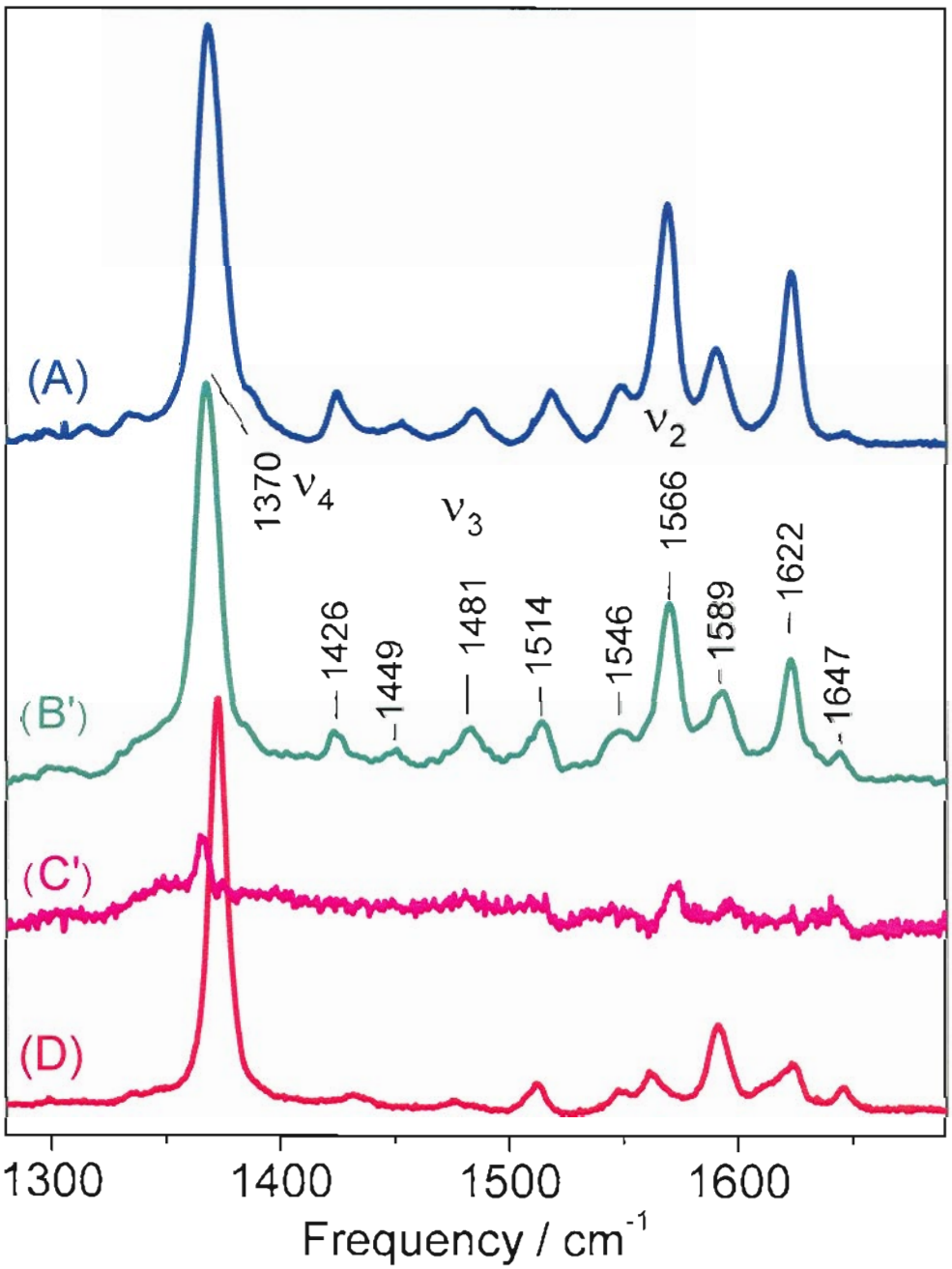

Fig. 6.2 Trace B′ and C′ represent the residual spectra of the 95 μs-MHQ (B′) and 245 μs-MHQ samples (C′) after maximal subtraction of contribution from the starting material (A) and the end-product (D). Traces B′ and C′ were multiplied by 4 to allow easy comparison with those of met-Mb (A), and met-Mb pre-incubated with azide (D).

the μs-RFQ sample at 95 μs reveals the presence of an intermediate species that accumulates to at least 20% (Fig. 6.2B′).

6.4 Discussion

The intermediate spectra of Figure 6.2B′ are consistent with a six-coordinate high-spin heme species with ν_4, ν_3, and ν_2 modes at 1370, 1481, and 1566 cm^{-1}, respectively. As for met-Mb and the azido complex, a distinct low-spin ν_{10} contribution at 1647 cm^{-1} reveals a low-spin component at this temperature and suggests that the 6-coordinate intermediate may exist as a HS/LS equilibrium. We can conclude that a nascent azido complex $[Mb \bullet N_3]^*$ distinct from the resting azido complex was formed during azido-Mb complex formation (Equation 6.1):

$$\text{met-Mb} + N_3^- \rightarrow [Mb \bullet N_3]^*_{t1/2 \sim 60\ \mu s} \rightarrow \text{Mb-}N_3 \quad \text{(Eq. 6.1)}$$

However, it remains to be determined whether the azido group is already coordinating the iron(III) but the ligand field splitting is smaller compared to that of the resting azido complex, or if azide is not yet coordinating the iron but perturbs interactions between the iron-aqua ligand and its distal-pocket environment. Investigating the spectral windows where iron-azide stretches, $\nu(Fe\text{-}N_3)$, and asymmetric intra-azide stretches, $\nu_{as}(NNN)$, may distinguish between these alternative interpretations. Regardless of the outcome of these future experiments, the work carried out so far demonstrates the feasibility and potential of this new methodology. In the next chapter we discuss how the combination of RR and MHQ techniques will be essential to the understanding of the catalytic cycle of NO reductases.

CHAPTER 7
CONCLUSIONS AND FUTURE DIRECTIONS

7.1 Peroxo Intermediates in Wild-Type R2 and Variant Proteins

To investigate the possible involvement of a bridging peroxo species during the O_2 activation of wt-R2, we have characterized by UV-vis absorption, EPR, RR, and FTIR spectroscopies the iron-nitrosyl species that form at the diiron sites of wt-R2, D84E-R2, and W48F/D84E-R2. In all three proteins, both irons bind one NO molecule to form a spin-coupled $\{FeNO\}^7$ dimer where both Fe-N-O units share a common vibrational signature. These results demonstrate that all three proteins accommodate fully symmetric $[\{FeNO\}^7]_2$ species with two identical Fe-N-O units. By analogy, the behavior of these R2 proteins toward NO suggests that binding of O_2 will occur in a symmetric configuration. The symmetry of the μ-1,2-peroxo intermediate observed in W48F/D84E-R2 is preserved in the structure of the NO adducts, and the formation of a similar $[\{FeNO\}^7]_2$ cluster in R2-wt supports the formation of a similar symmetric peroxodiiron(III) species in the O_2 reaction of wt-R2. While the μ-1,2-bridging peroxo species accumulate in the variant protein before leading to the hydroxylation of a nearby phenylalanine side chain, in the wt protein, the decay rate of the peroxo species is associated with a one electron transfer from the nearby tryptophan W48 which prevents the detection of the peroxo species [Lu et al., 2004b].

7.2 O_2 Activation Processes in MMOH

The azido complex formed in oxidized MMOH from *Methylococcus capsulatus* (Bath) was investigated with RR and FTIR techniques. The vibrational data from FTIR

are assigned to an azido complex bound terminally to one iron(III) at the diiron center. When the azido complex is illuminated at 15 K, a new ν_{as}(NNN) is observed which is assigned to a photodissociated HN_3 within the substrate pocket. From the FTIR data, we propose a model where an aqua ligand engages a hydrogen bond interaction with the 1N atom of the azido group and acts as at a proton donor during the photolysis process. The binding characteristics of the azido complex suggest that the peroxo complex formed in the course of O_2-activation in MMOH might be asymmetrically bound. Interestingly, an asymmetric η^2:η^1 bridging peroxo structure stabilized by a hydrogen bond interaction with an aqua ligand has been proposed on the basis of theoretical calculations. The proton transfer observed with the azido complex at 15 K suggests that the proton transfer might also take place during the O_2-activation process and influence the decay of H_{peroxo} and the structure of compound Q. In view of these results, and as an alternative to the diferryl bis-μ-oxo diamond core structure usual proposed for intermediate Q, we propose a asymmetric catalytic route where the two Fe(IV) of compound Q present different terminal oxo ligands and one bridging hydroxo [Lu et al., 2005a].

7.3 Reaction Intermediate in NO Reductase

CO complexes formed in reduced NO reductase from *Bacillus azotoformans* were investigated with RR and FTIR techniques. These experiments reveal the concomitant binding of two CO molecules to diiron(II) sites, a heme-CO complex, and a non-heme Fe_BCO complex. At cryogenic temperatures, the heme-CO complex can adopt a semi-bridging configuration with Fe_B. Our FTIR experiments strongly support a mechanistic model where two NO molecules can bind at the active site to form a $[\{FeNO\}^7]_2$ unit that promotes N-N bond formation. We also showed that chloride interferes with the binding of CO. Specifically, the presence of excess chloride inhibits CO binding at Fe_B and precludes the heme-CO from adopting a semi-bridging geometry. The FTIR data of qCu_ANOR-CO in presence of excess chloride are virtually

identical to those of cNOR, where binding of CO at the Fe_B site is not observed [Lu et al., 2004a].

7.4 Rapid-Freeze-Quench Intermediates in Metalloproteins

Recently, a newly developed instrumentation allowed us to trap transient species within less than 100 μs after mixing an exogenous ligand with a metalloprotein, thus making previously uncharacterized intermediates available for spectroscopic studies. An RR analysis of met-Mb with azide established that within 100-μs aging time an intermediate was trapped before formation of the end-product met-Mb-azido complex [Lu et al., 2005b]. Using this approach, we will be able to characterize MHQ samples collected during the reaction of fully-reduced NORs with NO, to define the catalytic mechanism of denitrifying NORs. A recent study has shown that NO and fully-reduced cNOR react in a sub-millisecond time scale, as evidenced by the appearance of new EPR signals within 0.5 ms after mixing [Kumita et al., 2004], but a RR characterization of such samples is still lacking.

7.5 Future Directions

Catalytic Mechanism Studies of NO Reductases

The work described in this thesis shows that the catalytic mechanism of denitrifying NORs can be characterized by a combination of the MHQ technique and RR spectroscopy. On the basis of these RR spectra, the coordination state of the heme *b* nitrosyl complex can be defined. The measurement of ν(Fe-NO) and ν(N-O), using isotopic labeling, will further confirm the coordination number of the heme iron. ν(N-O) and ν(Fe-NO) in NOR intermediates will be compared to the frequencies observed in non-reactive heme $\{FeNO\}^7$ species characterized in hemoproteins. If as suggested by the EPR experiment of Kumita et al. [Kumita et al., 2004] a non-heme iron-nitrosyl is also formed, FTIR experiments will be conducted to confirm the presence of this

species and determine the source of the reactivity of the $[\{FeNO\}^7]_2$ intermediate in NOR by comparing its vibrational signature with that of the stable $[\{FeNO\}^7]_2$ we characterized in the R2 proteins [Lu et al., 2004b; Lu et al., 2005b; Brown et al., 1995; Richter-Addo, 2002].

Examine Reaction Mechanisms of NO Reductase in Native Membrane Environment

Our experiments with the CO complexes of NORs demonstrate that conclusions reached with solublized proteins must be tested and complemented with studies of membrane fragments. Pre-steady state kinetics should be investigated in membrane fragments from *P. denitrificans* and *B. azotoformans*, to determine whether native membrane environments yield more homogeneous kinetics than that observed with solublized proteins. Such studies may ultimately provide better opportunities to detect and characterize reaction intermediates in the catalytic cycle of bacterial NORs.

Detoxifying NO Reductases

Another group of diiron proteins with NO reductase activity is comprised of the large family of soluble flavoprotein A (FprA) [Wasserfallen et al., 1998; Gardner et al., 2002b]. The active site of FprA contains a non-heme diiron cluster with two bridging ligands: a bidentate carboxylate and a solvent molecule (Fig. 7.1). With a Fe–Fe distance of 3.4 Å [Silaghi-Dumitrescu et al., 2005], this diiron cluster is reminiscent of O_2-activating diiron proteins such as MMOH and the protein R2 of RNR; however, FprAs show no amino acid sequence homology with other diiron proteins [Gomes et al., 2000; Gomes et al., 2002]. In FprA, each iron contains two histidine ligands and an empty coordination site that faces the other, such that NO could bind to form an $[\{FeNO\}^7]_2$ intermediate during catalysis [Silaghi-Dumitrescu et al., 2005]. If such species form in the catalytic turnover of FprA, we will be able to define their vibrational signatures and compare them with those we recently characterized at the non-heme diiron site of the R2 protein of RNR. Such comparisons will help determine the structural parameters that lead to catalytic efficiency.

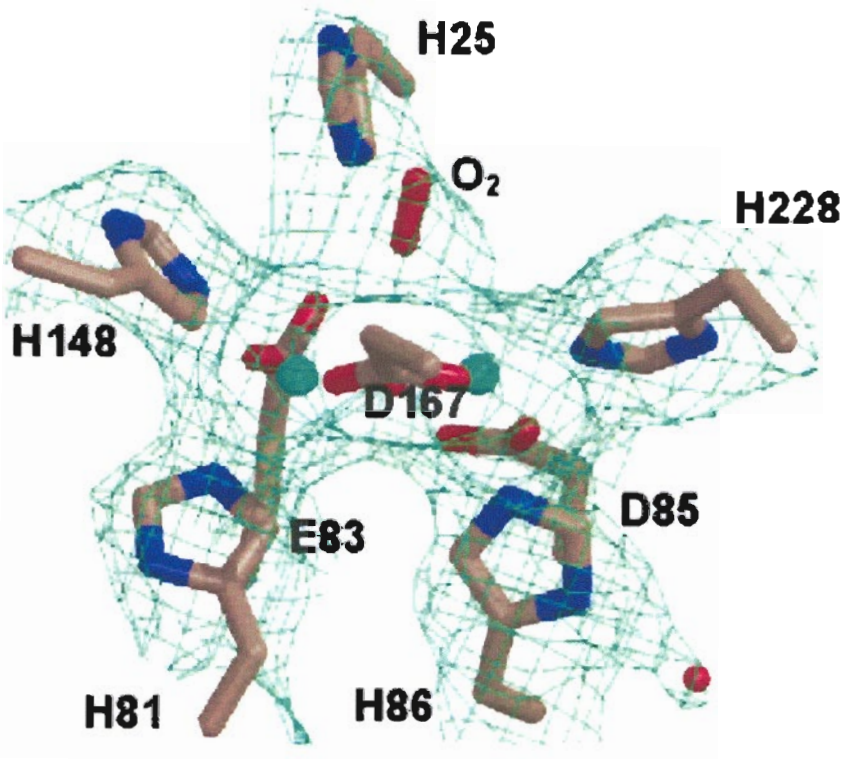

Fig. 7.1 Crystal structure of the diiron site in as-isolated *M. thermoacetica* FprA (PDB accession code 1YCF).

Originally published as Fig. 4 in:

Silaghi-Dumitrescu, R., Kurtz, D.M., Jr., Ljungdahl, L.G., and Lanzilotta, W.N. (2005) X-ray crystal structures of *Moorella thermoacetica* FprA. Novel diiron site structure and mechanistic insights into a scavenging nitric oxide reductase. *Biochemistry*, **44**, 6492-6501.

LITERATURE CITED

Aberg, A., Nordlund, P., and Eklund, H. (1993) Unusual clustering of carboxyl side chains in the core of iron-free ribonucleotide reductase. *Nature* **361**, 276-278.

Ai, J., Broadwater, J. A., Loehr, T. M., Sanders-Loehr, J., and Fox, B. G. (1997) Azide adducts of stearoyl-ACP desaturase: a model for μ-1,2 bridging by dioxygen in the binuclear iron active site. *J. Biol. Inorg. Chem.* **2**, 37-45.

Alben, J. O., Moh, P. P., Fiamingo, F. G., and Altschuld, R. A. (1981) Cytochrome oxidase (a_3) heme and copper observed by low-temperature Fourier transform infrared spectroscopy of the CO complex. *Proc. Natl. Acad. Sci. U. S. A.* **78**, 234-237.

Andersson, K. K., and Graslund, A. (1995) Diiron-Oxygen Proteins. *Adv. Inorg. Chem.* **43**, 359-408.

Andersson, M. E., Hogbom, M., Rinaldo-Matthis, A., Andersson, K. K., Sjöberg, B. M., and Nordlund, P. (1999) The crystal structure of an azide complex of the diferrous R2 subunit of ribonucleotide reductase displays a novel carboxylate shift with important mechanistic implications for diiron-catalyzed oxygen activation. *J. Am. Chem. Soc.* **121**, 2346-2352.

Ansari, A., Berendzen, J., Braunstein, D., Cowen, B. R., Frauenfelder, H., Hong, M. K., Iben, I. E., Johnson, J. B., Ormos, P., Sauke, T. B., Scholl, R., Schulte, A., Steinbach, P. J., Vittitow, J., and Young, R. D. (1987) Rebinding and relaxation in the myoglobin pocket. *Biophys. Chem.* **26**, 337-355.

Arciero, D. M., Orville, A. M., and Lipscomb, J. D. (1985) [^{17}O]Water and nitric oxide binding by protocatechuate 4,5-dioxygenase and catechol 2,3-dioxygenase. Evidence for binding of exogenous ligands to the active site Fe^{2+} of extradiol dioxygenases. *J. Biol. Chem.* **260**, 14035-14044.

Arciero, D. M., and Lipscomb, J. D. (1986) Binding of ^{17}O-labeled substrate and inhibitors to protocatechuate 4,5- dioxygenase-nitrosyl complex. Evidence for direct substrate binding to the active site Fe^{2+} of extradiol dioxygenases. *J. Biol. Chem.* **261**, 2170-2178.

Atkin, C. L., Thelander, L., Reichard, P., and Lang, G. (1973) Iron and free radical in ribonucleotide reductase. Exchange of iron and Mössbauer spectroscopy of the protein R2 subunit of the *Escherichia coli* enzyme. *J. Biol. Chem.* **248**, 7464-7472.

Bagley, K. A., Vangarderen, C. J., Chen, M., Duin, E. C., Albracht, S. P. J., and Woodruff, W. H. (1994) Infrared studies on the interaction of carbon monoxide with divalent nickel in hydrogenase from Chromatium vinosum. *Biochemistry* **33**, 9229-9236.

Baldwin, M. J., Ross, P. K., Pate, J. E., Tyeklár, Z., Karlin, K. D., and Solomon, E. I. (1991) Spectroscopic and theoretical-studies of an end-on peroxide-bridged coupled binuclear copper(II) model complex of relevance to the active-sites in hemocyanin and tyrosinase. *J. Am. Chem. Soc.* **113**, 8671-8679.

Baldwin, J., Krebs, C., Ley, B. A., Edmondson, D. E., Huyhn, B. H., and Bollinger, J. M., Jr. (2000) Mechanism of rapid electron transfer during oxygen activation in the R2 subunit of *Escherichia coli* ribonucleotide reductase. 1. Evidence for a transient tryptophan radical. *J Am Chem Soc* **122**, 12195-12206.

Baldwin, J., Voegtli, W. C., Khidekel, N., Moënne-Loccoz, P., Krebs, C., Pereira, A. S., Ley, B. A., Huynh, B. H., Loehr, T. M., and Riggs-Gelasco, P. J. (2001) Rational reprogramming of the R2 subunit of *Escherichia coli.* ribonucleotide reductase into a self-hydroxylating monooxygenase. *J. Am. Chem. Soc.* **123**, 7017-7030.

Baldwin, J., Krebs, C., Saleh, L., Stelling, M., Huynh, B. H., Bollinger, J. M., Jr., and Riggs-Gelasco, P. (2003) Structural characterization of the peroxodiiron(III) intermediate generated during oxygen activation by the W48A/D84E variant of ribonucleotide reductase protein R2 from *Escherichia coli. Biochemistry* **42**, 13269-13279.

Bollinger, J. M., Jr., Tong, W. H., Ravi, N., Huynh, B. H., Edmondson, D. E., and Stubbe, J. (1994a) Mechanism of assembly of the tyrosyl radical-diiron(III) cofactor of *Escherichia coli* ribonucleotide reductase: 3. Kinetics of the limiting Fe^{2+} reaction by optical, EPR, and Mössbauer spectroscopies. *J. Am. Chem. Soc.* **116**, 8024-8032.

Bollinger, J. M., Jr., Tong, W. H., Ravi, N., Huynh, B. H., Edmondson, D. E., and Stubbe, J. (1994b) Mechanism of assembly of the tyrosyl radical-diiron(III) cofactor of *Escherichia coli* ribonucleotide reductase: 2. Kinetics of the excess Fe^{2+} reaction by optical, EPR, and Mössbauer spectroscopies. *J. Am. Chem. Soc.* **116**, 8015-8023.

Bollinger, J. M., Jr., Chen, S., Parkin, S. E., Mangravite, L. M., Ley, B. A., Edmondson, D. E., and Huynh, B. H. (1997) Differential iron(II) affinity of the sites of the diiron cluster in protein R2 of *Escherichia coli.* ribonucleotide reductase: tracking the individual sites through the O_2 activation. *J. Am. Chem. Soc.* **119**, 5976-5977.

Bollinger, J. M., Jr., Krebs, C., Vicol, A., Chen, S., Ley, B. A., Edmondson, D. E., and Huynh, B. H. (1998) Engineering the diiron site of *Escherichia coli* ribonucleotide reductase protein R2 to accumulate an intermediate similar to H_{peroxo}, the putative peroxodiiron(III) complex from the methane monooxygenase catalytic cycle. *J. Am. Chem. Soc.* **120**, 1094-1095.

Broadwater, J. A., Ai, J., Loehr, T. M., Sanders-Loehr, J., and Fox, B. G. (1998) Peroxodiferric Intermediate of Stearoyl-Acyl Carrier Protein Δ^9 Desaturase: Oxidase Reactivity during Single Turnover and Implications for the Mechanism of Desaturation *Biochemistry* **37**, 14664-14671

Broadwater, J. A., Achim, C., Münck, E., and Fox, B.G. (1999) Mössbauer studies of the formation and reactivity of a quasi-stable peroxo intermediate of stearoyl-acyl carrier protein Δ^9-desaturase. *Biochemistry* **38**, 12197-12204.

Broderick, J. B., and Coucouvanis, D. (2003) Bioinorganic chemistry. *Curr. Opin. Chem. Biol.* **7**, 157-159.

Brown, C. A., Pavlosky, M. A., Westre, T. E., Zhang, Y., Hedman, B., Hodgson, K. O., and Solomon, E. I. (1995) Spectroscopic and theoretical description of the electronic structure of S = 3/2 iron-nitrosyl complexes and their relation to O_2 activation by non-heme iron enzyme active sites. *J. Am. Chem. Soc.* **117**, 715-732.

Brunold, T. C., Tamura, N., Kitajima, N., Moro-Oka, Y., and Solomon, E. I. (1998) Spectroscopic study of $[Fe_2(O_2)(OBz)_2\{HB(pz')_3\}_2]$: nature of the μ-1,2 peroxide-Fe(III) bond and its possible relevance to O_2 activation by non-heme iron enzymes. *J. Am. Chem. Soc.* **120**, 5674-5690.

Brunori, M. (2001) Nitric oxide, cytochrome *c* oxidase and myoglobin. *Trends Biochem. Sci.* **26**, 21-23.

Burstyn, J. N., Roe, J. A., Miksztal, A. R., Shaevitz, B. A., Lang, G., and Valentine, J. S. (1988) Magnetic and spectroscopic characterization of an iron porphyrin peroxide complex. Peroxoferrioctaethylporphyrin(1-). *J. Am. Chem. Soc.* **110**, 1382-1388.

Castresana, J., Lubben, M., Saraste, M., and Higgins, D. G. (1994) Evolution of cytochrome oxidase, an enzyme older than atmospheric oxygen. *EMBO J.* **13**, 2516-2525.

Chang, M. C. Y., Yee, C. S., Nocera, D. G., and Stubbe, J. (2004) Site-specific replacement of a conserved tyrosine in ribonucleotide reductase with an aniline amino acid: a mechanistic probe for a redox-active tyrosine. *J. Am. Chem. Soc.* **126**, 16702-16703.

Cheesman, M. R., Zumft, W. G., and Thomson, A. J. (1998) The MCD and EPR of the heme centers of nitric oxide reductase from *Pseudomonas stutzeri*: evidence that the enzyme is structurally related to the heme-copper oxidases. *Biochemistry* **37**, 3994-4000.

Chen, V. J., Orville, A. M., Harpel, M. R., Frolik, C. A., Surerus, K. K., Münck, E., and Lipscomb, J. D. (1989) Spectroscopic studies of isopenicillin N synthase. A mononuclear nonheme Fe^{2+} oxidase with metal coordination sites for small molecules and substrate. *J. Biol. Chem.* **264**, 21677-21681.

Cherpanov, A. V., and de Vries, S. (2004) Microsecond freeze-hyperquenching: development of a new ultrafast micro-mixing and sampling technology and application to enzyme catalysis. *Biochim. Biophys. Acta.* **1656**, 1-31.

Chiou, Y. M., and Que, L., Jr. (1995a) Models for α-Keto Acid-Dependent Non-heme Iron Enzymes: Structures and Reactivity of $[Fe^{II}(L)(O_2CCOPh)](ClO_4)$ Complexes. *J. Am. Chem. Soc.* **117**, 3999-4013.

Chiou, Y. M., and Que, L., Jr. (1995b) Model studies of α-keto acid-dependent nonheme iron enzymes: nitric oxide adducts of $[Fe^{II}(L)(O_2CCOPh)](ClO_4)$ complexes. *Inorg. Chem.* **34**, 3270-3278.

Clay, M. D., Cosper, C. A., Jenney, F. E. J., Adams, M. W., and Johnson, M. K. (2003) Nitric oxide binding at the mononuclear active site of reduced *Pyrococcus furiosus* superoxide reductase. *Proc. Natl. Acad. Sci. U. S. A.* **100**, 3796-3801.

Coufal, D. E., Tavares, P., Pereira, A. S., Hyunh, B. H., and Lippard, S. J. (1999) Reactions of nitric oxide with the reduced non-heme diiron center of the soluble methane monooxygenase hydroxylase. *Biochemistry* **38**, 4504-4513.

Covès, J., Laulhère, J. P., and Fontecave, M. (1997) The role of exogenous iron in the activation of ribonucleotide reductase from *Escherichia coli*. *J. Biol. Inorg. Chem.* **2**, 418-426.

Coyle, C. M., Vogel, K. M., Rush, T. S., Kozlowski, P. M., Williams, R., Spiro, T. G., Dou, Y., Ikeda-Saito, M., Olson, J. S., and Zgierski, M. Z. (2003) FeNO structure in distal pocket mutants of myoglobin based on resonance Raman spectroscopy. *Biochemistry* **42**, 4896-4903.

Cramm, R., Pohlmann, A., and Friedrich, B. (1999) Purification and characterization of the single-component nitric oxide reductase from *Ralstonia eutropha* H16. *FEBS Lett.* **460**, 6-10.

Deeth, R. J., and Dalton, H. (1998) Methane activation by methane monooxygenase: free radicals, Fe-C bonding, substrate dependent pathways and the role of the regulatory protein. *J. Biol. Inorg. Chem.* **3**, 302-306.

Deinum, G., Stone, J. R., Babcock, G. T., and Marletta, M. A. (1996) Binding of nitric oxide and carbon monoxide to soluble guanylate cyclase as observed with resonance Raman spectroscopy. *Biochemistry* **35**, 1540-1547.

de Vries, D., and Schroder, I. (2002) Comparison between the nitric oxide reductase family and its aerobic relatives, the cytochrome oxidases. *Biochem. Soc. Trans.* **30**, 662-667.

de Vries, S., Strampraad, M. J., Lu, S., Moënne-Loccoz, P., and Schroder, I. (2003) Purification and characterization of the MQH2:NO oxidoreductase from the hyperthermophilic archaeon Pyrobaculum aerophilum. *J. Biol. Chem.* **278**, 35861-35868.

Drapier, J. C., Pellat, C., and Henry, Y. (1991) Generation of EPR-detectable nitrosyl-iron complexes in tumor target cells cocultured with activated macrophages. *J. Biol. Chem.* **266**, 10162-10167.

Dunietz, B. D., Beachy, M. D., Cao, Y., Whittington, D. A., Lippard, S. J., and Friesner, R. A. (2000) Large scale ab initio quantum chemical calculation of the intermediates in the soluble methane monooxygenase catalytic cycle. *J. Am. Chem. Soc.* **122**, 2828-2839.

Einarsdottir, O., Killough, P. M., Fee, J. A., and Woodruff, W. H. (1989) An infrared study of the binding and photodissociation of carbon monoxide in cytochrome *ba3* from *Thermus thermophilus*. *J. Biol. Chem.* **264**, 2405-2408.

Enemark, J. H., and Feltham, R. D. (1974) Principles of structure, bonding, and reactivity for metal nitrosyl complexes. *Coord. Chem. Rev.* **13**, 339-406.

Fabian, M., Skultety, L., Brunel, C., and Palmer, G. (2001) Cyanide stimulated dissociation of chloride from the catalytic center of oxidized cytochrome *c* oxidase. *Biochemistry*, **40**, 6061-6069.

Feig, A. L., and Lippard, S. J. (1994) Reactions of non-heme iron(II) centers with dioxygen in biology and chemistry. *Chem. Rev.* **94**, 759-805.

Feig, A. L., Bautista, M. T., and Lippard, S. J. (1996) A carboxylate-bridged non-heme diiron dinitrosyl complex. *Inorg. Chem.* **35**, 6892-6898.

Ferguson-Miller, S., and Babcock, G.T. (1996) Heme/copper terminal oxidases. *Chem. Rev.* **96**, 2889-2908.

Galli, C., Atta, M., Andersson, K. K., Graslund, A., and Brudvig, G. W. (1995) Variations of the diferric exchange coupling in the R2-subunit of ribonucleotide reductase from 4 species as determined by saturation-recovery EPR spectroscopy. *J. Am. Chem. Soc.* **117**, 740-746.

Gardner, A. M., and Gardner, P. R. (2002a) Flavohemoglobin detoxifies nitric oxide in aerobic, but not anaerobic, *Escherichia coli*. Evidence for a novel inducible anaerobic nitric oxide-scavenging activity. *J. Biol. Chem.* **277**, 8166-8171.

Gardner, A. M., Helmick, R. A., and Gardner, P. R. (2002b) Flavorubredoxin, an inducible catalyst for nitric oxide reduction and detoxification in *Escherichia coli*. *J. Biol. Chem.* **277**, 8172-8177.

Gennis, R. B. (1998) Multiple proton-conducting pathways in cytochrome oxidase and a proposed role for the active-site tyrosine. *Biochim. Biophys. Acta.* **1365**, 241-248.

George, S. D., Metz, M., Szilagyi, R. K., Wang, H., Cramer, S. P., Lu, Y., Tolman, W. B., Hedman, B., Hodgson, K. O., and Solomon, E. I. (2001) A quantitative description of the ground-state wave function of Cu_A by X-ray absorption spectroscopy: comparison to plastocyanin and relevance to electron transfer. *J. Am. Chem. Soc.* **123**, 5757-5767.

Gherman, B. F., Baik, M. H., Lippard, S. J., and Friesner, R. A. (2004) Dioxygen activation in methane monooxygenase: a theoretical study. *J. Am. Chem. Soc.* **126**, 2978-2990.

Ghiladi, R. A., Ju, T. D., Lee, D. H., Moënne-Loccoz, P., Kaderli, S., Neuhold, Y. M., Zuberbuhler, A. D., Woods, A. S., Cotter, R. J., and Karlin, K. D. (1999) Formation and characterization of a high-spin heme-copper dioxygen (peroxo) complex. *J. Am. Chem. Soc.* **121**, 9885-9886.

Ghiladi, R. A., Hatwell, K. R., Karlin, K. D., Huang, H., Moënne-Loccoz, P., Krebs, C., Huynh, B. H., Marzilli, L. A., Cotter, R. J., Kaderli, S., and Zuberbühler, A. D. (2001) Dioxygen reactivity of mononuclear heme and copper components yielding a high-spin heme-peroxo-Cu complex. *J. Am. Chem. Soc.* **123**, 6183-6184.

Girsch, P., and de Vries, S. (1997) Purification and initial kinetic and spectroscopic characterization of NO reductase from *Paracoccus denitrificans*. *Biochim. Biophys. Acta.* **1318**, 202-216.

Giuffre, A., Stubauer, G., Sarti, P., Brunori, M., Zumft, W. G., Buse, G. and Soulimane, T. (1999) The heme-copper oxidases of *Thermus thermophilus* catalyze the reduction of nitric oxide: evolutionary implications. *Proc. Natl. Acad. Sci. U. S. A.* **96**, 14718-14723.

Gomes, C. M., Vicente, J. B., Wasserfallen, A., and Teixeira, M. (2000) Spectroscopic studies and characterization of a novel electron-transfer chain from *Escherichia coli.* involving a flavorubredoxin and its flavoprotein reductase partner. *Biochemistry*, **39**, 16230-16237.

Gomes, C.M., Giuffre, A., Forte, E., Vicente, J. B., Saraiva, L. M., Brunori, M., and Teixeira, M. (2002) A novel type of nitric-oxide reductase. *Escherichia coli.* flavorubredoxin. *J. Biol. Chem.*, **277**, 25273-25276.

Goretski, J., Zafiriou, O. C., and Hollocher, T. C. (1990) Steady-state nitric oxide concentrations during denitrification. *J. Biol. Chem.* **265**, 11535-11538.

Gronberg, K. L. C., Roldan, M. D., Prior, L., Butland, G., Cheesman, M. R., Richardson, D. J., Spiro, S., Thomson, A. J., and Watmough, N. J. (1999) A low-redox potential heme in the dinuclear center of bacterial nitric oxide reductase: implications for the evolution of energy-conserving heme-copper oxidases. *Biochemistry* **38**, 13780-13786.

Hanson, R. S., and Hanson, T. E. (1996) Methanotrophic bacteria. *Microbiol. Rev.* **60**, 439-471.

Haskin, C. J., Ravi, N., Lynch, J. B., Münck, E., and Que, L., Jr. (1995) Reaction of NO with the reduced R2 protein of ribonucleotide reductase from *Escherichia coli. Biochemistry* **34**, 11090-11098.

Heiss, B., Frunzke, K., and Zumft, W. G. (1989) Formation of the N-N bond from nitric oxide by a membrane-bound cytochrome *bc* complex of nitrate-respiring (denitrifying) *Pseudomonas stutzeri. J. Bacteriol.* **171**, 3288-3297.

Hendriks, J., Warne, A., Gohlke, U., Haltia, T., Ludovici, C., Lubben, M. and Saraste, M. (1998) The active site of the bacterial nitric oxide reductase is a dinuclear iron center. *Biochemistry* **37**, 13102-13109.

Hersleth, H. P., Dalhus, B., Gorbitz, C. H., and Andersson, K. K. (2002) An iron hydroxide moiety in the 1.35 Å resolution structure of hydrogen peroxide derived myoglobin compound II at pH 5.2. *J. Biol. Inorg. Chem.* **7**, 299-304.

Himo, F., and Siegbahn, P. E. M. (2003) Quantum chemical studies of radical-containing enzymes. *Chem. Rev.* **103**, 2421-2456.

Hogbom, M., Galander, M., Andersson, M., Kolberg, M., Hofbauer, W., Lassmann, G., Nordlund, P., and Lendzian, F. (2003) Displacement of the tyrosyl radical cofactor in ribonucleotide reductase obtained by single-crystal high-field EPR and 1.4-Å X-ray data. *Proc. Natl. Acad. Sci. U. S. A.* **100**, 3209-3214.

Holm, R. H., Kennepohl, P., and Solomon, E. I. (1996) Structural and functional aspects of metal sites in biology. *Chem. Rev.* **96**, 2239-2314.

Holm, R. H., and Solomon, E. I. (2004) Preface: biomimetic inorganic chemistry. *Chem. Rev.* **104**, 347-348.

Holmes, M. A., Le Trong, I., Turley, S., Sieker, L. C., and Stenkamp, R. E. (1991) Structures of deoxy and oxy hemerythrin at 2.0 Å resolution. *J. Mol. Biol.* **218**, 583-593.

Ito, N., Phillips, S. E., Stevens, C., Ogel, Z. B., McPherson, M. J., Keen, J. N., Yadav, K. D., and Knowles, P. F. (1991) Novel thioether bond revealed by a 1.7 Å crystal structure of galactose oxidase. *Nature* **350**, 87-89.

Iwata, S., Ostermeier, C., Ludwig, B., and Michel, H. (1995) Structure at 2.8 Å resolution of cytochrome *c* oxidase from *Paracoccus denitrificans*. *Nature* **376**, 660-669.

Jackson, T. A., Yikilmaz, E., Miller, A. F., and Brunold, T. C. (2003) Spectroscopic and computational study of a non-heme iron $\{Fe\text{-}NO\}^7$ system: exploring the geometric and electronic structures of the nitrosyl adduct of iron superoxide dismutase. *J. Am. Chem. Soc.* **125**, 8348-8363.

Ju, T. D., Woods, A. S., Cotter, R. J., Moënne-Loccoz, P., and Karlin, K. D. (2000) Dioxygen and nitric oxide reactivity of a reduced heme/non-heme diiron(II) complex $[(^5L)Fe^{II}\cdots Fe^{II}\text{—}Cl]^+$. Using a tethered tetraarylporphyrin for the development of an active site reactivity model for bacterial nitric oxide reductase. *Inorg. Chim. Acta.* **297**, 362-372.

Karlin, K. D., Kaderli, S., and Zuberbühler, A. D. (1997) Kinetics and thermodynamics of copper(I)/dioxygen interaction. *Acc. Chem. Res.* **30**, 139-147.

Karlsson, M., Sahlin, M., and Sjöberg, B. M. (1992) *Escherichia coli.* ribonucleotide reductase. Radical susceptibility to hydroxyurea is dependent on the regulatory state of the enzyme. *J. Biol. Chem.* **267**, 12622-12626.

Kharitonov, V. G., Sharma, V. S., Pilz, R. B., Magde, D., and Koesling, D. (1995) Basis of guanylate cyclase activation by carbon monoxide. *Proc. Natl. Acad. Sci. U. S. A.* **92**, 2568-2571.

Kim, E., Helton, M. E., Wasser, I. M., Karlin, K. D., Lu, S., Huang, H., Moënne-Loccoz, P., Incarvito, C. D., Rheingold, A. L., Honecker, M., Kaderli, S., and Zuberbuhler, A. D. (2003) Superoxo, μ-peroxo, and μ-oxo complexes from heme/O_2 and heme-Cu/O_2 reactivity: copper ligand influences in cytochrome *c* oxidase models. *Proc. Natl. Acad. Sci. U. S. A.* **100**, 3623-3628.

Kim, E., Chufan, E. E., Kamaraj, K., and Karlin, K. D. (2004) Synthetic models for heme-copper oxidases. *Chem. Rev.* **104**, 1077-1133.

Kopp, D. A., and Lippard, S. J. (2002) Soluble methane monooxygenase: activation of dioxygen and methane. *Curr. Opin. Chem. Biol.* **6**, 568-576.

Koutsoupakis, K., Stavrakis, S., Pinakoulaki, E., Soulimane, T, and Varotsis, C. (2002) Observation of the equilibrium Cu_B-CO complex and functional implications of the transient heme a_3 propionates in cytochrome ba_3-CO from *Thermus thermophilus*. Fourier transform infrared (FTIR) and time-resolved step-scan FTIR studies. *J. Biol. Chem.* **277**, 32860-32866.

Krebs, C., Chen, S., Baldwin, J., Ley, B. A., Patel, U., Edmondson, D. E., Huynh, B. H., and Bollinger, J. M., Jr. (2000) Mechanism of rapid electron transfer during oxygen activation in the R2 subunit of *Escherichia coli.* ribonucleotide reductase. 2. Evidence for and consequences of blocked electron transfer in the W48F variant. *J. Am. Chem. Soc.* **122**, 12207-12219.

Kumita, H., Matsuura, K., Hino, T., Takahashi, S., Hori, H., Fukumori, Y., Morishima, I., and Shiro, Y. (2004) NO reduction by nitric oxide reductase from denitrifying bacterium *Pseudomonas aeruginosa*: characterization of reaction intermediates that appear in the single turnover cycle. *J. Biol. Chem.* **279**, 55247-55254.

Kurtz, D. M., Jr. (1997) Structural similarity and functional diversity in diiron-oxo proteins. *J. Biol. Inorg. Chem.* **2**, 159-167.

Kurtz, D. M., Jr. (1999), Oxygen-carrying proteins: three solutions to a common problem. *Essays Biochem.* **34**, 85-100.

Lah, M. S., Dixon, M. M., Pattridge, K. A., Stallings, W. C., Fee, J. A., and Ludwig, M. L. (1995) Structure-function in *Escherichia coli.* iron superoxide dismutase: comparisons with the manganese enzyme from *Thermus thermophilus*. *Biochemistry* **34**, 1646-1660.

Lee, M., Arosio, P., Cozzi, A., and Chasteen, N. D. (1994) Identification of the EPR-active iron-nitrosyl complexes in mammalian ferritins. *Biochemistry* **33**, 3679-3687.

Lee, S. K, and Lipscomb, J. D. (1999) Oxygen activation catalyzed by methane monooxygenase hydroxylase component: proton delivery during the O-O bond cleavage steps. *Biochemistry* **38**, 4423-4432.

Lee, D., Pierce, B., Krebs, C., Hendrich, M. P., Huynh, B. H., and Lippard, S. J. (2002) Functional mimic of dioxygen-activating centers in non-heme diiron enzymes: mechanistic implications of paramagnetic intermediates in the reactions between diiron(II) complexes and dioxygen. *J. Am. Chem. Soc.* **124**, 3993-4007.

Li, P. M., Gelles, J., Chan, S. I., Sullivan, R. J., and Scott, R. A. (1987) Extended X-ray absorption fine structure of copper in Cu_A-depleted, p-(hydroxymercuri)benzoate-modified, and native cytochrome *c* oxidase. *Biochemistry*, **26**, 2091-2095.

Li, X. Y., and Spiro, T. G. (1988) Is bound carbonyl linear or bent in heme proteins? Evidence from resonance Raman and infrared spectroscopic data. *J. Am. Chem. Soc.* **110**, 6024-6033.

Li, W., and Palmer, G. (1993) Spectroscopic characterization of the interaction of azide and thiocyanate with the binuclear center of cytochrome oxidase: evidence for multiple ligand sites. *Biochemistry*, **32**, 1833-1843.

Liang, H., Zhang, C. X., Henson, M. J., Sommer, R. D., Hatwell, K. R., Kaderli, S., Zuberbühler, A. D., Rheingold, A. L., Solomon, E. I., and Karlin, K. D. (2002) Contrasting copper-dioxygen chemistry arising from alike tridentate alkyltriamine copper(I) complexes. *J. Am. Chem. Soc.* **124**, 4170-4171.

Lieberman R. L., and Rosenzweig A. C. (2005) Crystal structure of a membrane-bound metalloenzyme that catalyses the biological oxidation of methane. *Nature* **434**, 177-182.

Lindqvist, Y., Huang, W., Schneider, G., and Shanklin, J. (1996) Crystal structure of Δ^9 stearoyl-acyl carrier protein desaturase from castor seed and its relationship to other diiron proteins. *EMBO J.* **15**, 4081-4092.

Lippard, S. J., and Berg, J. M. (1994) Principles of bioinorganic chemistry. Mill Valley: University Science Books.

Lipscomb, J. D., and Que, L., Jr. (1998) MMO: P450 in wolf's clothing? *J. Biol. Inorg. Chem.* **3**, 331-336.

Liu, K. E., Wang, D., Huynh, B. H., Edmondson, D. E., Salifoglou, A., and Lippard, S. J. (1994) Spectroscopic detection of intermediates in the reaction of dioxygen with the reduced methane monooxygenase/hydroxylase from *Methylococcus capsulatus* (Bath) *J. Am. Chem. Soc.* **116**, 7465-7466.

Liu, K. E., Valentine, A. M., Wang, D., Huynh, B. H., Edmondson, D. E., Salifoglou, A., and Lippard, S. J. (1995a) Kinetic and spectroscopic characterization of intermediates and component interactions in reactions of methane monooxygenase from *Methylococcus capsulatus* (Bath) *J. Am. Chem. Soc.* **117**, 10174-10185.

Liu, K. E., Valentine, A. M., Qiu, D., Edmondson, D. E., Appelman, E. H., Spiro, T. G., and Lippard, S. J. (1995b) Characterization of a diiron(III) peroxo intermediate in the reaction cycle of methane monooxygenase hydroxylase from *Methylococcus capsulatus* (Bath). *J. Am. Chem. Soc.* **117**, 4997-4998.

Liu, Y., Nesheim, J. C., Lee, S. K., and Lipscomb, J. D. (1995c) Gating effects of component B on oxygen activation by the methane monooxygenase hydroxylase component. *J. Biol. Chem.* **270**, 24662-24665.

Liu, J. G., Naruta, Y., Tani, F., Chishiro, T., and Tachi, Y. (2004) Formation and spectroscopic characterization of the dioxygen adduct of a heme-Cu complex possessing a cross-linked tyrosine-histidine mimic: modeling the active site of cytochrome *c* oxidase. *Chem. Commun.* **2004**, 120-121.

Loehr, T. M., and Sanders-Loehr, J. (1993) Technique for obtaining resonance Raman spectra of metalloproteins. *Methods Enzymol.* **226**, 431-470.

Logan, D. T., Su, X. D., Aberg, A., Regnstrom, K., Hajdu, J., Eklund, H., and Nordlund, P. (1996) Crystal structure of reduced protein R2 of ribonucleotide reductase: the structural basis for oxygen activation at a dinuclear iron site. *Structure* **4**, 1053-1064.

Lu, S., Suharti, de Vries, S., and Moënne-Loccoz, P. (2004a) Two CO molecules can bind concomitantly at the diiron site of NO reductase from *Bacillus azotoformans*. *J. Am. Chem. Soc.* **126**, 15332-15333.

Lu, S., Libby, E., Saleh, L., Xing, G., Bollinger, J. M., Jr., and Moënne-Loccoz, P. (2004b) Characterization of NO adducts of the diiron center in protein R2 of *Escherichia coli.* ribonucleotide reductase and site-directed variants; implications for the O_2 activation mechanism. *J. Biol. Inorg. Chem.* **9**, 818-827.

Lu, S., Sazinsky, M. H., Whittaker, J. W., Lippard, S. J., and Moënne-Loccoz, P. (2005a) Fourier transform infrared characterization of the azido complex of methane

monooxygenase hydroxylase from *Methylococcus capsulatus* (Bath). *J. Am. Chem. Soc.* **127**, 4148-4149.

Lu, S., Wiertz, F. G. M., de Vries, S., and Moënne-Loccoz, P. (2005b) Resonance Raman characterization of a high-spin six-coordinate iron(III) intermediate in the metmyoglobin-azido complex formation trapped by microsecond freeze-hyperquenching (MHQ). *J. Raman Spectrosc.* **36**, 359-362.

Lynch, J. B., Juarez-Garcia, C., Münck, E., and Que, L., Jr. (1989) Mössbauer and EPR studies of the binuclear iron center in ribonucleotide reductase from *Escherichia coli*. A new iron-to-protein stoichiometry. *J. Biol. Chem.* **264**, 8091-8096.

MacMillan, F., Kannt, A., Behr, J., Prisner, T., and Michel, H. (1999) Direct evidence for a tyrosine radical in the reaction of cytochrome *c* oxidase with hydrogen peroxide. *Biochemistry* **38**, 9179-9184.

McDonald, C. C., Phillips, W. D., and Mower, H. F. (1965) An electron spin resonance study of some complexes of iron, nitric oxide, and anionic ligands. *J. Am. Chem. Soc.* **87**, 3319-3326.

Miller, M. A., Gobena, F. T., Kauffmann, K., Münck, E., Que, L., Jr., and Stankovich, M. T. (1999) Differing roles for the diiron clusters of ribonucleotide reductase from aerobically grown *Escherichia coli.* in the generation of the Y122 radical. *J. Am. Chem. Soc.* **121**, 1096-1097.

Mitchell, D. M., Muller, J. D., Gennis, R. B., and Nienhaus, G. U. (1996) FTIR study of conformational substrates in the CO adduct of cytochrome *c* oxidase from *Rhodobacter sphaeroides*. *Biochemistry* **35**, 16782-16788.

Mitchell, D. M., Wang, Y., Alben, J. O., and Shapleigh, J. P. (1998) Fourier transform infrared analysis of membranes of *Rhodobacter sphaeroides* 2.4.3 grown under microaerobic and denitrifying conditions. *Biochim. Biophys. Acta.* **1409**, 99-105.

Moënne-Loccoz, P., Baldwin, J., Ley, B. A., Loehr, T. M., and Bollinger, J. M., Jr. (1998a) O_2 activation by non-heme diiron proteins: identification of a symmetric μ-1,2-peroxide in a mutant of ribonucleotide reductase. *Biochemistry* **37**, 14659-14663.

Moënne-Loccoz, P., and de Vries, S. (1998b) Structural characterization of the catalytic high-spin heme *b* of nitric oxide reductase: a resonance Raman study. *J. Am. Chem. Soc.* **120**, 5147-5152.

Moënne-Loccoz, P., Krebs, C., Herlihy, K., Edmondson, D. E., Theil, E. C., Huynh, B. H., and Loehr, T. M. (1999) The ferroxidase reaction of ferritin reveals a diferric μ-1,2

bridging peroxide intermediate in common with other O_2-activating non-heme diiron proteins. *Biochemistry* **38**, 5290-5295.

Moënne-Loccoz, P., Richter, O. H., Huang, H., Wasser, I. M., Ghiladi, R. A., Karlin, K. D., and de Vries, S. (2000) Nitric oxide reductase from *Paracoccus denitrificans* contains an oxo-bridged heme/non-heme diiron center. *J. Am. Chem. Soc.* **122**, 9344-9345.

Moody, A. J. (1996) As prepared forms of fully oxidized heme/Cu terminal oxidases. *Biochim. Biophys. Acta*, **1276**, 6-20.

Moore, C. B., and Rosengren, K. (1966) Infrared spectrum and vibrational potential function of hydrazoic acid. *J. Chem. Phys.* **44**, 4108-4115.

Murad, F. (1999) Discovery of some of the biological effects of nitric oxide and its role in cell signaling. *Angew. Chem. Int. Ed. Engl.* **38**, 1857-1868.

Murrell, J. C., Gilbert, B., and McDonald, I. R. (2000) Molecular biology and regulation of methane monooxygenase. *Arch. Microbiol.* **173**, 325-332.

Nakamoto, K. (1997) Infrared and Raman spectroscopy of inorganic and coordination compounds. *5th ed, ed. K. Nakamoto. New York: John Wiley and Sons, Inc.*

Nelson, M. J. (1987) The nitric oxide complex of ferrous soybean lipoxygenase-1. Substrate, pH, and ethanol effects on the active-site iron. *J. Biol. Chem.* **262**, 12137-12142.

Nocek, J. M., Kurtz, D. M., Jr., Pickering, R. A., and Doyle, M. P. (1984) Oxidation of deoxyhemerythrin to semi-methemerythrin by nitrite. *J. Biol. Chem.* **259**, 12334-12338.

Nocek, J. M., Kurtz, D. M., Jr., Sage, J. T., Xia, Y. M., Debrunner, P., Shiemke, A. K., Sanders-Loehr, J., and Loehr, T. M. (1988) Nitric oxide adducts of the binuclear iron site of hemerythrin: spectroscopy and reactivity. *Biochemistry* **27**, 1014-1024.

Nordlund, P., Sjöberg, B. M., and Eklund, H. (1990) Three-dimensional structure of the free radical protein of ribonucleotide reductase. *Nature* **345**, 593-598.

Nordlund, P., and Eklund, H. (1993a) Structure and function of the *Escherichia coli.* ribonucleotide reductase protein R2. *J. Mol. Biol.* **232**, 123-164.

Nordlund, P., Aberg, A., Uhlin, U., and Eklund, H. (1993b) Crystallographic investigations of ribonucleotide reductase. *Biochem. Soc. Trans.* **21**, 735-738.

Obias, H. V., Lin, Y., Murthy, N. N., Pidcock, E., Solomon, E. I., Ralle, M., Blackburn, N. J., Neuhold, Y., Zuberbühler, A. D. and Karlin, K. D. (1998) Peroxo-, oxo-, and hydroxo-bridged dicopper complexes: observation of exogenous hydrocarbon substrate oxidation. *J. Am. Chem. Soc.* **120**, 12960-12961.

Ochiai, E., Mann, G. J., Graslund, A., and Thelander, L. (1990) Tyrosyl free radical formation in the small subunit of mouse ribonucleotide reductase. *J. Biol. Chem.* **265**, 15758-15761.

Oellerich, S., Bill, E., and Hildebrandt, P. (2000) Freeze-quench resonance Raman and electron paramagnetic resonance spectroscopy for studying enzyme kinetics. application to azide binding to myoglobin. *Appl. Spectrosc.* **54**, 1480-1484.

Orii, Y., Mogi, T., Sato-Watanabe, M., Hirano, T., and Anraku, Y. (1995) Facilitated intramolecular electron transfer in the *Escherichia coli. bo*-type ubiquinol oxidase requires chloride. *Biochemistry*, **34**, 1127-1132.

Orville, A. M., and Lipscomb, J. D. (1993) Simultaneous binding of nitric oxide and isotopically labeled substrates or inhibitors by reduced protocatechuate 3,4-dioxygenase. *J. Biol. Chem.* **268**, 8596-8607.

Ostermeier, C., Harrenga, A., Ermler, U., and Michel, H. (1997) Structure at 2.7 Å resolution of the *Paracoccus denitrificans* two-subunit cytochrome *c* oxidase complexed with an antibody F_V fragment. *Proc. Natl. Acad. Sci. U. S. A.* **94**, 10547-10553.

Park, E. S., Thomas, M. R., and Boxer, S. G. (2000) Vibrational stark spectroscopy of NO bound to heme: effects of protein electrostatic fields on the NO stretch frequency. *J. Am. Chem. Soc.* **122**, 12297-12303.

Parkin, S. E., Chen, S., Ley, B. A., Mangravite, L., Edmondson, D. E., Huynh, B. H., and Bollinger, J. M. Jr. (1998) Electron injection through a specific pathway determines the outcome of oxygen activation at the diiron cluster in the F208Y mutant of *Escherichia coli.* ribonucleotide reductase protein R2. *Biochemistry* **37**, 1124-1130.

Pate, J. E., Ross, P. K., Thamann, T. J., Reed, C. A., Karlin, K. D., Sorrell, T. N., and Solomon, E. I. (1989) Spectroscopic studies of the charge-transfer and vibrational features of binuclear copper(II) azide complexes: comparison to the coupled binuclear copper active site in met azide hemocyanin and tyrosinase. *J. Am. Chem. Soc.* **111**, 5198-5209.

Petersson, L., Graslund, A., Ehrenberg, A., Sjöberg, B. M., and Reichard, P. (1980) The iron center in ribonucleotide reductase from *Escherichia coli. J. Biol. Chem.* **255**, 6706-6712.

Pierce, B. S., Elgren, T. E., and Hendrich, M. P. (2003) Mechanistic implications for the formation of the diiron cluster in ribonucleotide reductase provided by quantitative EPR spectroscopy. *J. Am. Chem. Soc.* **125**, 8748-8759.

Proshlyakov, D. A., Pressler, M. A., DeMaso, C., Leykam, J. F., DeWitt, D. L., and Babcock, G. T. (2000) Oxygen activation and reduction in respiration: involvement of redox-active tyrosine 244. *Science* **290**, 1588-1591.

Pulver, S. C., Tong, W. H., Bollinger, J. M., Jr., Stubbe, J., and Solomon, E. I. (1995) Circular dichroism and magnetic circular dichroism studies of the fully reduced binuclear non-heme iron active site in the *Escherichia coli.* R2 subunit of ribonucleoside diphosphate reductase. *J. Am. Chem. Soc.* **117**, 12664-12678.

Que, L., Jr., and Dong, Y. (1996) Modeling the oxygen activation chemistry of methane monooxygenase and ribonucleotide reductase. *Acc. Chem. Res.* **29**, 190-196.

Que, L., Jr., and Tolman, W. B. (2002) Bis(μ-oxo)dimetal "diamond" cores in copper and iron complexes relevant to biocatalysis. *Angew. Chem. Int. Ed. Engl.* **41**, 1114-1137.

Que, L., Jr. (2004) The oxo/peroxo debate: a nonheme iron perspective. *J. Biol. Inorg. Chem.* **9**, 684-690.

Ralle, M., Verkhovskaya, M. L., Morgan, J. E., Verkhovsky, M. I., Wikstrom, M., and Blackburn, N. (1999) Coordination of Cu_B in reduced and CO-liganded states of cytochrome bo_3 from *Escherichia coli.* Is chloride ion a cofactor? *Biochemistry* **38**, 7185-7194.

Ravi, N., Bollinger, J. M., Jr., Huynh, B. H., Edmondson, D. E., and Stubbe, J. (1994) Mechanism of assembly of the tyrosyl radical-diiron(III) cofactor of *Escherichia coli.* ribonucleotide reductase: 1. Mössbauer characterization of the diferric radical precursor. *J. Am. Chem. Soc.* **116**, 8007-8014.

Ray, G. B., Li, X. Y., Ibers, J. A., Sessler, J. L., and Spiro, T. G. (1994) How far can proteins bend the FeCO unit? Distal polar and steric effects in heme proteins and models. *J. Am. Chem. Soc.* **116**, 162-176.

Reichard, P. (1993) From RNA to DNA, why so many ribonucleotide reductases? *Science* **260**, 1773-1777.

Richardson, D. J. (2000) Bacterial respiration: a flexible process for a changing environment. *Microbiology* **146**, 551-571.

Richter-Addo, G. B., Legzdins, P., and Burstyn, J. (2002) Introduction: nitric oxide chemistry. *Chem. Rev.* **102**, 857-859.

Riggs-Gelasco, P. J., Shu, L. J., Chen, S. X., Burdi, D., Huynh, B. H., Que, L., Jr., and Stubbe, J. (1998) EXAFS characterization of the intermediate X generated during the assembly of the *Escherichia coli.* ribonucleotide reductase R2 diferric tyrosyl radical cofactor. *J. Am. Chem. Soc.* **120**, 849-860.

Rosenzweig, A. C., Frederick, C. A., Lippard, S. J., and Nordlund, P. (1993) Crystal structure of a bacterial nonheme iron hydroxylase that catalyses the biological oxidation of methane. *Nature* **366**, 537-543.

Rosenzweig, A. C., Nordlund, P., Takahara, P. M., Frederick, C. A., and Lippard, S. J. (1995) Geometry of the soluble methane monooxygenase catalytic diiron center in two oxidation states. *Chem. Biol.* **2**, 409-418.

Rotenberg, M. O., and Maines, M. D. (1990) Isolation, characterization, and expression in *Escherichia coli.* of a cDNA encoding rat heme oxygenase-2. *J. Biol. Chem.* **265**, 7501-7506.

Ryle, M. J., and Hausinger, R. P. (2002) Non-heme iron oxygenases. *Curr. Opin. Chem. Biol.* **6**, 193-201.

Sazinsky, M. H., Bard, J., Di Donato, A., and Lippard, S. J. (2004) Crystal structure of the toluene/*o*-xylene monooxygenase hydroxylase from *Pseudomonas stutzeri* ox1: insight into the substrate specificity, substrate channeling, and active site tuning of multicomponent monooxygenases *J. Biol. Chem.* **279**, 30600-30610.

Schlichting, I., Berendzen, J., Chu, K., Stock, A. M., Maves, S. A., Benson, D. E., Sweet, R. M., Ringe, D., Petsko, G. A., and Sligar, S. G. (2000) The catalytic pathway of cytochrome P450cam at atomic resolution. *Science* **287**, 1615-1622.

Scott, R. A., Li, P. M., and Chan, S. I. (1988) The binuclear site of cytochrome *c* oxidase. Structural evidence from iron X-ray absorption spectroscopy. *Ann. N. Y. Acad. Sci.*, **550**, 53-58.

Selke, M., Sisemore, M. F., and Valentine, J. S. (1996) The diverse reactivity of peroxy ferric porphyrin complexes of electron-rich and electron-poor porphyrins. *J. Am. Chem. Soc.* **118**, 2008-2012.

Shapleigh, J. P., and Payne, W. J. (1985) Nitric oxide-dependent proton translocation in various denitrifiers. *J. Bacteriol.* **163**, 837-840.

Shapleigh, J. P., Hill, J. J., Alben, J. O., and Gennis, R. B. (1992) Spectroscopic and genetic evidence for two heme-Cu containing oxidases in *Rhodobacter sphaeroides*. *J. Bacteriol.* **174**, 2338-2343.

Siegbahn, P. E. M. (1998) Theoretical study of the substrate mechanism of ribonucleotide reductase. *J. Am. Chem. Soc.* **120**, 8417-8429.

Siegbahn, P. E. M. (2001) O–O bond cleavage and alkane hydroxylation in methane monooxygenase. *J. Biol. Inorg. Chem.* **6**, 27-45.

Silaghi-Dumitrescu, R., Kurtz, D. M., Jr., Ljungdahl, L. G., and Lanzilotta, W. N. (2005) X-ray crystal structures of *Moorella thermoacetica* FprA. Novel diiron site structure and mechanistic insights into a scavenging nitric oxide reductase. *Biochemistry*, **44**, 6492-6501.

Solomon, E. I., Brunold, T. C., Davis, M. I., Kemsley, J. N., Lee, S. K., Lehnert, N., Neese, F., Skulan, A.J., Yang, Y.S., and Zhou, J. (2000) Geometric and electronic structure/function correlations in non-heme iron enzymes. *Chem. Rev.* **100**, 235-349.

Song, S. H., and Asher, S. A. (1991) Internal intensity standards for heme protein UV resonance Raman studies: excitation profiles of cacodylic acid and sodium selenate. *Biochemistry* **30**, 1199-1205.

Stenkamp, R. E., Sieker, L. C., Jensen, L. H., McCallum, J. D., and Sanders-Loehr, J. (1985) Active site structure of deoxyhemerythrin and oxyhemerythrin. *Proc. Natl. Acad. Sci. U. S. A.* **82**, 713-716.

Stenmark, P., Grünler, J., Mattsson, J., Sindelar, P. J., Nordlund, P., and Berthold, D. A. (2001) A new member of the family of diiron carboxylate proteins: Coq7 (clk-1), a membrane-bound hydroxylase involved in ubiquinone biosynthesis. *J. Biol. Chem.* **276**, 33297-33300.

Stone, J. R., and Marletta, M. A. (1996) Spectral and kinetic studies on the activation of soluble guanylate cyclase by nitric oxide. *Biochemistry* **35**, 1093-1099.

Stubbe, J., and Riggs-Gelasco, P. (1998a) Harnessing free radicals: formation and function of the tyrosyl radical in ribonucleotide reductase. *Trends Biochem. Sci.* **23**, 438-443.

Stubbe, J., and van der Donk, W. A. (1998b) Protein radicals in enzyme catalysis. *Chem. Rev.* **98**, 705-762.

Stubbe, J., Ge, J., and Yee, C. S. (2001) The evolution of ribonucleotide reduction revisited. *Trends Biochem. Sci.* **26**, 93-99.

Sturgeon, B. E, Burdi, D., Chen, S. X., Huynh, B. H., Edmondson, D. E., Stubbe, J., and Hoffman, B. M. (1996) Reconsideration of X, the diiron intermediate formed during cofactor assembly in *Escherichia coli.* ribonucleotide reductase. *J. Am. Chem. Soc.* **118**, 7551-7557.

Suharti, S., Strampraad, M. J., Schroder, I. and de Vries, S. (2001) A novel copper A containing menaquinol NO reductase from *Bacillus azotoformans*. *Biochemistry* **40**, 2632-2639.

Tian, G., and Klinman, J. P. (1993) Discrimination between ^{16}O and ^{18}O in oxygen binding to the reversible oxygen carriers hemoglobin, myoglobin, hemerythrin, and hemocyanin: a new probe for oxygen binding and reductive activation by proteins. *J. Am. Chem. Soc.* **115**, 8891-8897.

Tierney, D. L., Fee, J. A., Ludwig, M. L., and Penner-Hahn, J. E. (1995) X-ray absorption spectroscopy of the iron site in *Escherichia coli.* Fe(III) superoxide dismutase. *Biochemistry* **34**, 1661-1668.

Tshuva, E. Y., and Lippard, S. J. (2004) Synthetic models for non-heme carboxylate-bridged diiron metalloproteins: strategies and tactics. *Chem. Rev.* **104**, 987-1012.

Tsubaki, M., Srivastava, R. B., and Yu, N. T. (1982) Resonance Raman investigation of carbon monoxide bonding in (carbon monoxy)hemoglobin and -myoglobin: detection of Fe-CO stretching and Fe-C-O bending vibrations and influence of the quaternary structure change. *Biochemistry* **21**, 1132-1140.

Tsukihara, T., Aoyama, H., Yamashita, E., Tomizaki, T., Yamaguchi, H., Shinzawa-Itoh, K., Nakashima, R., Yaono, R., and Yoshikawa, S. (1995) Structures of metal sites of oxidized bovine heart cytochrome *c* oxidase at 2.8 Å. *Science* **269**, 1069-1074.

Tsukihara, T., Aoyama, H., Yamashita, E., Tomizaki, T., Yamaguchi, H., Shinzawa-Itoh, K., Nakashima, R., Yaono, R., and Yoshikawa, S. (1996) The whole structure of the 13-subunit oxidized cytochrome *c* oxidase at 2.8 Å. *Science* **272**, 1136-1144.

Voegtli, W. C., Khidekel, N., Baldwin, J., Ley, B. A., Bollinger, J. M., Jr., and Rosenzweig, A. C. (2000) Crystal structure of the ribonucleotide reductase R2 mutant that accumulates a μ-1,2-peroxodiiron(III) intermediate during oxygen activation. *J. Am. Chem. Soc.* **122**, 3255-3261.

Voegtli, W. C., Sommerhalter, M., Saleh, L., Baldwin, J., Bollinger, J. M., Jr., and Rosenzweig, A. C. (2003) Variable coordination geometries at the diiron(II) active site of ribonucleotide reductase R2. *J. Am. Chem. Soc.* **125**, 15822-15830.

Vogel, K. M., Spiro, T. G., Shelver, D., Thorsteinsson, M. V., and Roberts, G. P. (1999) Resonance Raman evidence for a novel charge relay activation mechanism of the CO-dependent heme protein transcription factor CooA. *Biochemistry* **38**, 2679-2687.

Wallar, B. J., and Lipscomb, J. D. (1996) Dioxygen activation by enzymes containing binuclear non-heine iron clusters. *Chem. Rev.* **96**, 2625-2658.

Wallar, B. J, and Lipscomb, J. D. (2001) Methane monooxygenase component B mutants alter the kinetics of steps throughout the catalytic cycle. *Biochemistry* **40**, 2220-2233.

Walters, K. J., Gassner, G. T., Lippard, S. J., and Wagner, G. (1999) Structure of the soluble methane monooxygenase regulatory protein B. *Proc. Natl. Acad. Sci. U. S. A.* **96**, 7877-7882.

Wang, J., Takahashi, S., Hosler, J. P., Mitchell, D. M., Ferguson-Miller, S., Gennis, R. B., and Rousseau, D. L. (1995) Two conformations of the catalytic site in the *aa3*-type cytochrome *c* oxidase from *Rhodobacter sphaeroides*. *Biochemistry* **34**, 9819-9825.

Wang, J., Lu, S., Moënne-Loccoz, P., and Ortiz de Montellano, P. R. (2003) Interaction of nitric oxide with human heme oxygenase-1. *J. Biol. Chem.* **278**, 2341-2347.

Wasinger, E. C., Davis, M. I., Pau, M. Y., Orville, A. M., Zaleski, J. M., Hedman, B., Lipscomb, J. D., Hodgson, K. O., and Solomon, E. I. (2003) Spectroscopic studies of the effect of ligand donor strength on the Fe-NO bond in intradiol dioxygenases. *Inorg. Chem.* **42**, 365-376.

Wasser, I. M., de Vries, S., Moënne-Loccoz, P., Schroder, I., and Karlin, K. D. (2002) Nitric oxide in biological denitrification: Fe/Cu metalloenzyme and metal complex NO(x) redox chemistry. *Chem. Rev.* **102**, 1201-1234.

Wasserfallen, A., Ragettli, S., Jouanneau, Y., and Leisinger, T. (1998) A family of flavoproteins in the domains archaea and bacteria. *Eur. J. Biochem.* **254**, 325-332.

Wei, P. P., Skulan, A. J., Mitiac, N., Yang, Y. S., Saleh, L., Bollinger, J. M., Jr., and Solomon, E. I. (2004) Electronic and spectroscopic studies of the non-heme reduced binuclear iron sites of two ribonucleotide reductase variants: comparison to reduced methane monooxygenase and contributions to O_2 reactivity. *J. Am. Chem. Soc.* **126**, 3777-3788.

Wescott, B. L., and Enemark, J. H. (1999) Transition metal nitrosyls. *Inorganic electronic structure and spectroscopy; Lever, A. B. P., Solomon, E. I. Eds.; Wiley and*

Sons: New York **Vol. 2**, Chapter 7.

Whittington, D. A., Sazinsky, M. H., and Lippard, S. J. (2001) X-ray crystal structure of alcohol products bound at the active site of soluble methane monooxygenase hydroxylase. *J. Am. Chem. Soc.* **123**, 1794-1795.

Xie, J., Yikilmaz, E., Miller, A. F., and Brunold, T. C. (2002) Second-sphere contributions to substrate-analogue binding in iron(III) superoxide dismutase. *J. Am. Chem. Soc.* **124**, 3769-3774.

Zakhary, R., Poss, K. D., Jaffrey, S. R., Ferris, C. D., Tonegawa, S., and Snyder, S. H. (1997) Targeted gene deletion of heme oxygenase 2 reveals neural role for carbon monoxide. *Proc. Natl. Acad. Sci. U. S. A.* **94**, 14848-14853.

Zhang, C. X., Liang, H. C., Kim, E., Shearer, J., Helton, M. E., Kim, E., Kaderli, S., Incarvito, C. D., Zuberbühler, A. D., Rheingold, A. L., and Karlin, K. D. (2003) Tuning copper-dioxygen reactivity and exogenous substrate oxidations via alterations in ligand electronics. *J. Am. Chem. Soc.* **125**, 634-635.

Zumft, W. G., Braun, C., and Cuypers, H. (1994) Nitric oxide reductase from *Pseudomonas stutzeri*. Primary structure and gene organization of a novel bacterial cytochrome *bc* complex. *Eur. J. Biochem.* **219**, 481-490.

Zumft, W. G. (1997) Cell biology and molecular basis of denitrification. *Microbiol. Mol. Biol. Rev.* **61**, 533-616.

BIOGRAPHICAL SKETCH

Shen Lu was born on February 1st, 1975, in China. In 1997, he received a B.S. degree in Chemistry from Peking University of China. In 2000, he received a M.S. degree in Analytical Chemistry from Peking University. In the fall of 2000, he began his graduate studies in the Department of Environmental & Biomolecular Systems in OGI School of Science and Engineering at Oregon Health & Science University.

Publications:

Wang, J., Lu, S., Moënne-Loccoz, P., and Ortiz de Montellano, P. R. (2003) Interaction of nitric oxide with human heme oxygenase-1. *J. Biol. Chem.* **278**, 2341-2347.

de Vries, S., Strampraad, M. J., Lu, S., Moënne-Loccoz, P., and Schroder, I. (2003) Purification and characterization of the MQH2:NO oxidoreductase from the hyperthermophilic archaeon *Pyrobaculum aerophilum*. *J. Biol. Chem.* **278**, 35861-35868.

Kim, E., Helton, M. E., Wasser, I. M., Karlin, K. D., Lu, S., Huang, H., Moënne-Loccoz, P., Incarvito, C. D., Rheingold, A. L., Honecker, M., Kaderli, S., and Zuberbuhler, A. D. (2003) Superoxo, μ-peroxo, and μ-oxo complexes from heme/O_2 and heme-Cu/O_2 reactivity: copper ligand influences in cytochrome c oxidase models. *Proc. Natl. Acad. Sci. U. S. A.* **100**, 3623-3628.

Avila, L., Huang, H., Damaso, C. O., Lu, S., Moënne-Loccoz, P., and Rivera, M. (2003) Coupled oxidation vs heme oxygenation: insights from axial ligand mutants of mitochondrial cytochrome *b5*. *J. Am. Chem. Soc.* **125**, 4103-4110.

Lu, S., Suharti, de Vries S., and Moënne-Loccoz, P. (2004) Two CO molecules can bind concomitantly at the diiron site of NO reductase from *Bacillus azotoformans*. *J. Am. Chem. Soc.* **126**, 15332-15333.

Kim, E., Shearer, J., Lu, S., Moënne-Loccoz, P., Helton, M. E., Kaderli, S., Zuberbuhler, A. D., and Karlin, K. D. (2004) Heme/Cu/O_2 reactivity: change in Fe^{III}-(O_2^{2-})-Cu^{II} unit peroxo binding geometry effected by tridentate copper chelation. *J. Am. Chem. Soc.* **126**, 12716-12717.

Lu, S., Libby, E., Saleh, L., Xing, G., Bollinger, J. M. Jr., and Moënne-Loccoz, P. (2004) Characterization of NO adducts of the diiron center in protein R2 of *Escherichia coli.* ribonucleotide reductase and site-directed variants; implications for the O_2 activation mechanism. *J. Biol. Inorg. Chem.* **9**, 818-827.

Lu, S., Sazinsky, M. H., Whittaker, J. W., Lippard, S. J., and Moënne-Loccoz, P. (2005) Fourier transform infrared characterization of the azido complex of methane monooxygenase hydroxylase from *Methylococcus capsulatus* (Bath). *J. Am. Chem. Soc.* **127**, 4148-4149.

Lu, S., Wiertz, F. G. M., de Vries, S., and Moënne-Loccoz, P. (2005) Resonance Raman characterization of a high-spin six-coordinate iron(III) intermediate in the metmyoglobin-azido complex formation trapped by microsecond freeze-hyperquenching (MHQ). *J. Raman Spectrosc.* **36**, 359-362.

Andrew, C. R., Kemper, L. J., Busche, T. L., Tiwari, A. M., Kecskes, M. C., Stafford, J. M., Croft, L. C., Lu, S., Moënne-Loccoz, P., Huston, W., Moir, J. W. B., and Eady, R. R. (2005) Accessibility of the distal heme face, rather than Fe-His bond strength, determines the heme-nitrosyl coordination number of cytochromes *c'*: evidence from spectroscopic studies. *Biochemistry* **44**, 8664-8672.

Kim, E., Helton, M. E., Lu, S., Moënne-Loccoz, P., Incarvito, C. D., Rheingold, A. L., Kaderli, S., Zuberbühler, A. D., and Karlin, K. D. (2005) Tridentate copper ligand influences on heme-peroxo-copper formation and properties: reduced, superoxo, and μ-peroxo iron/copper complexes. *Inorg. Chem.* **44**, in press (web release: 08/26/2005).